이학박사학위논문

EMERGENT PHENOMENA FROM SPIN DEGREES OF FREEDOM IN LOW-DIMENSIONAL SYSTEMS

낮은 차원계의 스핀 자유도를 통한 떠오름 현상

2017년 2월

서울대학교 대학원

물리천문학부

이 형 준

EMERGENT PHENOMENA FROM SPIN DEGREES OF FREEDOM IN LOW-DIMENSIONAL SYSTEMS

낮은 차원계의 스핀 자유도를 통한 떠오름 현상

지도교수 최 무 영

이 논문을 이학박사 학위논문으로 제출함

2016년 11월

서울대학교 대학원

물리천문학부

이 형 준

이형준의 이학박사 학위논문을 인준함

2016년 12월

위 원 장	박 제 근	(인)
부위원장	최 무 영	(인)
위 원	김 창 영	(인)
위 원	양 범 정	(인)
위 원	전 건 상	(인)

EMERGENT PHENOMENA FROM SPIN DEGREES OF FREEDOM IN LOW-DIMENSIONAL SYSTEMS

A Dissertation
Presented to the Faculty of the Graduate School
of Seoul National University
in Partial Fulfillment of the Requirements for the Degree of
Doctor of Philosophy

by

Hyeong Jun Lee

February 2017

Abstract

We study emergent phenomena that occur in low dimensional spin and electronic systems, especially those related to spin degrees of freedom. In frustrated ferromagnetic spin-1 chains where the ferromagnetic nearest-neighbor coupling competes with the antiferromagnetic next-nearest-neighbor coupling, we analyze the ground state and its various correlation functions by using the density-matrix renormalization group. The double Haldane phase with ferromagnetic coupling shows incommensurate correlations of wavenumber q with $0 < q < \pi$ and transforms through a phase transition to the ferromagnetic phase. Such short-range correlations transform continuously into the ferromagnetic instability at the transition. The additional anisotropy in exchange interaction gives rise to a new disordered phase and a chirality phase in a wide region. We also compare the results with the spin-1/2 and classical spin systems, and discuss the string orders in the system.

We also investigate the magnetism on the edge of the Kane-Mele-Hubbard model. By means of the Hartree-Fock approximation we examine the nature of edge states in the presence of the Hubbard interaction in the Kane-Mele model. We compute local magnetizations of a nanoribbon with various widths. Phase

diagram is obtained in the thermodynamic limit. It turns out that in-plane magnetic order survives at the edges in a wide range of the spin-orbit coupling. The variation of its characteristic length is shown to be closely related to the phase transition between topological insulator and antiferromagnetic insulator.

Keywords: quantum spin chain, one-dimensional system, Haldane gap, AKLT state, spin exchange interaction, Heisenberg model, frustration, anisotropy, density-matrix renormalization-group, Kane-Mele-Hubbard model, honeycomb lattice, zigzag nanoribbon, spin-orbit interaction, Hubbard interaction, Hartree-Fock approximation, edge state, topological state

Student Number: 2012-30107

Contents

List of Figures

Chapter 1

Introduction

Low-dimensional quantum systems have attracted much interest for the past decade. One of the reasons is that quantum fluctuations play a more dominant role in their ground states than for higher-dimensional systems [1–3]. Generally quantum fluctuations suppress long-range order of a many-body system in low dimensions. In this case, interactions between particles play a more crucial role leading to novel emergent phenomena.

In 1983, it was suggested by Haldane [4, 5] that in the presence of antiferromagnetic nearest-neighbor interactions the integer/half-integer Heisenberg spin chains have ground states with/without excitation gaps. This has been confirmed by extensive theoretical and experimental studies [1–3]. In particular, one-dimensional odd-integer spin systems have disordered ground states in which symmetry is not broken with with a finite excitation gap [6–8]. There has been a spectacular advance in numerical tools with the introductioni of the density-matrix renormalization-group method by White [9, 10], which initiated extensive research on one-dimensional systems. The unprecedented high accuracy can be

obtained by this method; This allows us to obtain accurate ground states of much larger one-dimensional systems and to understand deeply the physics of low-dimensional systems.

Frustration is another important concept in physics. It is caused by the competition of two or more exchange interactions or the system geometry, and is known to generate enormous quantum emergent phenomena in exotic phases. One interesting example is a quantum spin chain with two types of interactions, one between nearest-neighbor spins and the other between next-nearest-neighbor spins. Extensive analytical and numerical studies on frustrated spin chains have been performed [3]. The frustrated chains exhibit numerous exotic phases and phase transitions among them. There is a nontrivial phase, the so-called AKLT state [6, 7] in spin-1 chains characterized by the nonlocal string order with $Z_2 \times Z_2$ symmetry [11–13].

Not only the spins, but also electrons in low-dimensional systems show very distinctive behaviors. It has been known that different topological orders can exist and cause distinct phases in materials without symmetry breaking. In particular, two-dimensional topological systems were suggested [14]. Insulators are classified into topologically trivial and non-trivial insulators in terms of a Z_2 topological invariance [15, 16]. The former is called a normal band insulator (NBI) that we are familiar with. The latter is characterized by bulk gap with gapless edge excitations, distinguished from the NBI, and is called a topological band insulator (TBI). The different topology produces metallic states at the boundary between the NBI and TBI inevitably. In the two-dimensional (2D) systems such a boundary state appears in the form of spin-current channels with

time-reversal symmetry conserved [17], and it has been generalized to the surface state with Dirac cones in the three-dimensional (3D) systems [18]. In principle, the boundary state is protected topologically and accordingly it is robust to weak disorder and interactions. Signatures of TBI were first observed in the experiment on HgTe/CdTe quantum wells [19]. The theoretical predictions of the surface states were also confirmed through the angle resolved photoemission spectroscopy (ARPES) experiment of BiSb [20]. A great number of experiments have recently been performed, particularly in the search for the transport evidence.

Such recent studies of TBI were initiated by the discovery of quantum spin Hall (QSH) insulators, which are induced by the intrinsic spin-orbit (SO) interactions [16, 17]. The QSH phase is shown to exist in the Kane-Mele (KM) model on the 2D honeycomb lattice. The Hamiltonian of the KM model consists of two terms: The nearest-neighbor hoppings from the kinetic energy and the next-nearest-neighbor hoppings induced by the intrinsic SO couplings. Electrons of QSH insulators are in a helical motion as in the integer quantum Hall systems and also in a chiral motion similar to that of graphene-pseudospins. Consequently, they exhibit one-dimensional (1D) spin current channels at the edge of the system.

On the other hand, the Hubbard model which has local Coulomb interaction between electrons with different spins has also been studied on the honeycomb lattice [21, 22]. The Hubbard interaction makes the electrons feel the repulsion. Above some critical value of the interaction strength electrons are localized, yielding a Mott gap. It also gives the antiferromagnetic order in the system with a spontaneous symmetry breaking [21]. The local magnetizations have been shown to display peculiar properties at the open boundary [22]. Recently, it has also

been reported that there exists a quantum spin liquid (QSL) phase before the charge-gap opening [23].

The interplay of the SO interaction and the Hubbard interaction has been studied in the Kane-Mele-Hubbard (KMH) model. The mean-field study revealed the phase transition from the TBI to antiferromagnetic insulator (AFI) in the presence of both SO interactions and Hubbard interactions [24]. The QSL has also been observed in the region of weak SO interactions [25]. Particular attention has been paid to how the characteristic edge state of TBI evolves as the interaction strength increases. While the helical edge state has been shown to persist below the critical interaction strength in the quantum Monte Carlo (QMC) study [25] and the variational cluster approach (VCA) [26], a different QMC calculation has yielded finite edge magnetism in the limit of infinite length [27]. In the latter study, finite edge magnetism has been interpreted as a signature of quasi-long-range order due to the 1D nature of the edge and the U(1) symmetry of spins. On the other hand the mean-field calculation in the finite nanoribbon system has revealed rich phases of the edge states in the TBI phase, which includes the half-metallic edge state with ferromagnetic order [28].

This dissertation is organized as follows. We first review quantum spin systems in one-dimension in Chap. 2. Previous theoretical studies are presented in detail as well as experiments on relevant systems. Chapter 3 is devoted to an explanation of numerical methods - the density-matrix renormalization group and the Hartree-Fock approximation. In Chap. 4, we investigate the frustrated spin-1 chains and present its results. The effect of the anisotropic exchange interaction in the frustrated chains is also examined in Chap. 5. Lastly, in Chap. 6, we

investigate the Kane-Mele-Hubbard model in nanoribbon geometry.

Chapter 2

Reviews of quantum spin chains

In this chapter, we will review the research on the one-dimensional spin-1 systems, which has been performed extensively for decades. Many interesting results have been known in one-dimensional quantum spin-1 models [1–3], especially after Haldane suggested that the antiferromagnetic spin chain systems can be classified by the spin number S [4, 5]. Haldane showed that systems with the integer/half-integer spin have ground states with/without excitation gaps in consideration of the one-dimensional Heisenberg model [29]. Its Hamiltonian is

$$\mathcal{H}_{\text{Heisenberg}} = J \sum_i \boldsymbol{S}_i \cdot \boldsymbol{S}_{i+1} \ , \tag{2.1}$$

where $\boldsymbol{S}_i \equiv (S_i^x, S_i^y, S_i^z)$ is a vector spin operator at ith site and $J > 0$. It was proved by a semi-classical approach using the nonlinear σ-model. Although his conjecture corresponds to the large spin limit, numerous theoretical and experimental studies have proved it in various spin systems. Some of these studies are introduced in the following sections.

2.1 Spin-1 chain models

The spin-1 chains have been studied intensively together with the spin-1/2 chains because they can be accessed more easily than others of higher spin number. Not only the gap in the spectrum can exist, Haldane also showed that correlation functions decay exponentially in the spin-1 chain. In addition to the suggestion by Haldane, Affleck *et al.* [6–8] showed that the first rigorous example of the gapped phase in spin-1 chains by using valence bonds.[1] They proved that the proposed valence-bond-solid (VBS) state is a unique ground state of an isotropic spin model with the translational and SO(3) symmetries. In addition, it also shows the exponential decay of the correlation functions. Although the model they investigated is different from the original Heisenberg model in Eq. (2.1) it was verified that its ground state is connected to that of the Heisenberg model [30].

In order to examine further the ground state of the isotropic spin model some researchers introduced a interesting correlation known as the "string" correlation [11–13]. They used various approaches and analogies to understand the VBS state with the string correlation function. It is shown that the VBS-type states in the quantum spin chains are equivalent to the disordered flat phase which is discovered in the two-dimensional surface-roughening transitions and that the string correlation function characterizes these VBS states [11]. The string order is also

[1] As well as in the spin-1 chains, they showed that other non-integral spin S systems in higher dimensions can have the gapped phases. This is when the following condition is satisfied :

$$S = \frac{z}{2}\, d\, n\ . \tag{2.2}$$

Spatial dimension and coordinate number are denoted by d and z, respectively, and n is any positive integer.

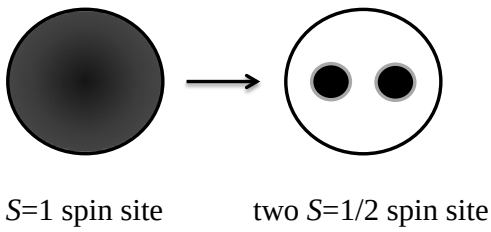

Figure 2.1: Sketch of the AKLT description of a $S = 1$ spin site represented by two $S = 1/2$ spins. In this case, symmetrization of the two $S = 1/2$ spins should be considered. Each $S = 1/2$ spin will bond with that of one of nearest-neighboring sites.

explained within the analogy between the $S = 1$ Heisenberg spin chain and the fractional quantum Hall effect [12]. The appearance of the Haldane gap in the $S = 1$ spin chain corresponds to the breaking of a hidden $Z_2 \times Z_2$ symmetry [13]. The nonlocal string order from the string correlation function is connected to the Haldane gap consequently.

2.1.1 AKLT (Affleck-Kennedy-Lieb-Tasaki) state

We first explain in detail the state of the singlet bonds proposed by Affleck *et al.* [6, 7], the so-called AKLT (Affleck-Kennedy-Lieb-Tasaki) state or the VBS state, which is an example of a class of quantum states for analytical studies, so-called "matrix product states" [31]. This started from the idea of the representation of the higher-spin states in the spin-1/2 basis states [6, 7]. For example, a spin-S site is represented by $2S$ spin-1/2 sites within the angular momentum addition (or the Clebsch-Gordan coefficients). Then, they consider the state in which there are singlet bonds between the spin-1/2 components of the nearest-neighbor sites.

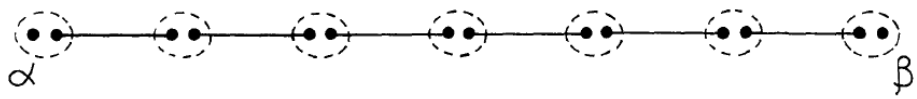

Figure 2.2: Sketch of the valence bond solid state, so-called the AKLT state, taken from Ref. 7. Each dot, line, and dashed circle denote a spin-1/2, a singlet bond, and a spin-1, respectively. It considers the free open boundary condition, so there exists a free spin-1/2 on each edge.

It was proved that this state can be the ground state of the isotropic spin model when it satisfies the condition of Eq. (2.2). It also enabled us to understand the higher spin systems and their ground states.

According to the AKLT description, a spin-1 site is decomposed by symmetrized states (triplet states) of the two spin-1/2 states as illustrated in Fig. 2.1. Together with their singlet bonds between the nearest-neighbor sites the spin-1 chain can be represented as shown in Fig. 2.2. The AKLT state was first considered in the special case of the bilinear-biquadratic model [32–37] of which Hamiltonian is

$$\mathcal{H}_{\mathrm{BB}} = \sum_i \left[\boldsymbol{S}_i \cdot \boldsymbol{S}_{i+1} - \beta (\boldsymbol{S}_i \cdot \boldsymbol{S}_{i+1})^2 \right] \ . \tag{2.3}$$

It was proved that the AKLT state is the exact ground state of the bilinear-biquadratic Hamiltonian for $\beta = -\frac{1}{3}$. This model is quiet different from the Heisenberg model (Eq. (4.1)), but their connection has been examined which will be explained later. In fact, the special case ($\beta = -\frac{1}{3}$) of the bilinear-biquadratic Hamiltonian (or the AKLT model) can come from a sum of projection operators. The projection is taken for the nearest-neighbor $S = 1$ spins and is expressed by

the following equation :

$$\mathcal{H}_i \equiv P^{(2)}(\boldsymbol{S}_i\ ,\boldsymbol{S}_{i+1}) \tag{2.4}$$

where $P^{(2)}$ denotes a projection operator of two spins to the $S = 2$ spin space It acts on a direct product of the two $S = 1$ spins and gives 1 if the direct product is in the $S = 2$ space or zero otherwise. By introducing another projection operator

$$X_i^{(j)} \equiv (\boldsymbol{S}_i + \boldsymbol{S}_{i+1}) \cdot (\boldsymbol{S}_i + \boldsymbol{S}_{i+1}) - j(j+1)\ , \tag{2.5}$$

we can rewrite $\mathcal{H}_i$ more specifically as follows :

$$\mathcal{H}_i = P^{(2)}(\boldsymbol{S}_i, \boldsymbol{S}_{i+1}) = \frac{1}{24}[2X_i^{(0)} + \left(X_i^{(1)}\right)^2 - 4]\ . \tag{2.6}$$

Then we have the Hamiltonian $\mathcal{H} \equiv \sum_i \mathcal{H}_i$ as in Eq. (2.3) which differs by the constant factor only. With this form of the Hamiltonian, one can shows that the AKLT state is a unique ground state for the periodic boundary condition in the thermodynamic limit (or it will have fourfold degeneracy for the standard open boundary condition) [7]. More detailed calculations about the $S = 1$ AKLT state on a chain, such as the correlation functions and the total spin value, will be explained in Sec. 2.1.4.

2.1.2 Heisenberg spin chains

After the AKLT state was proposed, There has been a progress in the general bilinear-biquadratic Hamiltonian which includes the isotropic Heisenberg model to understand the isotropic spin chain more [30, 35, 36]. It was revealed that

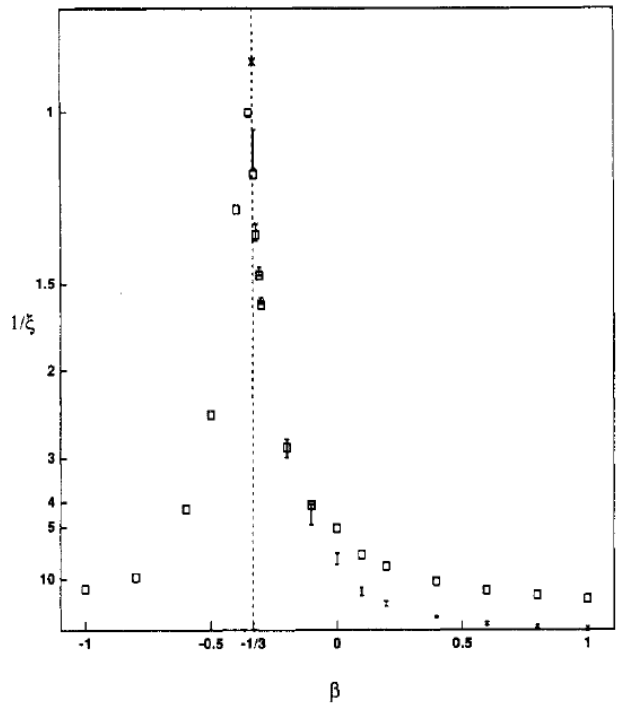

Figure 2.3: Spin-spin correlation length as a function of the biquadratic interaction strength β taken from Ref. 30. It shows the finite correlation length remains even in the Heisenberg point $\beta = 0$ and implies that a gapped state exists as Haldane suggested.

there is a connection between the ground states of the isotropic Heisenberg model and the AKLT model. As increasing β from -1 to 1 gradually in the bilinear-biquadratic Hamiltonian (Eq. (2.1)), Kennedy [30] showed that the system in the open boundary condition has the degenerate states from the AKLT description and finite correlation length by means of exact diagonalization. One of their result is shown in Fig. 2.3. This shows the spin-spin correlation length as a function of β ($-1 < \beta < 1$). It supports the Haldane's conjecture because the finite correlation

Table 2.1: Ground state energy and gap for various numerical methods. The data are taken from references ; Monte Carlo (MC) result from Ref. 38, exact diagonalization (ED) result from Ref. 39, series expansion (SE) result from Ref. 37, and density-matrix renormalization-group (DMRG) result from Ref. 40.

Method	Ground state energy (J)	Energy gap (J)
MC	$-1.4015(5)$	≈ 0.41
ED	-	0.1 - 0.4
SE	-	≈ 0.4
DMRG	$-1.401484038971(4)$	0.41050(2)

length means that the existence of a gap in the spectrum. They also showed that the total spin of the ground state becomes 0 or 1 depending on whether the size of the system is even or odd. They interpreted that there is a singlet or a triplet coming from unbounded $S = 1/2$ spins on each edge of the chain as we can see in Fig. 2.2. The slight difference in energy between the singlet and the triplet is shown to decay exponentially and become almost zero with increasing the system size. The alternation of the total spin of the ground state can be regarded as a result of the antiferromagnetic short-range correlation in the finite system. All these results also support that the AKLT state can be extended to the ground state of the Heisenberg model and become a good explanation.

In addition to the bilinear-biquadratic model, numerous numerical studies to explain the existence of the Haldane gap have been conducted by investigating the XXZ (exchange anisotropy) model [41–46] and the Heisenberg chain model itself [10, 38, 39, 47–50]. Among them, the density-matrix renormalization-method by

White [9, 10] showed the ground state of the Heisenberg chain and its energy in the open boundary condition with unprecedented accuracy. They calculated and showed the finite edge magnetization at very large sizes. It is attributed by the unbounded $S = 1/2$ edge spin which penetrates into the bulk, which is an evidence of the AKLT description [9, 40]. They also calculated the spin-spin correlation function $\langle \boldsymbol{S}_i \cdot \boldsymbol{S}_j \rangle$ and showed that it decays exponentially with the correlation length of $\xi \simeq 6.03(1)$. The penetrating length of the edge magnetization is very similar to that of the spin-spin correlation length. Some of numerical results of the ground state energy and the Haldane gap are listed in Tab. 2.1 according to calculation methods. The finite Haldane gap is obtained between the $S_z^{\mathrm{total}} = 0$ singlet ground state and the $S_z^{\mathrm{total}} = 1$ triplet states for the periodic boundary conditions while is obtained between the degenerate ($S_z^{\mathrm{total}} = 0$, 1) ground states and the $S_z^{\mathrm{total}} = 2$ quintuplet state for the open boundary conditions.

2.1.3 String correlation

The AKLT state can be interpreted as a fluid phase of the spin-1/2 particles with the antiferromagnetic order [11]. Nevertheless, the reason why spin-1 chain does not show the magnetic order is because the fluid is disordered spatially. This feature of the AKLT state can be characterized by the string correlation function $O(i, j)$ which is defined by

$$O(i, j) \equiv -\langle S_i^z \exp[i\pi \sum_{k=i+1}^{j-1} S_k^z] S_j^z \rangle \tag{2.7}$$

and shows the long range order, the so-called "string order". This is understood by the breaking of a hidden $Z_2 \times Z_2$ symmetry [13], showing the ground state is invariant under π-rotations about the three coordinate axes. With a nonlocal unitary transformation, the string correlation functions associated with not only S^z but also S^x are transformed into the ordinary spin-spin correlation functions $\langle S_i^\alpha S_j^\alpha \rangle$ $(\alpha = x,\ z)$. The action of the transformation on a chain represented by S^z-eigenstates (+,0, and -) is as follows :

(a) It does not change sites of 0.

(b) If the number of +'s sites and -'s sites which are left to site l is odd we replace the sign of the site l, and if the number is even we leave site l unchanged.

(c) We then multiply the state by -1 if the number of 0's at odd sites is odd.

The transformation is generalized by a set of operators with more specific forms later [51]. They expressed the above nonlocal transformation as follows :

$$U = \prod_i U_i \tag{2.8}$$

where

$$U_i \equiv \frac{1}{2}(1 + f_i^z + \frac{1}{2}(1 - f_i^z e^{i\pi S_i^x}) \ . \tag{2.9}$$

The string correlation function should be examined carefully because it can also capture the magnetically ordered states where the Z_2 symmetry breaks sponta-

neously. In the AKLT state described in the isotropic model, the string order parameters along (x and z) are the same, reflecting that the AKLT state is total spin zero and isotropic.

2.1.4 Matrix-product states

The matrix-product states (MPS) are constructed by taking the relevant part of the entire Hilbert space spanned by many-particle states, and are used in variational analytical approach usually [52, 53]. They are known to show only the exponentially decaying behavior rather than the criticality. In this section we will show one of the MPS representation of the AKLT state [7, 31]. For convenience, we will use the following notation :

$$|\uparrow\rangle = |S = \frac{1}{2}, S_z = +\frac{1}{2}\rangle \tag{2.10}$$

$$|\downarrow\rangle = |S = \frac{1}{2}, S_z = -\frac{1}{2}\rangle \tag{2.11}$$

and

$$|+\rangle = |S = 1, S_z = +1\rangle \tag{2.12}$$

$$|0\rangle = |S = 1, S_z = 0\rangle \tag{2.13}$$

$$|-\rangle = |S = 1, S_z = -1\rangle \ . \tag{2.14}$$

As we explained in the $S = 1$ AKLT state, two neighboring $S = 1/2$ spins forms the singlet bonding state and its representation is

$$|\Sigma^{(i)}; \text{singlet}\rangle = \frac{\left(|\uparrow_{b_i}\downarrow_{a_{i+1}}\rangle - |\downarrow_{b_i}\uparrow_{a_{i+1}}\rangle\right)}{\sqrt{2}} \tag{2.15}$$

$$= \begin{pmatrix} |\uparrow_{b_i}\rangle & |\downarrow_{b_i}\rangle \end{pmatrix} \underbrace{\begin{pmatrix} 0 & 1/\sqrt{2} \\ -1/\sqrt{2} & 0 \end{pmatrix}}_{\equiv\Sigma} \begin{pmatrix} |\uparrow_{a_{i+1}}\rangle \\ |\downarrow_{a_{i+1}}\rangle \end{pmatrix} \tag{2.16}$$

$$= \sum_{b_i, a_{i+1}} |b_i\rangle \left(\Sigma\right)_{b_i, a_{i+1}} |a_{i+1}\rangle \tag{2.17}$$

where we use

$$\Sigma \equiv \begin{pmatrix} 0 & 1/\sqrt{2} \\ -1/\sqrt{2} & 0 \end{pmatrix} \tag{2.18}$$

and $a_i(b_i)$ denotes the one $S = 1/2$ spin on the left(right) side at ith site, i.e., $|a_i\rangle = \{|\uparrow_{a_i}\rangle, |\downarrow_{a_i}\rangle\}$ (see Fig. 2.1). Considering the entire bonds of a chain of length L, we can write a state of the chain in terms of singlets as

$$|\psi_\Sigma\rangle = \otimes_i |\Sigma^{(i)}\rangle \ . \tag{2.19}$$

In order to describe a physical state of the $S = 1$ chain, we need a symmetrization of the on-site two $S = 1/2$ spins. It is indeed the triplet state because of the angular momentum addition. So we introduce a transformation operator (or a projection operator) $\tilde{P}_{(i)}$ which transforms the triplet state in the $S = 1/2$ basis

to the $S = 1$ basis states. It is represented by

$$\tilde{P}^{(i)} = |+_i\rangle\langle\uparrow_{a_i}\uparrow_{b_i}| + |0_i\rangle\frac{\langle\uparrow_{a_i}\downarrow_{b_i}| + \langle\downarrow_{a_i}\uparrow_{b_i}|}{\sqrt{2}} + |-_i\rangle\langle\downarrow_{a_i}\downarrow_{b_i}| \tag{2.20}$$

$$= \sum_{\sigma_i}\sum_{a_i,b_i} |\sigma_i\rangle\,(M)^{\sigma_i}_{a_i,b_i}\,\langle a_i|\langle b_i| \tag{2.21}$$

where we define

$$M^+ = \begin{pmatrix} 1 & 0 \\ 0 & 0 \end{pmatrix},\ M^0 = \begin{pmatrix} 0 & \frac{1}{\sqrt{2}} \\ \frac{1}{\sqrt{2}} & 0 \end{pmatrix},\ M^- = \begin{pmatrix} 0 & 0 \\ 0 & 1 \end{pmatrix} \tag{2.22}$$

and $|\sigma_i\rangle = \{|+_i\rangle, |0_i\rangle, |-_i\rangle\}$. Taking this operator into each site of the chain, we have finally the AKLT state ψ which is written as

$$|\psi\rangle = \otimes_i \left(P^{(i)}|\Sigma^{(i)}\rangle\right) \tag{2.23}$$

and

$$P^{(i)}|\Sigma^{(i)} = \left(\sum_{\sigma_i}\sum_{a_i,b_i} |\sigma_i\rangle\,(M)^{\sigma_i}_{a_i,b_i}\,\langle a_i|\langle b_i|\right)\left(\sum_{b'_i,a'_{i+1}} |b'_i\rangle\,(\Sigma)_{b'_i,a'_{i+1}}\,|a'_{i+1}\rangle\right) \tag{2.24}$$

$$= \sum_{\sigma_i}\sum_{a_i,a'_{i+1}} |\sigma_i\rangle\,\underbrace{(M\Sigma)^{\sigma_i}_{a_i,a'_{i+1}}}_{\equiv\tilde{C}}\langle a_i| \otimes |a'_{i+1}\rangle\ . \tag{2.25}$$

We obtained the following matrices from Eq. (2.25) :

$$\tilde{C}^+ \equiv \begin{pmatrix} 0 & \frac{1}{\sqrt{2}} \\ 0 & 0 \end{pmatrix},\ \tilde{C}^0 \equiv \begin{pmatrix} -\frac{1}{2} & 0 \\ 0 & \frac{1}{2} \end{pmatrix},\ \tilde{C}^- \equiv \begin{pmatrix} 0 & 0 \\ -\frac{1}{\sqrt{2}} & 0 \end{pmatrix}\ . \tag{2.26}$$

We need to normalize the state in a common space, so we take the left-normalization of $\tilde{C}^{\sigma_i}$, i.e., the unitarity in the a_{i+1} basis. It is carried out by using

$$\sum_{\sigma_i} \tilde{C}^{\sigma_i} \tilde{C}^{\sigma_i} = \frac{3}{4} I_{a_{i+1}} \ , \tag{2.27}$$

and we take $C^{\sigma_i} \equiv \frac{2}{\sqrt{3}} \tilde{C}^{\sigma_i}$ so that

$$\sum_{\sigma_i} C^{\sigma_i} C^{\sigma_i} = I_{a_{i+1}} \tag{2.28}$$

where I_α denotes an identity matrix in α-space. The AKLT state can be rewritten with the periodic boundary condition as

$$|\psi\rangle = \sum_{\sigma} \mathrm{Tr}[C^{\sigma_1} C^{\sigma_2} \cdots C^{\sigma_L}] |\sigma\rangle \tag{2.29}$$

where $\sigma = |\sigma_1 \sigma_2 \cdots \sigma_L\rangle$. It should also satisfy the normalization condition,

$$\langle\psi|\psi\rangle = \sum_{\sigma} \mathrm{Tr}[C^{\sigma_1} C^{\sigma_2} \cdots C^{\sigma_L}] * |\mathrm{Tr}[C^{\sigma_1} C^{\sigma_2} \cdots C^{\sigma_L}]| \tag{2.30}$$

$$= \mathrm{Tr}[\left(\sum_{\sigma_1} C^{\sigma_1 *} \otimes C^{\sigma_1}\right) \left(\sum_{\sigma_2} C^{\sigma_2 *} \otimes C^{\sigma_2}\right) \cdots \left(\sum_{\sigma_L} C^{\sigma_L *} \otimes C^{\sigma_L}\right)] \tag{2.31}$$

$$= \mathrm{Tr}[(D)^L] = \sum_i (\lambda_{D,i})^L \tag{2.32}$$

where $D \equiv \sum_{\sigma_i} C^{\sigma_i *} C^{\sigma_i}$ and $\lambda_{D,i}$ is an eigenvalue of D. We can diagonalized D as

$$D = \frac{4}{3} \begin{pmatrix} \frac{1}{4} & 0 & 0 & \frac{1}{2} \\ 0 & -\frac{1}{4} & 0 & 0 \\ 0 & 0 & -\frac{1}{4} & 0 \\ \frac{1}{2} & 0 & 0 & \frac{1}{4} \end{pmatrix} \rightarrow \Lambda_D \equiv U^{-1} D U = \begin{pmatrix} 1 & 0 & 0 & 0 \\ 0 & -\frac{1}{3} & 0 & 0 \\ 0 & 0 & -\frac{1}{3} & 0 \\ 0 & 0 & 0 & -\frac{1}{3} \end{pmatrix} . \tag{2.33}$$

We used an orthogonal matrix U ($UU^{\mathrm{T}} = I$)

$$U = \begin{pmatrix} \frac{1}{\sqrt{2}} & 0 & 0 & -\frac{1}{\sqrt{2}} \\ 0 & 1 & 0 & 0 \\ 0 & 0 & 1 & 0 \\ \frac{1}{\sqrt{2}} & 0 & 0 & \frac{1}{\sqrt{2}} \end{pmatrix} \tag{2.34}$$

in Eq. (2.33) Finally, we can see that the MPS state is normalized as

$$\langle \psi | \psi \rangle = 1 + 3(-\frac{1}{3})^L \quad \xrightarrow{L \to \infty} \; 1 \; . \tag{2.35}$$

We consider the thermodynamic limit ($L \to \infty$) where the normalization of the AKLT state is valid for calculating its physical quantities in the following sections.

Correlation function

We can now calculate the spin-spin correlation function $\langle\psi|S_i^z S_j^z|\psi\rangle$. From Eq. (2.29) we have

$$\langle\psi|S_i^z S_j^z|\psi\rangle = \sum_{\sigma} \mathrm{Tr}[C^{\sigma_1}C^{\sigma_2}\cdots C^{\sigma_L}]^* S_i^z S_j^z \mathrm{Tr}[C^{\sigma_1}C^{\sigma_2}\cdots C^{\sigma_L}] \tag{2.36}$$

$$= \mathrm{Tr}[\left(\sum_{\sigma_1} C^{\sigma_1 *}\otimes C^{\sigma_1}\right)\cdots\left(\sum_{\sigma_i} C^{\sigma_i *}\otimes (S_i^z C^{\sigma_i})\right) \tag{2.37}$$

$$\times\cdots\times\left(\sum_{\sigma_j} C^{\sigma_j *}\otimes (S_j^z C^{\sigma_j})\right)\cdots\left(\sum_{\sigma_L} C^{\sigma_L *}\otimes C^{\sigma_L}\right)]\,. \tag{2.38}$$

By using the following relations

$$C^{\sigma_i *} = C^{\sigma_i} \tag{2.39}$$

and

$$S_i^z C^{\sigma_i}|\sigma_i\rangle = \begin{pmatrix} C^+|+_i\rangle \\ 0 \\ -C^-|-_i\rangle \end{pmatrix}\,, \tag{2.40}$$

we have

$$D_z \equiv \sum_{\sigma_i} C^{\sigma_i *}\otimes (S_i^z C^{\sigma_i}) = C^+\otimes C^+ - C^-\otimes C^- = \begin{pmatrix} 0 & 0 & 0 & \frac{2}{3} \\ 0 & 0 & 0 & 0 \\ 0 & 0 & 0 & 0 \\ -\frac{2}{3} & 0 & 0 & 0 \end{pmatrix}\,. \tag{2.41}$$

With the transformation U from Eq. (2.34), we also obtain

$$D'_z \equiv U^{-1} D_z U = D_z \ . \tag{2.42}$$

The correlation function then becomes

$$\langle\psi|S_i^z S_j^z|\psi\rangle = \mathrm{Tr}[D^{i-1}\, D_z\, D^{j-i-1}\, D_z\, D^{L-j}] \tag{2.43}$$

$$= \mathrm{Tr}[\Lambda^{i-1}\, \underbrace{D_z\, \Lambda^{j-i-1}\, D_z}\, \Lambda^{L-j}] \tag{2.44}$$

where we inserted $U^{-1}U$ into Eq. (2.43) to obtain Eq. (2.44). The underbraced part in Eq. (2.44) is calculated as

$$D_z\, \Lambda^{j-i-1}\, D_z = D_z \begin{pmatrix} 1 & 0 & 0 & 0 \\ 0 & (-\frac{1}{3})^{j-i-1} & 0 & 0 \\ 0 & 0 & (-\frac{1}{3})^{j-i-1} & 0 \\ 0 & 0 & 0 & (-\frac{1}{3})^{j-i-1} \end{pmatrix} D_z \tag{2.45}$$

$$= -\frac{4}{9} \begin{pmatrix} (-\frac{1}{3})^{j-i-1} & 0 & 0 & 0 \\ 0 & 0 & 0 & 0 \\ 0 & 0 & 0 & 0 \\ 0 & 0 & 0 & 1 \end{pmatrix} \ . \tag{2.46}$$

As a result, we have a final form of the correlation function

$$
\begin{aligned}
&\langle\psi|S_i^z S_j^z|\psi\rangle \\
&= \mathrm{Tr}\begin{pmatrix} -\frac{4}{9}(-\frac{1}{3})^{j-i-1} & 0 & 0 & 0 \\ 0 & 0 & 0 & 0 \\ 0 & 0 & 0 & 0 \\ 0 & 0 & 0 & -\frac{4}{9} \end{pmatrix} \\
&\quad \times \begin{pmatrix} 1 & 0 & 0 & 0 \\ 0 & (-\frac{1}{3})^{L-j+i-1} & 0 & 0 \\ 0 & 0 & (-\frac{1}{3})^{L-j+i-1} & 0 \\ 0 & 0 & 0 & (-\frac{1}{3})^{L-j+i-1} \end{pmatrix} \qquad (2.47) \\
&= -\frac{4}{9}(-\frac{1}{3})^{j-i-1} - \frac{4}{9}(-\frac{1}{3})^{L-j+i-1} \\
&\simeq -\frac{4}{9}(-\frac{1}{3})^{j-i-1} \qquad \text{for } L \to \infty\,. \qquad (2.48)
\end{aligned}
$$

We can see that the correlation function is exponentially decaying with its correlation length ξ of $(\ln 3)^{-1} \simeq 0.91$. Also, it has an oscillation with the distance $|i-j|$ of which period is 2. It reflects that the pure antiferromagnetic correlation exists, but there is no magnetic order. It has been known that this correlation length corresponds well to the numerical results [30, 54].

String order

The AKLT state is characterized not only by the absence of the magnetic order but also by the nonlocal string order. We calculate the string correlation function of the AKLT state by using the MPS representation and show that its long range

order exists.

From Eq. (2.7) we first need to calculate the following :

$$D_{ez} \equiv \sum_{\sigma_i} C^{\sigma_i *} \otimes (e^{i\pi S_i^z} C^{\sigma_i}) = -C^+ \otimes C^+ + C^0 \otimes C^0 - C^- \otimes C^- \tag{2.49}$$

$$= \begin{pmatrix} \frac{1}{3} & 0 & 0 & -\frac{2}{3} \\ 0 & -\frac{1}{3} & 0 & 0 \\ 0 & 0 & -\frac{1}{3} & 0 \\ -\frac{2}{3} & 0 & 0 & \frac{1}{3} \end{pmatrix} \tag{2.50}$$

where we used

$$e^{i\pi S_i^z} C^{\sigma_i} |\sigma_i\rangle = \begin{pmatrix} -C^+|+_i\rangle \\ C^0|0_i\rangle \\ -C^-|-_i\rangle \end{pmatrix} . \tag{2.51}$$

The transformation U from Eq. (2.34) gives us

$$D_{ez} \to D'_{ez} = U^{-1} D_{ez} U = \begin{pmatrix} -\frac{1}{3} & 0 & 0 & 0 \\ 0 & -\frac{1}{3} & 0 & 0 \\ 0 & 0 & -\frac{1}{3} & 0 \\ 0 & 0 & 0 & 1 \end{pmatrix} \equiv \Lambda_{ez}. \tag{2.52}$$

The string order parameter $O(i,j)$ is then calculated as

$$
\begin{aligned}
-O(i,j) &= \langle S_i^z \exp(i\pi \sum_{k=i+1}^{j-1} S_k^z) S_j^z \rangle && (2.53)\\
&= \mathrm{Tr}[D^{i-1}\, D_z\, D_{ez}^{j-i-1}\, D_z\, D^{L-j}] && (2.54)\\
&= \mathrm{Tr}[\underbrace{D_z\, \Lambda_{ez}^{j-i-1}\, D_z}\, \Lambda^{L-j+i-1}] && (2.55)\\
&= -\frac{4}{9}\, \mathrm{Tr} \begin{pmatrix} 1 & 0 & 0 & 0 \\ 0 & 0 & 0 & 0 \\ 0 & 0 & 0 & 0 \\ 0 & 0 & 0 & (-\frac{1}{3})^{j-i-1} \end{pmatrix} \begin{pmatrix} 1 & 0 & 0 & 0 \\ 0 & (-\frac{1}{3})^{L-j+i-1} & 0 & 0 \\ 0 & 0 & (-\frac{1}{3})^{L-j+i-1} & 0 \\ 0 & 0 & 0 & (-\frac{1}{3})^{L-j+i-1} \end{pmatrix} \\
&= -\frac{4}{9}\left(1 + (-\frac{1}{3})^{L-2}\right) && (2.56)\\
&\simeq -\frac{4}{9} \qquad \text{for} \qquad L \to \infty && (2.57)
\end{aligned}
$$

If we rewrite the above results, the value of the string order defined as

$$O_{\text{string}} \equiv \lim_{|i-j|\to\infty} O(i,j)$$

is $\frac{4}{9}$. It certainly corresponds to the numerical results of the AKLT model ($\beta = -\frac{1}{3}$ case in Eq. (2.3)) [12, 55].

2.1.5 Frustrated spin chains

So far we have reviewed the Heisenberg single chain with antiferromagnetic nearest-neighbor couplings. The real system, however, has more complicated interactions and geometries. This leads to frustration, one of the interesting things that enrich physics. Since the first frustrated system [56] and the word "frustration" [57, 58]

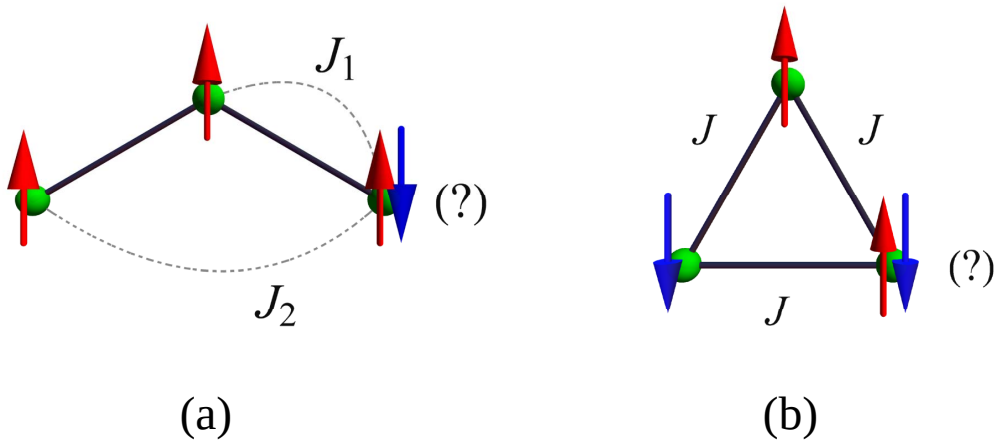

Figure 2.4: Two examples of the frustrated spin system. (a) One is the system described by two types of interactions - the antiferromagnetic interaction with nearest-neighbors and the ferromagnetic (or antiferromagnetic) interaction with next-nearest-neighbors. Of which interaction strengths are denoted by the positive constant J_1 and the negative J_2, respectively. (b) The other one is the system frustrated by the geometrical factor. The three spins are coupled by the antiferromagnetic nearest-neighbor interaction of which strength is denoted by J. These two systems has a ground state(s) which cannot be determined simply by classical states.

were introduced it has attracted much attentions in the last decades [3]. Its rich and unexpected effects have led to many interesting studies with enormous quantum emergent phenomena and exotic phases. Extensive studies on the frustrated spin chains have been performed. In this section, we will give one good example of the frustrated spin chains and show the results of the previous studies.

Frustration

We say that a system is frustrated when its spin state cannot be determined by fully satisfying all the interactions with neighboring spins to give the minimum

energy in each bond [3, 59]. The frustration is mostly shown in systems including at least one kind of antiferromagnetic interaction. This is because a set of ferromagnetic interactions can be satisfied fully and give rise to the ferromagnet such as in the Heisenberg model (Eq. (2.1)). The main cause of frustration is either the competition of two or more exchange interactions or the system geometry. Two typical examples of the spin system in the frustration are shown in Fig. 2.4. One is the case in which there is the two kinds of interactions the antiferromagnetic interaction with nearest-neighbors and the ferromagnetic (or antiferromagnetic) interaction with next-nearest-neighbors (Fig. 2.4(a)). The other one is the system of which three spins are coupled by the antiferromagnetic nearest-neighbor interaction only (Fig. 2.4(b)). Both two examples show that the classical spin state is not fully satisfying all interactions, but partially. It is then hard to determine their ground state. We will find the degeneracy in the ground state instead. This description is applicable to other types of local interactions, and shows that the system is frustrated if the classical spin state does not fully minimize all the interactions.

Another simple way to see if the system is frustrated is to use plaquettes, polygons that make up an unit cell [57]. When the following quantity defined on a plaquette is negative, the system or the plaquette are frustrated :

$$F \equiv \prod_{\langle i,j \rangle \in \text{plaqutte}} \text{sign}(J_{i,j}) \tag{2.58}$$

where $J_{i,j}$ is the exchange interaction strength between the nearest-neighbors i and j. For example, a triangle and a square with the antiferromagnetic Heisen-

berg interaction have $F = -1$, and we can see that they and their lattices are frustrated.

J_1-J_2 model

We introduce the J_1-J_2 model of the spin-1 chain. This model has the interplay of the two interactions as we can see in Fig. 2.4(a). The Hamiltonian is written as

$$\mathcal{H} = J_1 \sum_i \boldsymbol{S}_i \cdot \boldsymbol{S}_{i+1} + J_2 \sum_i \boldsymbol{S}_i \cdot \boldsymbol{S}_{i+2} \tag{2.59}$$

There have been many studies about the frustrated chain where both J_1 and J_2 are positive and the resulting antiferromagnetic interactions interplay with each other. If we first consider the case of the absence of the nearest-neighbor interaction ($J_1 = 0$). the system reduces to two decoupled subchains; each consists of next-nearest-neighbor singlet pairs from the antiferromagnetic next-nearest-neighbor interaction ($J_2 > 0$). The individual subchain lies in the Haldane gapped phase. As well as the excitation gap the exponentially decaying spin-spin correlations and long-range string order [40] still remain. Such a phase is called the double Haldane (DH) phase, This is also understood well by the AKLT description, with four unbounded $S = 1/2$ edge spins in open boundary condition and a 16-fold degeneracy of the ground state.

In the presence of the nearest-neighbor interaction in addition, it was revealed [61, 62] that the double Haldane phase undergoes a discontinuous transition to the Haldane phase at $J_2/J_1 \simeq 0.744$ although they seems to be similar to each other. At the transition point, the system exhibits a jump in the string

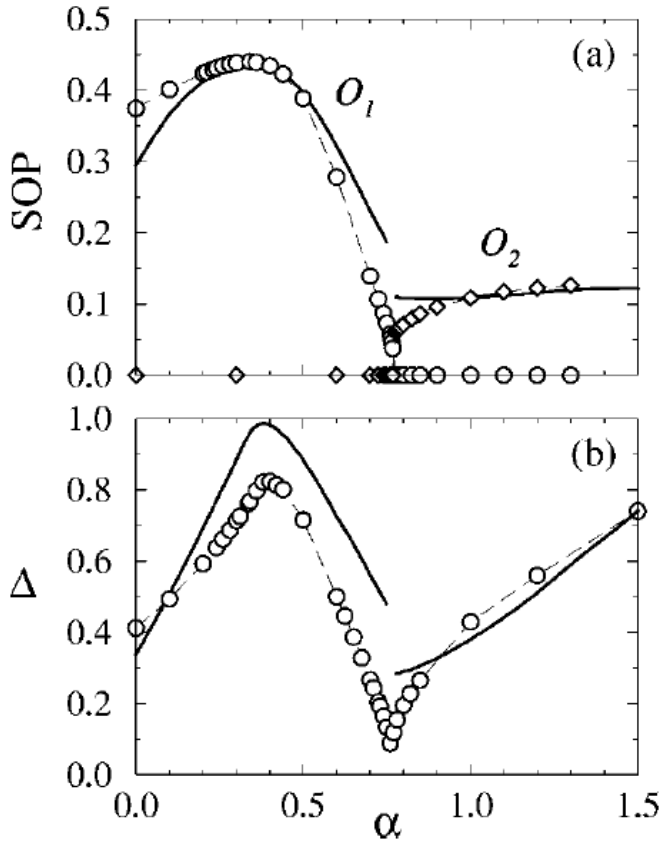

Figure 2.5: (a) String order parameters and (b) gap of the J_1-J_2 model taken from Ref. 60. The single and double string order parameters are denoted by O_1 and O_2, respectively, and $\alpha \equiv J_2/J_1$. Each string order parameter has the jump at the phase transition point, $J_2/J_1 \simeq 0.744$. The gap between the ground state and the first (bulk) excited state in spectrum is denoted by Δ. The result that gap does not become zero at the transition point indicates that it is the discontinuous phase transition between the Haldane and DH phases.

order parameter with the finite bulk gap and a cusp of the correlation length data. As the ratio of J_2/J_1 is changed more, the string order which is defined in

Eq. (2.7) becomes finite in the Haldane phase. The DH phase is, however, not characterized by the type of string order. This fact shows that the string correlation function is different from the ordinary correlation functions. Kolezhuk *et al.* [60] considered so-called the "double" string correlation function defined by

$$O_2(i,j) \equiv \langle S_i^z S_{i+1}^z \exp[i\pi \sum_{k=i+2}^{j-2} S_k^z] S_{j-1}^z S_j^z \rangle \tag{2.60}$$

instead to characterize the DH phase. This correlator shows a long range order in the DH phase only. These two kinds of the string correlation show a jump at the transition point $J_2/J_1 \simeq 0.744$ as shown in Fig. 2.5. It is interpreted as the two AKLT states in the DH phase adiabatically change with the soliton excitations and it results in a change of connectivities of the two states intertwined [60].

2.1.6 Anisotropy effects

XXZ spin chains

The effects of the anisotropic exchange interaction on the spin-1 chains will be shown in the section. The Heisenberg isotropic exchange interaction is replaced by the anisotropy as follows :

$$\boldsymbol{S}_i \cdot \boldsymbol{S}_{i+1} \rightarrow S_i^x S_{i+1}^x + S_i^y S_{i+1}^y + J_z S_i^z S_{i+1}^z \tag{2.61}$$

$$= \frac{1}{2}\left(S_i^+ S_{i+1}^- + S_i^- S_{i+1}^+\right) + J_z S_i^z S_{i+1}^z \ . \tag{2.62}$$

The strength of the exchange anisotropy is denoted by J_z. Such a model described by this anisotropic exchange interaction is called the "XXZ" model. The XXZ

model connects the Heisenberg model with the Ising model [63, 64] and the XY model [65] which traditionally have been studied for a very long time exhibited many interesting phenomena. In the spin-1 system, anisotropic interactions also cause spontaneous symmetry-breaking or the phase transition to the XY phase, which is similar to the $S = 1/2$ or classical spin systems [41, 42]. For the Ising limit ($|J_z| \to \infty$), there are two well-known symmetry-broken states; one is the Ising ferromagnet and the other is the Ising antiferromagnet. They do not have time-reversal symmetry, but long range magnetic orders. There is a difference between the areas of these two Ising states in the spin-1 systems. The Haldane gapped phase that we have described so far appears between the Ising antiferromagnet and the XY phases [39, 47, 48, 66–68]. It was shown that the phase transition from the Haldane phase to the Ising antiferromagnetic phase occurs at $J_z = J_{z,c_1}$ [41, 69, 70]. The value of J_{z,c_1} is known as 1.167(7) for the large system size [69]. They also obtained its critical exponents

$$\beta = 0.126(7) \tag{2.63}$$

$$\nu = 0.98(2) \tag{2.64}$$

$$\eta = 0.25(3) \tag{2.65}$$

defined by

$$m_z \equiv \lim_{l\to\infty} \sqrt{\langle S_0^z S_l^z \rangle} \tag{2.66}$$

$$m_z \sim |J_z - J_{z,c_1}|^{\beta} \tag{2.67}$$

$$\xi \sim |J_z - J_{z,c_1}|^{-\nu} \tag{2.68}$$

$$\xi \sim |J_z - J_{z,c_1}|^{-\nu} \tag{2.69}$$

$$\langle S_0^z S_l^z \rangle \sim r^{-\eta} \ . \tag{2.70}$$

These values are very close to the classical 2D Ising critical exponents - $\beta = \frac{1}{8}$, $\nu = 1$, and $\eta = \frac{1}{4}$. It means that they belong to the same universality class [69, 70].

Single-ion anisotropy

There has been another type of anisotropy in addition to the exchange isotropy. It is the "single-ion anisotropy" (or crystal field anisotropy) which is effectively derived from the weak spin-orbit coupling (see more details in Ref. 72). This effect usually exists in the real systems. The additional Hamiltonian from the single-ion anisotropy is given by

$$\mathcal{H}_{\text{single-ion}} = \sum_i D\,(S_i^z)^2 \tag{2.71}$$

where D denotes its strength. This anisotropy affects only the system with spin $S > 1/2$. Briefly, the spins favour ordering along the z-direction when $D > 0$ while the spins tend to lie on the xy-plane when $D < 0$. In the spin-1 systems, its effect has been studied in the XXZ model [43, 45, 46, 73–75]. Various distinctive

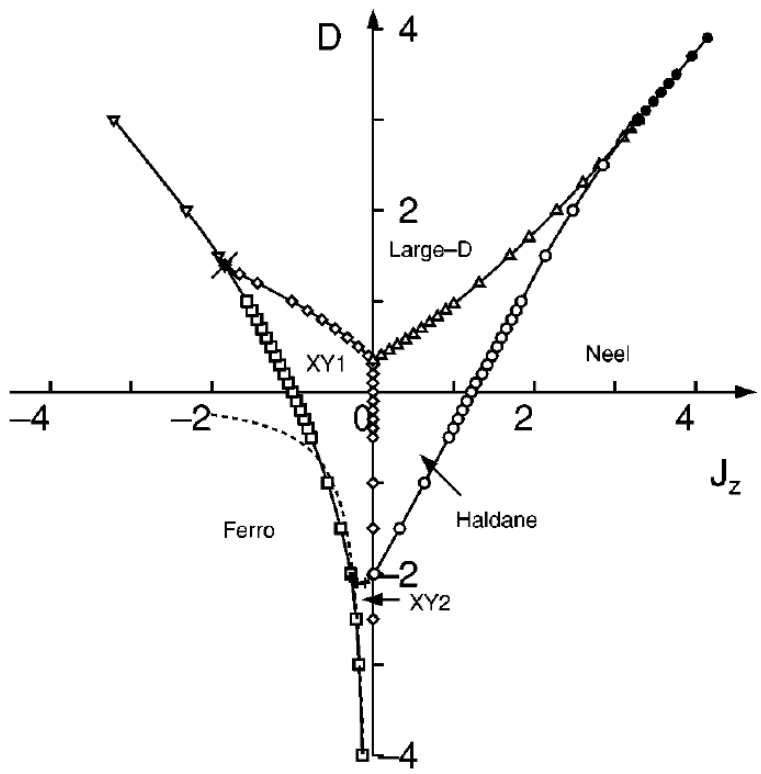

Figure 2.6: Phase diagram of the XXZ model with the single-ion anisotropy in J_z-D plane from Ref. 71.

phases were obtained in this model as shown in Fig. 2.6. As well as the Haldane, XY (or XY1), and two magnetic ordered phases that can be obtained in the XXZ model, there are two more phases - the large-D phase and the XY2 phase - which exist for relatively large D. The large-D phase can be represented by a state of $|0000\cdots00\rangle$ when $D \to \infty$ (0 means a $S_z = 0$ eigenstate for a $S = 1$ spin site). The continuous transition to the Haldane phase from the large-D phase

is found with closing the gap and is characterized by the value of the central charge of the conformal field theory. The central charge can be obtained by the excitation spectrum or the entanglement entropy [71, 75, 76]. It is interesting to note that the Haldane phase is quiet robust against the anisotropy ($D \neq 0$ or $J_z \neq 1$). In particular, the area of the Haldane phase is enlarged for $J_z < 1$. The XY1 and XY2 phases appear with power-law decays of the correlation functions without gap in spectrum. The XY1 phase shows the power-decay of the typical correlation functions $\langle S_i^x S_j^x \rangle$ and $\langle S_i^y S_j^y \rangle$ while the XY2 phase shows the power-decay of $\langle {S_i^x}^2 {S_j^x}^2 \rangle$ and $\langle {S_i^y}^2 {S_j^y}^2 \rangle$.

Anisotropy with frustration

The anisotropy has considerable effects on the spin chain when it appears together with the frustration. We introduce some previous numerical results here in the $S = 1$ anisotropic J_1-J_2 model. For antiferromagnetic nearest- and next-nearest-neighbor interactions as in Sec. 2.1.5, the exchange anisotropy allows the frustrated system to have another spontaneous symmetry-broken phase, the chirality phase which is not shown in the unfrustrated or anisotropic spin chains [78, 79]. The Z_2 symmetry is broken in this phase, and it shows a long range order of chirality which is defined by

$$\hat{\kappa}_i^z \equiv \hat{z} \cdot (\hat{\boldsymbol{S}}_i \times \hat{\boldsymbol{S}}_{i+1}) = \hat{S}_i^x \hat{S}_{i+1}^y - \hat{S}_i^y \hat{S}_{i+1}^x. \,. \tag{2.72}$$

The chiral phase is also invariant under the time-reversal operation and shows no magnetic long range order. The phase diagram in the J_2-J_z plane from Ref. 78 is

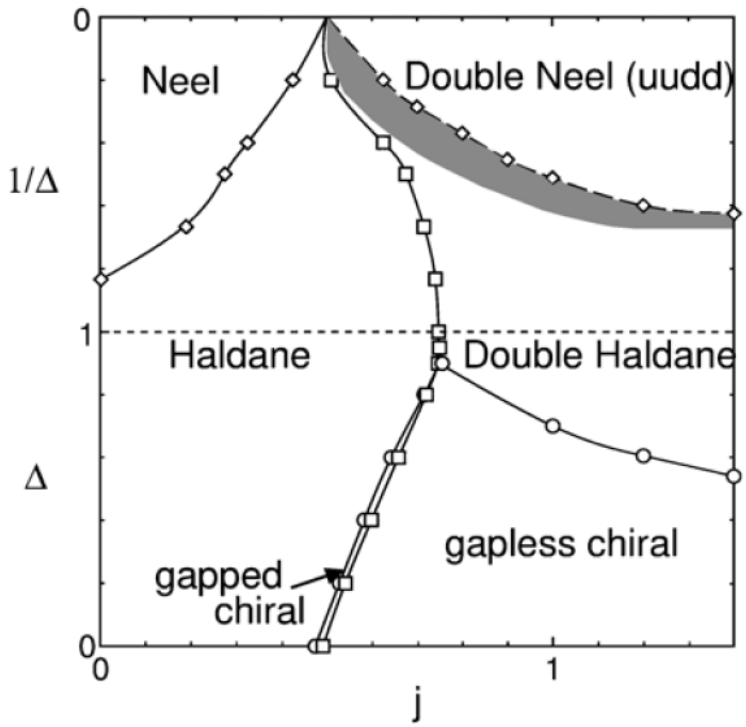

Figure 2.7: Phase diagram of the J_1-J_2 model with exchange anisotropy in J_2-J_z plane from Ref. 77. The notation is different from ours and j and Δ mean J_2 and J_z, respectively.

shown in Fig. 2.7. Two different chiral phases appear in the anisotropic frustrated spin-1 chain. One is the gapless chiral phase which shows the spin-spin correlation function decaying algebraically. The other is the gapped chiral phase with the exponentially decaying spin-spin correlation function. The gapless chiral phase is located in a very narrow region between the Haldane and gapped chiral phases.

The J_1-J_2 model with the single-ion anisotropy exhibits a much more complicated phase diagram [77]. For positive single-ion anisotropy strength, the region

of the gapless chiral phase becomes larger and two new phases called the chiral-large-D phase and the chiral-Haldane phase appear. The chiral-large-D phase is characterized by the gap and the chirality order, and the chiral-Haldane phase is characterized by the Haldane gap with the finite string order parameter as well as the chirality order. The frustration helps the anisotropy the spontaneous symmetry-breaking occur.

2.2 Experiments on spin-1 chain systems

In condensed matter physics, experimental realization is very important because not only does it further develop the theoretical considerations, but it also supports it very quickly, and vice versa. Extensive experimental studies have been conducted for decades after the development of experimental techniques for the magnetic structure of materials such as electron spin resonance and neutron scattering. In this section, we will review several relevant materials of one-dimensional spin-1 systems, such as NENP [80–88], $CsNiCl_3$ [89–92], $NaV(WO_4)_2$ [93], Y_2BaNiO_5 [94–98], and ANi$_2$V$_2$O$_8$ (A=Pb, Sr) [99–104], briefly.

$Ni(C_2H_8N_2)_2NO_2ClO_4$ (NENP)

It has been well-known that $Ni(C_2H_8N_2)_2NO_2ClO_4$ (Nickel ethylenediamine nitrite perchlorate or NENP) is one of the spin-1 chain materials since the material was studied in 1982 [80]. Not only was evidence of the Haldane gap shown [81–83, 88], but evidence for the spin-1 chain described by the AKLT state was also presented [84–87]. The crystal structure of the NENP at low temperature is shown in Fig. 2.8. Hagiwara *et al.* substituted a small amount of Ni^{2+} by Cu^{2+} as impurities, which cause some the singlet bonds to break [84]. (Glarum *et al.* also used non-magnetic impurities such as Zn^{2+}, Cd^{2+}, and Hg^{2+} [85].) Then, they found that $S = 1/2$ degrees of freedoms are induced additionally by using the electron spin resonance (ESR) technique. This result supports that the Ni-ions with $S = 1$ spin composes the chains and each chain with open boundary has fractionalized $S = 1/2$ spins on each edge as described by the AKLT state. Its

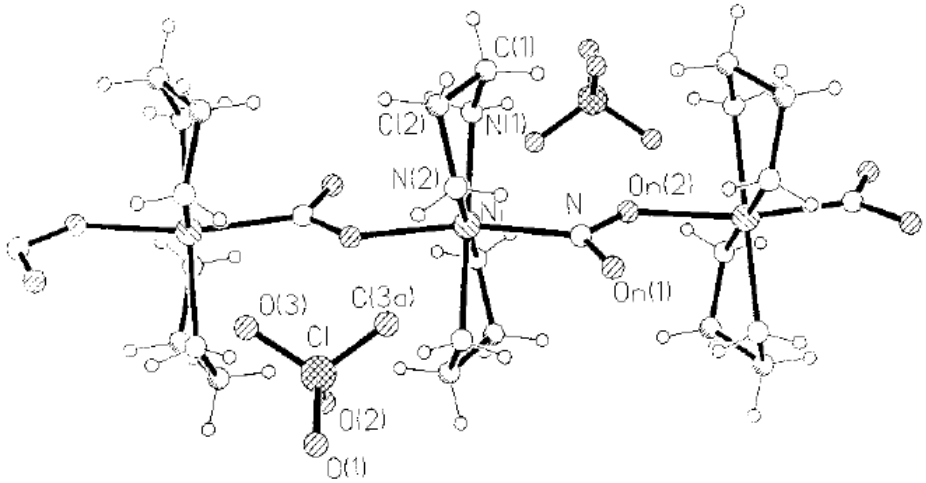

Figure 2.8: Low-temperature crystal structure of NENP from Ref. 105. Ni-ions compose the spin-1 chains along the horizontal direction.

schematic representation is shown in Fig. 2.9. The excitation and the dynamic correlation function were also studied with inelastic neutron scattering experiments [86]. They showed that the data is consistent with the numerical result and there is a peak of structure factors at $q = \pi$.

$CsNiCl_3$

In $CsNiCl_3$, Ni^{2+} ions also has a $S = 1$ spin moment and constitute chains as the crystal structure is shown in Fig. 2.10. This material is described by a set of antiferromagnetically interacting chains in which the strength of the interchain interaction is very weak ($J'/J \simeq 0.02$ and $J = 2.28$meV [106]). It correspondingly shows the excitations with the Haldane gap above the Néel temperature $T_{\mathrm{N}} \simeq$

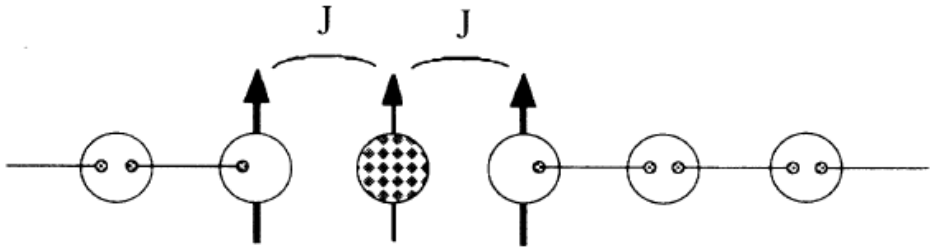

Figure 2.9: Schematic representation of the AKLT state when substituted by an impurity taken from Ref. 84. From the AKLT state described in Fig. 2.2, one of singlet bonds is broken by a $S = 1/2$ Cu^{2+} ion. Resulting three $S = 1/2$ spins will interact.

$4.8K$ by using the technique of neutron scattering [89, 90, 92, 92]. The fitting result gives the Haldane gap of $0.54(2)J = 0.124(4)$ meV [92] which higher than the theoretically predicted value, possibly due to an additional renormalization from the weak interchain coupling. The enhancement of the gap shows that the interchain is coupling of $CsNiCl_3$ is weaker than that of NENP. The Ni-ions has its spin structure with π phase along the chain direction Its spin-spin correlation length was obtained as 5-8 sites at 9K [90] and 4.0(2) sites at 6.2K [92], which is explained by the weakly coupled spin-1 chains. Above the Haldane gap, the well-defined excitation is observed as multiparticle continuum which resemble the spinon continuum from the spin-1/2 antiferromagnetic chains [92].

Other compounds

The compound $NaV(WO_4)_2$ has been considered to be a system of zigzag spin chains with the exchange interaction of $J \simeq 15.5$meV [93]. It manifests a spin

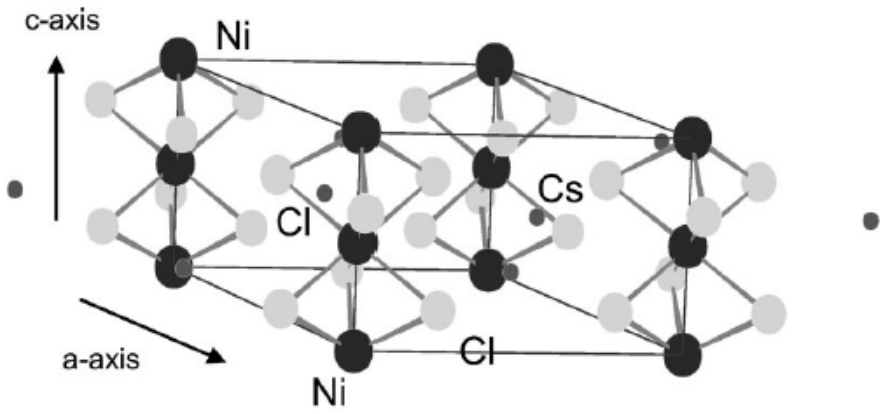

Figure 2.10: Structure of $CsNiCl_3$ taken from Ref. 92. Ni-ions compose the spin-1 chains along the c-axis.

gap in the magnetic susceptibility. The antiferromagnetic fluctuation from $S = 1$ spins gives a broad maximum in the data and a minimum value at $T \sim$10 K, signifying that the paramagnetic region appears. The fitting result without consideration of anisotropy shows that the values of the gap is $\sim 0.14J$ ($J \simeq$ 15.5 meV) which is smaller than the prediction from the theory. They suggest that this is attributed by weak couplings between the chains presumably. Inelastic neutron scattering experiments on Y_2BaNiO_5 shows that it is also one of quantum spin-1 chains with the Haldane gap [95, 96]. Like other Haldane chain materials, $S = 1/2$ spins induced from nonmagnetic impurities are also confirmed by NMR experiments [97]. They are also found in the form of singlets and triplets [94]. When there are many Haldane chain segments at high doping concentrations, the resulting triplet modes exist inside the Haldane gap with a Friedel oscillation under magnetic field [98]. Its exponential decay length is 8(1) sites which is

similar to that of the exponential spin-spin correlation in the AKLT state as is pointed out in Ref. [40].

Measurements of magnetic properties of $A\mathrm{Ni_2V_2O_8}$ have shown that it is described as the Haldane gapped phase without long-range order. The inter-chain exchange interaction is small enough that the systems can not have 3D magnetic ordering at low temperature. Doping non-magnetic impurities to $\mathrm{PbNi_2V_2O_8}$ [99] and $\mathrm{SrNi_2V_2O_8}$ [107] induces a magnetically ordered state due to the strong interchain interactions. It is shown that $\mathrm{SrNi_2V_2O_8}$ is in the paramagnetic state down to 3.75 K [102] and that the material is in the Haldane phase by considering the anisotropic effect with other materials of $\mathrm{BaNi_2V_2O_8}$ and $\mathrm{CaNi_2V_2O_8}$ [103].

Chapter 3

Methods

3.1 Density-matrix renormalization-group (DMRG)

Since White suggested a method to obtain thermodynamic ground state by using density-matrix and improved the renormalization group approach [9, 10], this method, so-called the "density-matrix renormalization-group (DMRG)" method has been one of the powerful tools in the strongly correlated systems.

In many-particle systems, we may take a Hilbert space of very large dimension which is about x^N (x is the number of degrees of freedom of a particle). It is impossible to treat all vectors of the huge Hilbert space in the thermodynamic limit. We have, however, known the fact that many of these vectors do not play an important role in determining properties of systems. What we want to know in condensed matter physics is mainly related to their ground state(s) and low-lying states which take a relatively small part of the Hilbert space. The DMRG method gives us the ground state(s) (and a few low-lying states) in a spirit of coarse-graining the irrelevant degrees of freedom as in the RG approach.

Let me give a brief overview on the DMRG. We first take and keep a part of a basis which contributes to a ground state dominantly from small size to large. We then add two sites to the system and construct the Hamiltonian matrix of the enlarged system by combining the kept and the additional basis states. From this Hamiltonian, we obtain a ground state of the enlarged system and iterate the above procedure until the system gets a size that we want to calculate. As a result, we have a ground state of very large size of the system with approximation. More details about the DMRG calculation will be explained in the following sections. (See also Ref. 108–111 for more information.)

3.1.1 Ground state and Truncation

As we mentioned above, we start with a small system of size L which can be calculated exactly instead of large size of system. We give an example of the system of its size $L = 4$ in Fig. 3.2. From the Hamiltonian $\mathcal{H}_L$ of this small system, we can obtain its exact ground state $|\phi_0; L\rangle$ or low-lying states by using the exact diagonalization or the Lanczos method etc. The resulting ground state is expressed by a linear combination of direct products of single-site states as

$$|\phi_0\rangle = \sum_{s_1,s_2,\cdots s_L} C_{s_1,s_2,\cdots s_L} |s_1\rangle|s_2\rangle \cdots |s_L\rangle \ , \tag{3.1}$$

where $|s_i\rangle$ can be any single-particle state at ith site and we consider it as a spin state. In spirit of the renormalization group approach, we want to truncate the Hilbert space of the system and take the relevant part of the thermodynamic ground state. The DMRG, however, will use only the ground state of the small

size system to obtain that of large size systems without the excited states. In order to do this, we first need to partition the system into two segments with equal size in order to perform the truncation. We call each segment "a block", especially, the segment on the left is called the "system" block and the other is called the "environment" block as shown in Fig. 3.2. The Hamiltonian can also be divided into three parts as

$$\mathcal{H}_L = \mathcal{H}_S^{L/2} + \mathcal{H}_E^{L/2} + \mathcal{H}_{SE} \tag{3.2}$$

where S and E denotes the system and environment blocks, respectively, and $\mathcal{H}_{SE}$ is the interaction term between them. The ground state is then rewritten as

$$|\phi_0\rangle = \sum_{i_S} \sum_{i_E} [\Phi]_{i_S i_E} |i_S\rangle |i_E\rangle \tag{3.3}$$

where $|i_S\rangle = |s_1, \cdots, s_{L/2}\rangle$ and $|i_E\rangle = |s_{L/2+1}, \cdots, s_L\rangle$. The DMRG concentrates only on the system block and its states relevant to the ground state. If you trace out the environment block states, you can obtain and choose the basis states of the system block which are more contributing to the ground state. More specifically, you need to construct a density matrix of the ground state ρ from the density operator $\hat{\rho}$ as

$$\hat{\rho} = |\phi_0\rangle\langle\phi_0| = \sum_{i,j} [\rho]_{ij} |i\rangle\langle j| \tag{3.4}$$

where $|i\rangle = |i_S\rangle \otimes |i_E\rangle$. It shows that how the ground state is decomposed in the $|i \rightarrow$-basis states. But we want to know the contribution of the system block. This can be accomplished by just tracing out the environment block states from

the density matrix so that the basis state of the system block remains. We call the resulting density matrix the reduced density matrix of the system block ρ_S.

The reduced density matrix is written as

$$\hat{\rho}_S \equiv \mathrm{Tr}_E\ \hat{\rho} = \sum_{i_E} \langle i_E | \hat{\rho} | i_E \rangle = \sum_{i_S, j_S} |i_S\rangle [\rho_S]_{ij} \langle j_S| \ . \tag{3.5}$$

It is now expressed in terms of the system block states $|i_S \rightarrow$. Now we have to extract the relevant part and truncate the Hilbert space. Diagonalization of ρ_S with a unitary transformation and a unitary matrix U gives eigenstates (good basis states), i.e.

$$\hat{\rho}_S = \sum_{k,k'} \sum_{i_S, j_S} [U^\dagger]_{ki} |\tilde{\rho}_k\rangle [\rho_S]_{ij} \langle \tilde{\rho}_{k'}| [U]_{jk'} \tag{3.6}$$

$$= \sum_{k=1}^{M_S} \sum_{k'=1}^{M_S} [U^\dagger \rho_S U]_{kk'}\ |\tilde{\rho}_k\rangle \langle \tilde{\rho}'_k| \tag{3.7}$$

$$= \sum_{k=1}^{M_S} \tilde{\rho}_k\ |\tilde{\rho}_k\rangle \langle \tilde{\rho}_k| \tag{3.8}$$

where $|\tilde{\rho}_k\rangle$ denotes an eigenstate of ρ_S with eigenvalue $\tilde{\rho}_k$ and M_S is the dimension of the Hilbert space of the system block. The eigenvalues represent the probability of the eigenstates on the ground state. Listing these eigenstates and sorting them by descending order of their eigenvalues, we choose and keep the first m eigenstates as basis vectors. We will neglect the other eigenstates, since the eigenstates with large probability value $\tilde{\rho}_k$ ($\tilde{\rho}_k \geq 0$) play a more crucial role in constructing the ground state. The remaining basis vectors span a m-dimensional subspace. The truncation procedure will be completed after projecting all matri-

$$U^t = \left[\left\{ \tilde{\rho}_1 \right\} \cdots\cdots \left\{ \tilde{\rho}_{M_S} \right\} \right] \quad \rightarrow \quad T^t = \left[\left\{ \tilde{\rho}_1 \right\} \cdots\cdots \left\{ \tilde{\rho}_m \right\} \right]$$

Figure 3.1: Sketch of obtaining the truncation matrix T from the unitary matrix U. We show the matrices transposed for the sake of convenience, and each column vector denotes one of eigenvectors of the reduced density matrix ρ_S. We keep the first m column vectors with large eigenvalue $\tilde{\rho}_k$ of ρ_S (or large probability $\tilde{\rho}_k$) and decimate the others from U when $m \leq M_S$. Finally, we have the $m \times M_S$ truncation matrix T.

ces of the local operators of the system block including the Hamiltonian onto the resulting subspace.

In the actual calculations, we need to consider a truncation matrix T to represent the projection (or the truncation) It will be obtained from the $M_S \times M_S$ matrix U which represents the transformation of $\{|i_S\rangle\}$ to $\{|\tilde{\rho}_k\rangle\}$. Taking only the m basis vectors means that only m row-vectors with large $\tilde{\rho}_k$ in U are taken and gives the $(m \times M_S)$-dimensional matrix T as

$$\hat{T} = \sum_{i=1}^{m} \sum_{j=1}^{M_S} [T]_{ij} |\tilde{\rho}_i\rangle\langle j_S| \ . \tag{3.9}$$

This is schematically illustrated in Fig. 3.1. All we have to do is to project all the matrices of the system block that we are interested in into the truncated Hilbert space as in the following way :

$$O \rightarrow \tilde{O} \equiv TOT^\dagger \ . \tag{3.10}$$

The truncation can be interpreted that we approximate the Hilbert space of the

system block by only taking the relevant basis states to the ground state

After the truncation procedure, we can have the Hamiltonian matrix $\tilde{\mathcal{H}}_S^{L/2}$ from $\mathcal{H}_E^{L/2}$. Similarly, the environment block can also be obtained by tracing out the system block's states and truncating it as in Eq. (3.8). We now add two more sites to the total system with the truncation. It gives a new total system of size $L+2$ (which is usually called "a superblock"). This procedure is illustrated in Fig. 3.2. The rectangular box in Fig. 3.2 means that we deal with the enclosed sites in the truncated Hilbert space. We can construct the Hamiltonian operator of the new superblock as follows :

$$\hat{\mathcal{H}}_{L+2} = \hat{\mathcal{H}}_S^{L/2} + \hat{\mathcal{H}}_{S\sigma_1} + \hat{\mathcal{H}}_{\sigma_1\sigma_2} + \hat{\mathcal{H}}_{\sigma_2 E} + \hat{\mathcal{H}}_E^{L/2} \tag{3.11}$$

in which σ_1 and σ_2 denote the two additional sites, and $\mathcal{H}_{\alpha\beta}$ is an interaction term between α block (or site) and β block (or site). In fact, each term of the Hamiltonian will be represented in the direct product of the truncated states and the inserted spin states

$$|\tilde{\rho}_i^S\rangle \otimes |\sigma_1\rangle \otimes |\sigma_2\rangle \otimes |\tilde{\rho}_j^E\rangle \tag{3.12}$$

i.e.

$$\hat{\mathcal{H}}_S^{L/2} \rightarrow \tilde{\mathcal{H}}_S^{L/2} \otimes \mathbb{I}_{\sigma_1\sigma_2 j_E} \tag{3.13}$$

$$\hat{\mathcal{H}}_E^{L/2} \rightarrow \mathbb{I}_{i_S\sigma_1\sigma_2} \otimes \tilde{\mathcal{H}}_E^{L/2} \tag{3.14}$$

$$\hat{\mathcal{H}}_{S\sigma_1} \rightarrow \tilde{\mathcal{H}}_{S\sigma_1} \otimes \mathbb{I}_{\sigma_2 j_E} \tag{3.15}$$

$$\hat{\mathcal{H}}_{\sigma_1\sigma_2} \rightarrow \mathbb{I}_{i_S} \otimes \tilde{\mathcal{H}}_{\sigma_1\sigma_2} \otimes \mathbb{I}_{j_E} \tag{3.16}$$

$$\hat{\mathcal{H}}_{\sigma_2 E} \rightarrow \mathbb{I}_{i_S\sigma_1} \otimes \tilde{\mathcal{H}}_{\sigma_2 E} \tag{3.17}$$

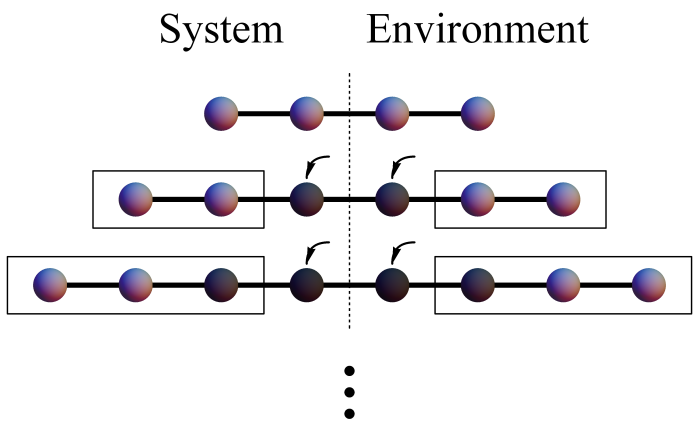

Figure 3.2: Partitioning of total systems of size $L = 4, 6$, and 8 for the truncation step in the DMRG. Each rectangular box is come from the sites of the above system block and means that irrelevant parts of the Hilbert space are removed. The environment block is also truncated, but we will copy the system block into the environment block as long as the Hamiltonian has reflection symmetry.

where $\mathbb{I}_\alpha$ is an identity matrix in the space spanned by $\{|\alpha\rangle\}$, and $i_{S(E)}$ denotes $\tilde{\rho}_i^{S(E)}$. Finally we calculate the ground state(s) of the superblock and its energy. We will iterate the above procedure by substituting L for $L' = L + 2$ until we get the system size that we want as shown in Fig. 3.2. The DMRG method sometimes does not need to calculate the truncation of the environment block as we explained. Instead, it can be accomplished by copying the system block to the environment one as long as the total system keeps the reflection symmetry in one-dimensional system. This will also reduce the cost to the DMRG process. The thermodynamic ground state and its energy can be approximated to the obtained ground state when $L \to \infty$.

The truncation basically has an error estimated by

$$\varepsilon \equiv 1 - \sum_{i=1}^{m} \tilde{\rho}_i \ . \tag{3.18}$$

We have $0 \leq \varepsilon < 1$ by the definition of Eq. (3.8). (When we take $m = M_S$, we get $\varepsilon = 0$. $\sum_{i=1}^{M_S} \tilde{\rho}_i = 1$) If the error becomes zero for every system size, we then have exact ground state in the thermodynamic limit. In this case, we will treat the entire Hilbert space i.e. $M_S = s^L$ where s is the number of degrees of freedom of a site. (Here, s is the spin number.) However, It is nearly impossible to calculate the ground state or the low-lying states in the thermodynamic limit because M_S becomes so large. The strategy of the DMRG method is now to increase m and extrapolate ε to 0 as possible as we can.

The approximated ground state has its energy with an error which is proportional to the truncation error ε. You must consider these errors and their extrapolations as well as the convergence of the iterations with increasing the system size. In order to have more accurate results, you need to first improve the precision of the ground state (or excited states which will be discussed later in Sec. 3.1.4.

3.1.2 Exact diagonalization

In the previous section, we mentioned that the Hamiltonian can be diagonalized and its ground state(s) (or a few low-lying states) can be obtained. We explain in this section that how we obtain them numerically in detail. We use one of diagonalization methods, the Lanczos method [112]. This helps us to find eigenstates

of the smallest (or the largest) eigenvalue of some operators approximately. We focus on the smallest eigenvalues because we are interested in the ground state.

If you know the Hilbert space of the system and construct the Hamiltonian matrix you first choose the target space and its states. This target space can be reduced or more specified by symmetries or boundary conditions, which will be discussed later in Sec. 3.1.5. Once you choose its basis states, you need to consider an initial guess of the ground state. Its probability amplitudes and their signs are determined by random numbers. We can express this as :

$$\varphi_0 = \sum_j C_j |\psi_j\rangle \tag{3.19}$$

where $|\psi_j\rangle$ is the basis states and C_j is its probability amplitude. The normalization condition is also necessary, $\sum_j |C_j|^2 = 1$. This state is not the same as the exact ground state of the system, $|\phi_0\rangle$ indeed i.e. $|\phi_0\rangle \neq |\phi_0\rangle$. We next operate the Hamiltonian to the initial state $|\varphi_0\rangle$. It produces a new state different from the initial state as

$$|\varphi_1'\rangle = \mathcal{H}|\varphi_0\rangle \tag{3.20}$$

$$= \sum_j C_j' |\psi_j\rangle \tag{3.21}$$

where $C_j' \equiv E_j C_j$ and E_j is the energy eigenvalue of $|\psi_j\rangle$. Note that $|\varphi_1\rangle$, however, includes the components of $|\varphi_0\rangle$ and does not have a unit norm. We subtract the component parallel to $|\varphi_0\rangle$ by the Gram-Schmidt decomposition as

$$|\varphi_1'\rangle \to |\varphi_1'\rangle - |\varphi_0\rangle\langle\varphi_0|\varphi_1'\rangle \ . \tag{3.22}$$

After a normalization we have a new orthogonal state

$$\varphi_1 \equiv \frac{|\varphi_1'\rangle - |\varphi_0\rangle\langle\varphi_0|\varphi_1'\rangle}{\langle\varphi_1'|\varphi_1'\rangle} \ . \tag{3.23}$$

You can expand a Hilbert space by these orthogonal states, which is a kind of so-called the Krylov subspace. We choose only two states - $|\varphi_0\rangle$ and $|\varphi_1\rangle$ - as basis states. This is the modified Lanczos method. In this subspace spanned by two basis vectors, you will have the Hamiltonian as

$$H = \begin{pmatrix} H_0 & H_{01} \\ H_{10} & H_1 \end{pmatrix} \tag{3.24}$$

where

$$H_0 \equiv \langle\varphi_0|\hat{H}|\varphi_0\rangle \tag{3.25}$$

$$H_{01} \equiv \langle\varphi_0|\hat{H}|\varphi_1\rangle \tag{3.26}$$

$$= H_{10}^* \tag{3.27}$$

$$H_1 \equiv \langle\varphi_1|\hat{H}|\varphi_1\rangle \ . \tag{3.28}$$

You can find its eigenstates with eigenvalues exactly and choose one eigenstate with the lowest eigenvalue. This state has an amplified component of the exact ground state. We then set the new state as the initial state $|\varphi_0$ and iterate the above procedure. You will finally have a state converging to the exact ground state after a lot of or some iterations. We take a criterion for convergence as overlaps and energy differences between the ground states of the iteration steps, which means that you find the invariant subspace of the Hilbert space and its

basis.

Generally, you can make the Krylov subspace of n-dimension ($n \geq 3$). It is called the band Lanczos method. Obtaining a new orthonormal state φ_i can be generalized from Eq. (3.23) as

$$\varphi_i = \frac{|\varphi_i'\rangle - \sum_j |\varphi_j\rangle\langle\varphi_j|\varphi_i'\rangle}{\langle\varphi_i'|\varphi_i'\rangle} \ . \tag{3.29}$$

One can obtain the following relation :

$$H\varphi_i = \beta_{i-1}|\varphi_{i-1}\rangle + \alpha_i|\varphi_i\rangle + \beta_i|\varphi_{i+1}\rangle \ . \tag{3.30}$$

A set of these orthonormal states forms a basis and has a tridiagonalized Hamiltonian matrix as

$$H = \begin{pmatrix} \alpha_1 & \beta_1 & & & \\ \beta_1 & \alpha_2 & \beta_2 & & \\ & \beta_2 & \alpha_3 & \ddots & \\ & & \ddots & \ddots & \beta_{n-1} \\ & & & \beta_{n-1} & \alpha_n \end{pmatrix} \ . \tag{3.31}$$

This Hamiltonian matrix can be diagonalized by the QR decomposition (which is omitted in this dissertation). The band Lanczos method will reduce the number of iterations and to deal with degeneracy of the low-lying states well at a cost of obtaining the enlarged basis and diagonalizing their Hamiltonian matrix.

3.1.3 Physical quantities

After the ground state is obtained in the way described in Sec. 3.1.1, we need to proceed to analyze physical properties of the system. We discussed only one of them, the energy value in the previous section which is just followed by updating the Hamiltonian and calculating the ground state. Most operators that we want to study are projected as we explained in Eq. 3.10. Onsite terms such as $\langle \hat{O}_i \rangle$ or matrices $O_i \equiv \sum_{\alpha,\beta} [O_i]_{\alpha\beta} \equiv \langle \alpha | O_i | \beta \rangle$ which are defined at ith-site can be applied and projected easily. The iteration procedure will give their matrix transformations as

$$O_i \to \tilde{O}_i \to \tilde{\tilde{O}}_i \ . \tag{3.32}$$

On the other hand, there is a caution on the transformation of other operators composed of multiple sites, for example, $\hat{O}_i \hat{O}_{i'}$. For these operators, their matrix should be transformed as a whole, not separately. Namely, if we define $\hat{V}_{i,i'} \equiv \hat{O}_i \hat{O}_{i'}$, its matrix $V_{i,i'}$ follows

$$V_{i,i'} \to \tilde{V}_{i,i'} \equiv \sum_{\alpha,\beta} [\widetilde{V_{i,i'}}]_{\alpha,\beta} \tag{3.33}$$

and

$$O_i O_{i'} \to (\widetilde{O_i O_{i'}}) \ . \tag{3.34}$$

Note that

$$O_i O_{i'} \nrightarrow \tilde{O}_i \tilde{O}_{i'} \ . \tag{3.35}$$

If you use the transformation as in Eq. (3.35), it gives a wrong answer which becomes close to zero almost. This is because $\hat{T}$ is not unitary ($T^\dagger T$ is not the identity matrix).

In addition to the above examples, you may also consider new operators including a site(s) with truncation and the added site(s). These operators shows a matrix transformation as follows :

$$\widetilde{O_i O_{i'}} O_{i''} \rightarrow \left(\widetilde{\widetilde{O_i O_{i'}} O_{i''}} \right) \ . \tag{3.36}$$

Here, each matrix should also be projected as a whole.

3.1.4 Excited states

So far, we have focused only on the ground state calculation. If you, however, want to calculate low-lying states (or excited states around the ground states), two additional steps are needed from the DMRG procedure we explained above. One is that when you calculate the ground state ϕ_0 for a given system size at first, you should also calculate more and find excited states as many as you want. Secondly, constructing a reduced density matrix from these excited states as well as from the ground state, you have to take its relevant basis vectors with large probability. A transformation matrix to the truncated Hilbert space can be obtained as in Eq. (3.9). The resulting reduced density matrix is written as

follows :

$$\rho_S \to \sum_{i=0} c_i |\phi_i\rangle\langle\phi_i| \tag{3.37}$$

where ϕ_i ($i \geq 1$) denotes the excited states and c_i is their probability ($\sum_i c_i = 1$). It is known that there is no optimal choice of c_i. However, equally-weighted probability distribution is regarded as reasonable one empirically. If you consider only a few excited states without ground state and project them separately, it may give best results for each states.

3.1.5 Physical considerations

When you calculate the ground state(s) (or excited states) and truncate the Hilbert space, some informations will help you to obtain more accurate results efficiently, for example, symmetry, degeneracy, boundary condition, etc. They reduce the computational cost of the calculations. As a result, it allows us to get larger values of m and higher accuracy of the states. In the followings, we will discuss about how symmetry can be applied to the DMRG calculation and how boundary conditions can affect the calculation in detail, which is expected to give better results.

Symmetry

We first consider symmetry in the Hamiltonian for given system. Symmetry can give informations about the Hilbert space of the system. If we know what symmetry lies in the Hamiltonian, we can classify its subspaces according to the

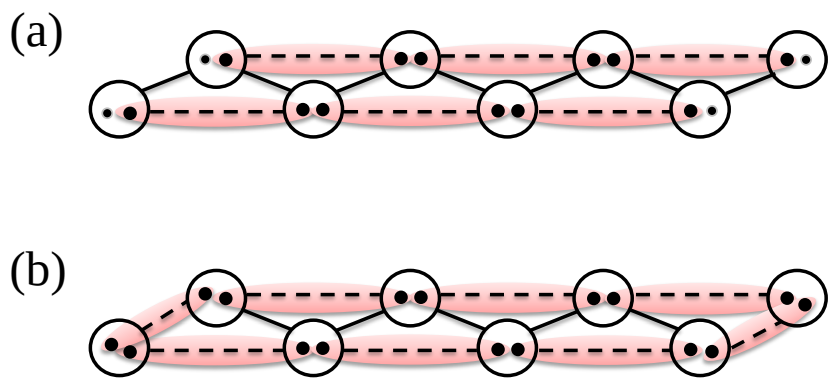

Figure 3.3: Schematic representations of the AKLT state adopted in our model. The filled circles, the dashed lines, the solid lines, and the shaded regions denote the $S = 1/2$ spins, the antiferromagnetic couplings, the ferromagnetic couplings, and the singlet bonds, respectively. (a) The usual open boundary condition gives rise to the edges containing the free spins which do not participate in the singlet bond. Its free spins cause the degeneracy that we are not interested in. (b) The modified open boundary condition we employed excludes the above free spin problem. Each ferromagnetic coupling between the two end sites is replaced by the antiferromagnetic one. This gives a marked improvement in the cost of the DMRG.

good quantum numbers which are separated with each other. It helps us to restrict the target subspace to the smaller one. We are then able to focus more efficiently on the subspace we are actually interested in. The ground state and the excited states will be determined after a comparison of the energy for each subspace.

For instance, let us consider a system with a rotational symmetry or a gauge symmetry which preserves the total angular momentum or the particle number, respectively. We can take operators such as S, S^z, or N, etc. which commute

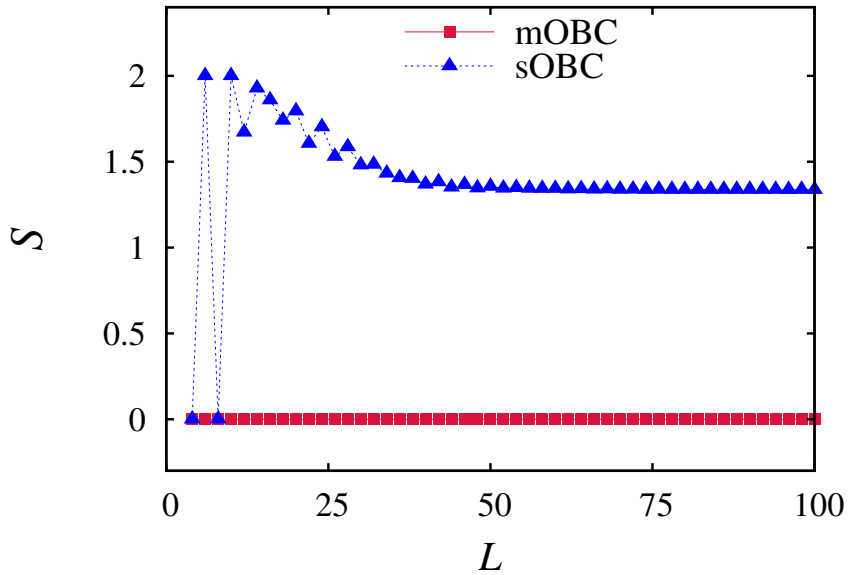

Figure 3.4: (Color online.) Total spin of ground states of the antiferromagnetic spin-1 chains for the mOBC (square) and the sOBC (triangle). The sOBC shows finite total spin value resulted from the fractionalized edge spins while the mOBC has zero total spin. It means that the degeneracy is lifted and we can focus only on the bulk state efficiently.

with the Hamiltonian. Each operator shows the conservation law in the truncation process. The eigenstates of the density matrix (Eq. (3.5)) have eigenvalues of these conserved quantities. In the reduced density matrix, its eigenstates also remains these conserved quantities as eigenvalues because tracing out the environment is taken by their eigenstates. Let us consider the ground state which has S^z (or N_{particle}), it then satisfies $S^z = S^z_S + S^z_E$. After tracing out the environment states, there are still the eigenstates of $\hat{S}^z$ with eigenvalues S^z_S. Therefore, the block diagonalized density and Hamiltonian matrices is kept in all the DMRG

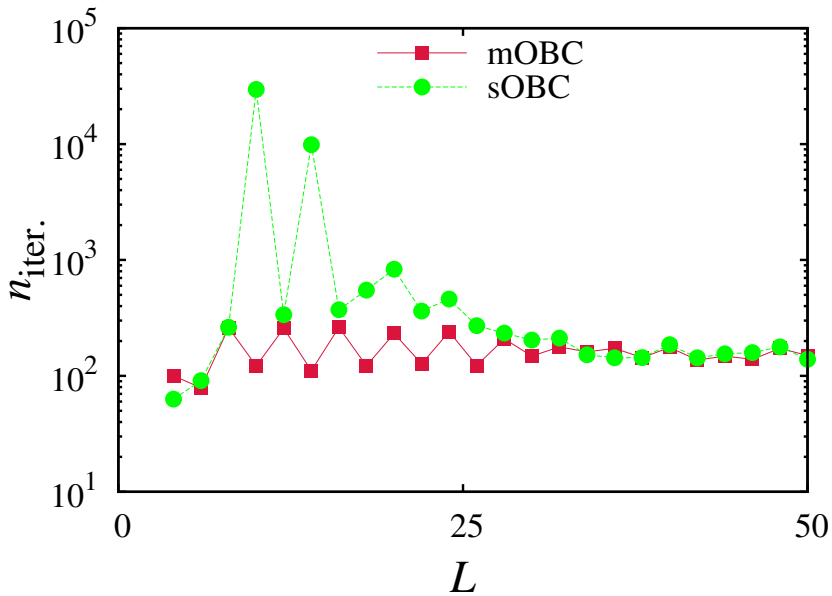

Figure 3.5: (Color online.) Number of iterations for the antiferromagnetic spin-1 chains with the mOBC (squares) and the sOBC (circles). Much more iterations are needed for the sOBC than for the mOBC. It causes the high computational cost problem in the DMRG.

steps.

Boundary condition

There is another efficient way to calculate the ground state more accurately and quickly. This is an employment of appropriate boundary conditions to systems We give an example of the antiferromagnetic spin-1 chain systems that we will discuss in Sec. 4. Within the Heisenberg exchange model the system is known to have a unique ground state in the thermodynamic limit. However, it has gapless edge excitations from the standard open boundary conditions (sOBC). Following

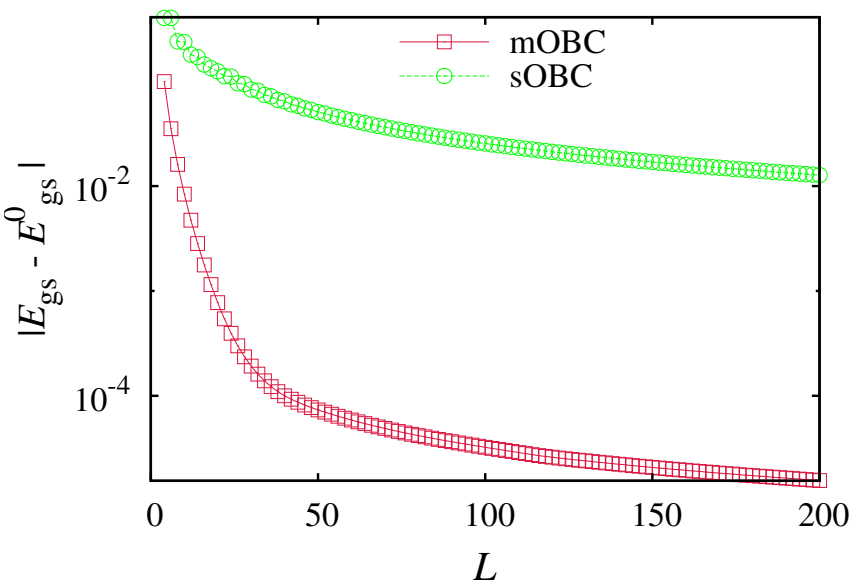

Figure 3.6: (Color online.) Difference between the ground state energies and the converged value for the antiferromagnetic spin-1 chains with the mOBC (squares) and the sOBC (circles).

the AKLT description adopted suitably to the ground state in our system, we expect that there are singlet bonds between sites by antiferromagnetic couplings. If we use the sOBC shown in Fig. 3.3(a), the edges have free spins which are not participating in the singlet bond with one of neighboring sites. They make the gapless excitation. Each DMRG step considers the finite-size systems, so we will encounter a problem from degeneracy. It increases the cost of the calculations and gives relatively inaccurate results. To solve this problem, we lift the degeneracy from the edge by a modified open boundary condition (mOBC) as shown in Fig. 3.3(b). It arises that the edge free spins form singlets artificially and the final ground state will show zero total spin. We plot the data of the total spin

of the ground state for each OBCs in Fig. 3.4. The mOBC shows total spin zero while the sOBC has finite total spin value. In the sOBC, the four edge $S = 1/2$ spins (Fig. 3.3(a)) will be represented by a direct product of the spin states and the angular momentum addition : $\frac{1}{2} \otimes \frac{1}{2} \otimes \frac{1}{2} \otimes \frac{1}{2} = (0 \oplus 1) \otimes (0 \oplus 1) \rightarrow 0 \oplus 1 \oplus 2$. This is because the ground state for the sBOC has to show the total spin in the range between 0 and 2. It confirms that the edge free spins are participating in the ground state for the sOBC and we suitably lift the degeneracy with the mOBC. We thus can focus only on the bulk state for the mOBC efficiently.

In order to check if the mOBC allows us to calculate and obtain the ground state in an efficient way, we compare the number of iterations of finding the ground state in the Lanczos procedure. The sOBC has much more iterations than the mOBC has as shown in Fig. 3.5. The computational cost of the DMRG is proportional to the number of the Lanczos iterations significantly and becomes much larger for the sOBC than for the mOBC. We also show that the accuracy of the calculation varies. We plot differences between the ground states energy and the converged one as a function of the system size in Fig. 3.6. The difference for the mOBC shows a rapid decrease at first small size and becomes close to the converged value. On the other hand, the sOBC shows the difference two orders of magnitude larger than that of the mOBC. For fixed system sizes, not only the number of iterations surges, the accuracy of the ground state is also reduced. The computational cost problem is much more compounded for the sOBC. It is thus important to reduce the degeneracy and the subspace by appropriate boundary conditions as well as symmetry considerations It will help us to concentrate on what we have an interest in and examine the systems more efficiently, accurately,

and energetically.

3.1.6 Optimizations

Accurate ground state and its energy can be obtained by increasing m (the number of kept states in the truncation process) with its extrapolation of $m \to \infty$. Furthermore, we have to iterate the calculation until the system gets a size sufficiently large that we are interested in. You, however, may have a problem of long-time calculations for obtaining high accuracy or treating a large number of data from large system sizes. It means that we need to utilize all computing resources in an efficient way during the DMRG calculations. In this section, we will explain technical details in our numerical calculations which improve performance of the DMRG calculations to solve the above problem.

Memory-efficient algorithms

Generally, it is impossible to increase m excessively because of our limited computing resources. Particularly, if we take large m, the matrix will have a large number of components proportional to m^4, and we need more memory resources. In order to use memory more efficiently, we have used two ways of reducing the memory-use in the DMRG method. One is the sparse-matrix algorithm which allocate memory only for nonzero components of matrices. While the standard memory-allocation routines use memory addresses as indices of matrices (or arrays), the spare-matrix algorithm saves values of the nonzero components with their indices in the memory. It cuts down the memory requirements dramatically. In facts, more than 50% of the memory we have to access is reduced

in our calculations within the sparse-matrix algorithm. Additionally, it also removes unnecessary multiplications and additions of zero components and gives less round-off errors and more correct answers.

The other one is the matrix-product representations of operators [113]. In the DMRG process, the Hamiltonian of each block is projected and collected to form the superblock Hamiltonian. Instead of calculating the superblock Hamiltonian matrix in the basis of Eq. 3.12, keeping the representations in the form of the direct product and their order (or indices) will reduce the memory-usage and even computing time. Let us consider Eq. (3.11) as an example. After some DMRG iterations, we may see that $\tilde{\mathcal{H}}_S^{L/2}$ is a $m \times m$ matrix and acts as $\tilde{\mathcal{H}}_S^{L/2} \otimes \mathbb{I}_{\sigma_1\sigma_2 j_E}$ which is in fact $(m^2s^2) \times (m^2s^2)$-dimensional superblock matrix. But the superblock matrix is composed of just four copied blocks of $\tilde{\mathcal{H}}_S^{L/2}$. If $\tilde{\mathcal{H}}_S^{L/2}$ has a components, the superblock matrix will have $4a$ components, occupying more memory redundantly. So we need to keep the operator matrices in the form of the direct product which is called the "matrix-product operator". It helps us to increase m more and obtain more accurate results with its small truncation errors and better extrapolations.

Parallelization

Recent computer systems with multi-cores enable the parallelization of algorithms which divides a task and executes allocated parts of the code in each thread at the same time. It also cuts down the computing time substantially. Its ability is boosted by the number of cores, depending on an algorithm. We use one of the parallelization method, the OpenMP (open multi-processing) [114], in which

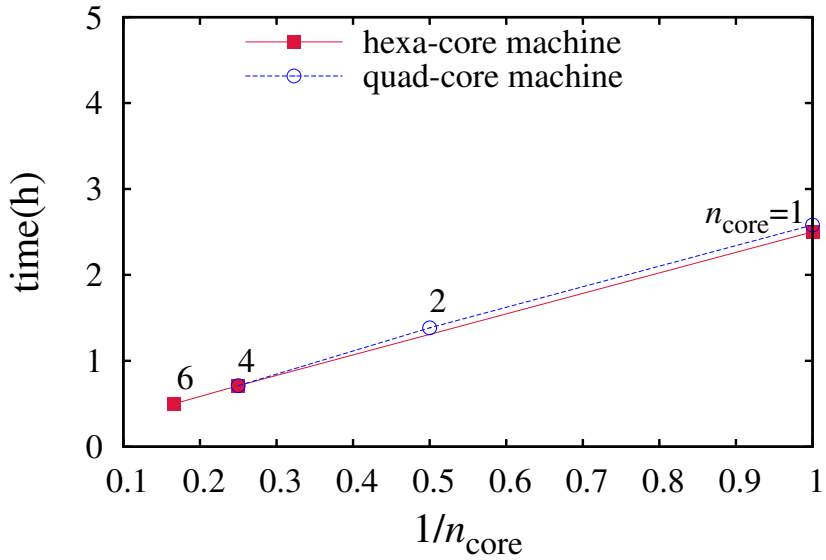

Figure 3.7: (Color online.) Computation time of one of our results (in Sec. 4) with the parallelization. It is plotted as a function of the inverse number of cores for the hexa-core machine (squares) and for the quad-core machine (circles). The linear reduction of the computation time is clearly shown as we the number of cores is increased.

each thread shares system memory in a node. In our codes, the parallelization is applied to divide the calculation of the superblock Hamiltonian into each sub-block part which is the most time-consuming process in the DMRG. We confirm that the total computation time of the code decreases and it is proportional to about $1/n$ (n: number of cores). You have to be careful about if you partition your tasks in a proper way and if each thread is running without idle processors. We plot one of our results of parallelization in Fig. 3.7. It clearly shows that the computation time reduces linearly as we increase the number of cores for two kinds of machines.

Eigenstate prediction

When performing the DMRG iterations with adding the new sites in between the blocks, it is useful to exploit the previous eigenstates of the system of small size in order to obtain eigenstates of the enlarged system [109, 115, 116]. This is because the resulting states tend to converge and resemble with states in the thermodynamic limit. The details are as follows. We use the system-block basis states with their probabilities after tracing out the environment block (Eq. (3.8). They are used to construct an initial guess of the new ground state of which composition is rarely changed and is expected to be very close to the new ground state. The new ground state is expected to be

$$|\phi_0^{L+2}\rangle \sim \sqrt{\tilde{\rho}_k^S}\sqrt{\tilde{\rho}_k^E} C_{\sigma_1} C_{\sigma_2}\ |\tilde{\rho}_k^S\rangle|\sigma_1\rangle|\sigma_2\rangle|\tilde{\rho}_k^E\rangle\ . \tag{3.38}$$

The signs of their probability amplitudes are determined randomly. The coefficients C_{σ_1} and C_{σ_2} can also be obtained up to the sign by tracing out the previous environment and system blocks from the density matrix of the ground state as

$$\mathrm{Tr}_{S^{L/2}E^{L/2}}|S\sigma_1\sigma_2E\rangle\langle S\sigma_1\sigma_2E|\ . \tag{3.39}$$

It enables the exact diagonalization to start with an initial state close to the ground state and reduce the number of the Lanczos iterations. The total computation time also decreases consequently.

3.2 Hartree-Fock approximation

We use another numerical method to treat the interaction between the particles in many-body systems. It is the Hartree-Fock approximation, one of the mean-field approaches, which turns out to yield the effective Hamiltonian of a single particle. As a result, it allows us to solve the problem rather easily and calculate the ground state. We apply the Hartree-Fock approximation to the Hubbard interaction of electrons ($S = 1/2$ fermions) as follows :

$$\begin{aligned}
\mathcal{H}_U &\equiv U \sum_i n_{i\uparrow} n_{i\downarrow} && (3.40)\\
&= U \sum_i c^\dagger_{i\uparrow} c_{i\uparrow} c^\dagger_{i\downarrow} c_{i\downarrow} \\
&\approx U \sum_i \Big[\langle c^\dagger_{i\uparrow} c_{i\uparrow} \rangle c^\dagger_{i\downarrow} c_{i\downarrow} + \langle c^\dagger_{i\downarrow} c_{i\downarrow} \rangle c^\dagger_{i\uparrow} c_{i\uparrow} - \langle c^\dagger_{i\uparrow} c_{i\uparrow} \rangle \langle c^\dagger_{i\downarrow} c_{i\downarrow} \rangle \\
&\qquad - \langle c^\dagger_{i\uparrow} c_{i\downarrow} \rangle c^\dagger_{i\downarrow} c_{i\uparrow} - \langle c^\dagger_{i\downarrow} c_{i\uparrow} \rangle c^\dagger_{i\uparrow} c_{i\downarrow} + \langle c^\dagger_{i\uparrow} c_{i\downarrow} \rangle \langle c^\dagger_{i\downarrow} c_{i\uparrow} \rangle \Big] && (3.41)\\
&= U \sum_i \left(-\frac{1}{2} \boldsymbol{m}_i \cdot \sum_{\alpha\beta} c^\dagger_{i\alpha} \boldsymbol{\sigma}_{\alpha\beta} c_{i\beta} \right) && (3.42)\\
&\equiv \mathcal{H}_U^{\mathrm{HF}} && (3.43)
\end{aligned}$$

where $\boldsymbol{m}_i \equiv \langle \sum_{\alpha\beta} c^\dagger_{i\alpha} \boldsymbol{\sigma}_{\alpha\beta} c_{i\beta} \rangle$ denotes the local magnetization of ith site and $\boldsymbol{\sigma} \equiv (\sigma_x, \sigma_y, \sigma_z)$ is the Pauli matrices vector. We will use a set of the local magnetizations as a mean-field. We can now construct the effective Hamiltonian, for example, the Hubbard model becomes

$$\mathcal{H} = -t \sum_{\langle ij \rangle} \left(c^\dagger_i c_j + H.c. \right) + U \sum_i \left(-\frac{1}{2} \boldsymbol{m}_i \cdot \sum_{\alpha\beta} c^\dagger_{i\alpha} \boldsymbol{\sigma}_{\alpha\beta} c_{i\beta} \right) . \qquad (3.44)$$

The number of mean-field parameters is determined by the system. It depends on the size of the unit cell, boundary conditions, and even the symmetry considerations. If we consider an unit cell composed of n-site, it has basically $4n$ mean-field parameters. Some symmetry considerations may give constraints on the parameters, and the number of parameters we have to deal with is reduced.

Because we do not know the values of mean-field parameters, diagonalizing the Hamiltonian is itself meaningless. We need to find self-consistent mean-field parameters. First, take an initial guess of the mean-field values. Insert these values to the effective Hamiltonian and solve the problem. The resulting ground state gives a new set of mean-field parameters (which here are magnetizations). We then compare the previous and the new parameters. If two sets are inconsistent, go back to the first step and iterate solving the Hamiltonian with new mean-field parameters. Otherwise, if they are consistent, it provides us a self-consistent ground state. This process is schematically represented in Fig. 3.2.

On the other hand, you can also obtain the ground state by minimizing the (free) energy functional with the mean-field. Finding its minimum energy and its solution numerically or analytically gives the ground state. The self-consistent mean-field solutions are equivalent to this method. When the number of the mean-field parameters is very large, it is more convenient and faster to calculate the iterative calculations of the mean-field.

We consider the Hubbard model in the honeycomb lattice. We employ two kinds of boundary conditions which represents the bulk system and the ribbon of a finite width. The bulk calculation is performed with a unit cell composed

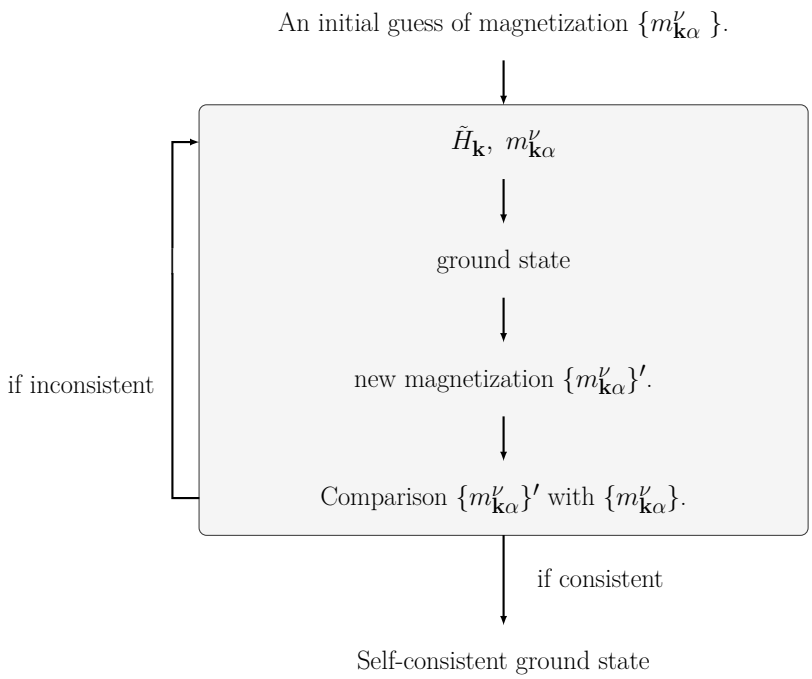

Figure 3.8: The procedure of the self-consistent loop.

of two atoms. At half-filling, the electronic number density $\langle n_i \rangle = 1$ and the additive constant energy can be neglected in the Hamiltonian. After the Fourier transformation of the creation and annihilation operators,

$$c_{i\uparrow} = \frac{1}{\sqrt{N_\Lambda}} \sum_i e^{-i\mathbf{k}\cdot\mathbf{r}_i} c_{\mathbf{k}\uparrow} \quad , \quad c^\dagger_{i\uparrow} = \frac{1}{\sqrt{N_\Lambda}} \sum_i e^{i\mathbf{k}\cdot\mathbf{r}_i} c^\dagger_{\mathbf{k}\uparrow}. \tag{3.45}$$

The Hamiltonian can then be rewritten as

$$\mathcal{H}_U^{\mathrm{HF,bulk}} = \sum_{\mathbf{k}} \Psi_{\mathbf{k}}^\dagger \tilde{H}_U^{\mathrm{HF,bulk}}(\mathbf{k}) \Psi_{\mathbf{k}} + \frac{UN_\Lambda}{4} \left(\sum_{\alpha=x,y,z} {m_{i\alpha}^A}^2 + {m_{i\alpha}^B}^2 - \langle n_i \rangle^2 \right) + \mathrm{const.} \tag{3.46}$$

where $\Psi_{\mathbf{k}}^\dagger = ({c_{\mathbf{k}\uparrow}^A}^\dagger, {c_{\mathbf{k}\uparrow}^B}^\dagger, {c_{\mathbf{k}\downarrow}^A}^\dagger, {c_{\mathbf{k}\downarrow}^B}^\dagger)$, N_Λ is the number of lattice sites, and $\tilde{H}_U^{\mathrm{HF,bulk}}(\mathbf{k})$ is a 4×4 matrix given by

$$\tilde{H}_U^{\mathrm{HF,bulk}}(\mathbf{k}) = \begin{pmatrix} \mathbf{M}_{2\times 2}^A & \\ & \mathbf{M}_{2\times 2}^B \end{pmatrix} . \tag{3.47}$$

We defined

$$\mathbf{M}^{(A/B)} \equiv \begin{pmatrix} m_{\mathbf{k}z}^{(A/B)} & m_{\mathbf{k}x}^{(A/B)} - i m_{\mathbf{k}y}^{(A/B)} \\ m_{\mathbf{k}x}^{(A/B)} + i m_{\mathbf{k}y}^{(A/B)} & m_{\mathbf{k}z}^{(A/B)} \end{pmatrix} \tag{3.48}$$

where $\sigma =$ A, B which denote the atoms in the unit cell. Combining this result with other Hamiltonian terms, we can calculate and obtain the ground state with its energy.

Since the honeycomb lattice has the bipartite structure we can expect antiferromagnetic ordering. Accordingly, we take $m_{\mathbf{k}\alpha} = m_{\mathbf{k}\alpha}^A = -m_{\mathbf{k}\alpha}^B$. It actually comes from the symmetry considerations that the system does not break the sublattice symmetry. If the system break the symmetry, we need to reconsider which the mean-field parameters are used. Also, if other Hamiltonian terms has a rotational symmetry (SU(2) for spin-1/2 particle) we can take only one component of the local magnetization, say m_z, without loss of generality. In fact, the calculation will find without these symmetry considerations, but the convergence occurs

more slowly. The KM model has only axial symmetry, so we need to consider two components, $m_{XY} = m_x = m_y$ and m_z.

The nanoribbon geometry does not have translational symmetry in one direction (sublattice symmetry breaks) and accordingly, we need to take the enlarged basis state

$$\Psi^\dagger(k) = (c^\dagger_{1A}, c^\dagger_{1B}, c^\dagger_{2A}, c^\dagger_{2B}, \ldots, c^\dagger_{LA}, c^\dagger_{LB}). \tag{3.49}$$

where k is a momentum in the direction of the ribbon length. The Hamiltonian of the system can also be extended with this basis and rewritten as a $4L \times 4L$ matrix as follows :

$$\tilde{H}_U^{\mathrm{HF,ribbon}}(k) = \begin{pmatrix} \mathbf{M}^{1A}_{2\times 2} & & & & \\ & \mathbf{M}^{1B}_{2\times 2} & & & \\ & & \ddots & & \\ & & & \mathbf{M}^{LA}_{2\times 2} & \\ & & & & \mathbf{M}^{LB}_{2\times 2} \end{pmatrix}. \tag{3.50}$$

Fortunately, the ribbon system has the reflection symmetry across the ribbon. We thus take a relation $m^{n,(A/B)}_{\mathbf{k}\alpha} = -m^{L-1-n,(A/B)}_{\mathbf{k}\alpha}$ to reduce the number of self-consistent mean-field variables.

Chapter 4

Frustrated Spin-1 Chains

In this chapter, we investigate ferromagnetically frustrated spin-1 chain systems. They are described by a combination of the antiferromagnetic and the ferromagnetic couplings between spins that has not been explored so far while another frustrated system discussed in Sec. 2.1.5 is composed of antiferromagnetic couplings only, We examine how the DH phase changes with the ferromagnetic interactions. We then show that there is no other phase between the ferromagnetic phase and the DH phase. The spin-spin correlation function and its structure factor are analyzed in the DH phase. The string order parameters and the absence of chirality are also discussed.

4.1 Model

The Hamiltonian of our model is

$$\mathcal{H} = J_1 \sum_i \hat{\boldsymbol{S}}_i \cdot \hat{\boldsymbol{S}}_{i+1} + J_2 \sum_i \hat{\boldsymbol{S}}_i \cdot \hat{\boldsymbol{S}}_{i+2} \tag{4.1}$$

where $\hat{\boldsymbol{S}}_i = (\hat{S}_i^x, \hat{S}_i^y, \hat{S}_i^z)$ is a spin-1 operator vector at i-th site. The exchange interaction strengths of nearest-neighbors (NN) and next-nearest-neighbors (NNN) are denoted by J_1 and J_2, respectively. We also denote the total number of sites in a chain N. We investigate the Hamiltonian (Eq. (4.1)) with ferromagnetic NN couplings ($J_1 < 0$) and antiferromagnetic couplings ($J_2 > 0$) at zero temperature. We adopt slightly modified open boundary conditions (Fig. 3.3(a)) in which the last two NN spins interact with J_2. This was explained in detail in Sec. 3.1.5. It leads to an effective finite-size calculation in the DH phase. We performed comparative computation in the standard open boundary conditions and found no significant qualitative difference in the bulk state. Henceforth, we will denote the energy and the length in units of J_2 and of the lattice constant, respectively.

4.2 Results

In this work, we use the DMRG method with infinite algorithm (Sec. 3) in chains up to $L = 200$. The spin-spin correlations in different sizes turn out to convolute to a single curve in a wide range of coupling parameters, as will be shown later. We estimate the uncertainty in the data by the maximum deviation from the average value for the systems with size $L \geq 50$. and mark the error bars when they are larger than the size of symbols. We have also checked out the convergence of the data with respect to m, where m is the number of states per block after truncation, by increasing m consecutively. The truncation errors in our calculations with $m = 200$ are of the order of 10^{-5} to 10^{-7} for the DH phase, in which the main interest of this work lies. They are larger in the central region of the DH phase

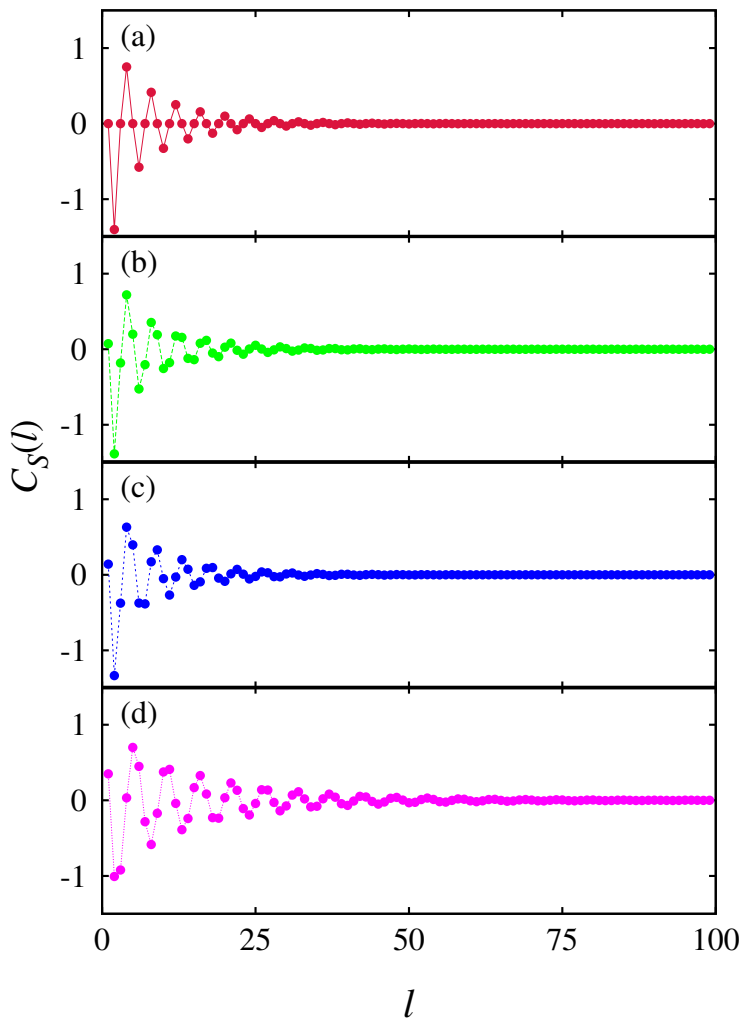

Figure 4.1: (Color online.) Spin-spin correlation functions as a function of the separation l between the spins (defined in Eq. (4.2)) for (a) $J_1 = 0$, (b) -0.5, (c) -1, and (d) -2. from top to bottom. The period of the oscillation is 4 (i.e. $k = \pi/2$) at $J_1 = 0$ and becomes incommensurate as J_1 decreases. Their amplitudes seems to decay without any long-range order.

due to the increase in frustration. In the region of the ferromagnetic phase the truncation errors decrease significantly below 10^{-15}. We have performed the calculation with m up to 250, and found that most physical results do not depend significantly on m. Some m-sensitive physical quantities such as the correlation length are presented together with the extrapolation value to $m = 1$, and relevant error bars are marked when they are larger than the size of the symbols.

We first calculate the spin-spin correlation function $C_S(l)$ which is defined as

$$C_S(l) = \langle \hat{\boldsymbol{S}}_i \cdot \hat{\boldsymbol{S}}_{i+l} \rangle \ . \tag{4.2}$$

This correlation function considers the rotational symmetry of spins which exists in the Hamiltonian of Eq. (4.1). In order to minimize finite-size effects, we take site i such that both sites i and $i+1$ are as far from the boundaries as possible.

Figure 4.1(a) shows the spin-spin correlation function for $J_1 = 0$. The ground state for $J_1 = 0$ can be simply understood in terms of the two completely decoupled chains, resulting in finite spin-spin correlations only for even-integer separations l with vanishing correlations for odd-integer separations. Within each subchain the system lies in the Haldane phase, which exhibits short-range antiferromagnetic correlations. Such spin-spin correlations are in good agreement with those plotted in Fig. 4.1(a). The correlations decay exponentially with the separation l, superposed by the oscillating correlations with a period of 4.

We also plot the spin-spin correlations for various ferromagnetic NN couplings J_1 in Fig. 4.1. When J_1 is finite, the two subchains are no longer decoupled and finite correlations show up for odd-integer separations. Interestingly, the corre-

lations still display oscillating behavior apparently with a single period, which is different from 4, the value for $J_1 = 0$; it increases monotonously with the increase of $|J_1|$. It is also of interest to note that the oscillating period does not always appear commensurate with the lattice period. Another conspicuous feature is that the decay of the correlations becomes slower as the ferromagnetic NN coupling becomes stronger. While the correlations become negligible around $l \approx 30$ for $J_1 = 0$, we can observe clear oscillations for $l \gtrsim 60$ at $J_1 = -2$. Until J_1 reaches the value $J_c \equiv -4$ the system does not show any abrupt change in the correlations, which implies that in the region of $J_c < J_1 < 0$ the system remains in the double Haldane phase. For $J_1 < J_c$, the spin-spin correlation function takes just the constant value of unity, independent of l, and the total spin of the ground state turns out to be $S_{\text{tot}} = L$, signifying that the system is in the ferromagnetic phase. The critical value in the ferromagnetic phase for $S = 1$ is the same as that in the case of classical spin systems [55] and $S = 1/2$ spin systems [117–121], as pointed out in Ref. 122.

For a quantitative analysis of the evolution of the states with J_1 varied, we examine the spin structure factor

$$S(k) \equiv \sum_l e^{ikl} C_S(l) \tag{4.3}$$

which is the Fourier transform of $C_S(l)$. We have used fast Fourier transform algorithms for $C_S(l)$ to obtain $S(k)$ and plot the resulting spin structure factor in Fig. 4.2 for various values of J_1. For $J_1 = 0$ we have broad peaks at $k = \pm 2$, which reflects oscillations with period 4. The peak broadens due to the exponentially

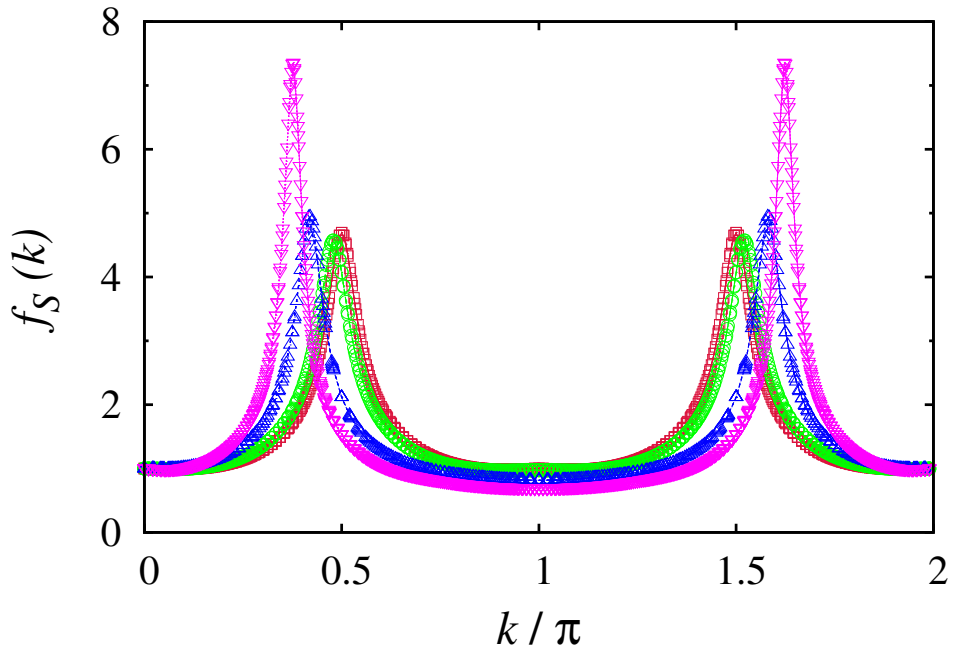

Figure 4.2: (Color online.) Spin structure factor S(k) for various NN couplings J_1. The data for $J_1 = 0$, -0.5, -1, and -2 with various lengths $L = 40$ to 100 are marked by red squares, green circles, blue triangles, and purple inverted triangles. The structure factor has two peaks in the DH phase, which are not divergent in the thermodynamic limit. This implies the spontaneous magnetization is absent. As J_1 is reduced, the peaks move closer to $k = 0$ and the system exhibits incommensurate short-ranged correlations.

decaying correlations. As $|J_1|$ increases, the positions of two peaks move towards $k = 0$. It is also clear that the peak gradually becomes narrower with the increase of J_1. This result for $S(k)$ gives quantitative support to all the observations on the spin-spin correlation function $C_S(l)$ mentioned above. The structure factor remains finite even when L is increased indefinitely, and the system does not exhibit long-range spin order in this region.

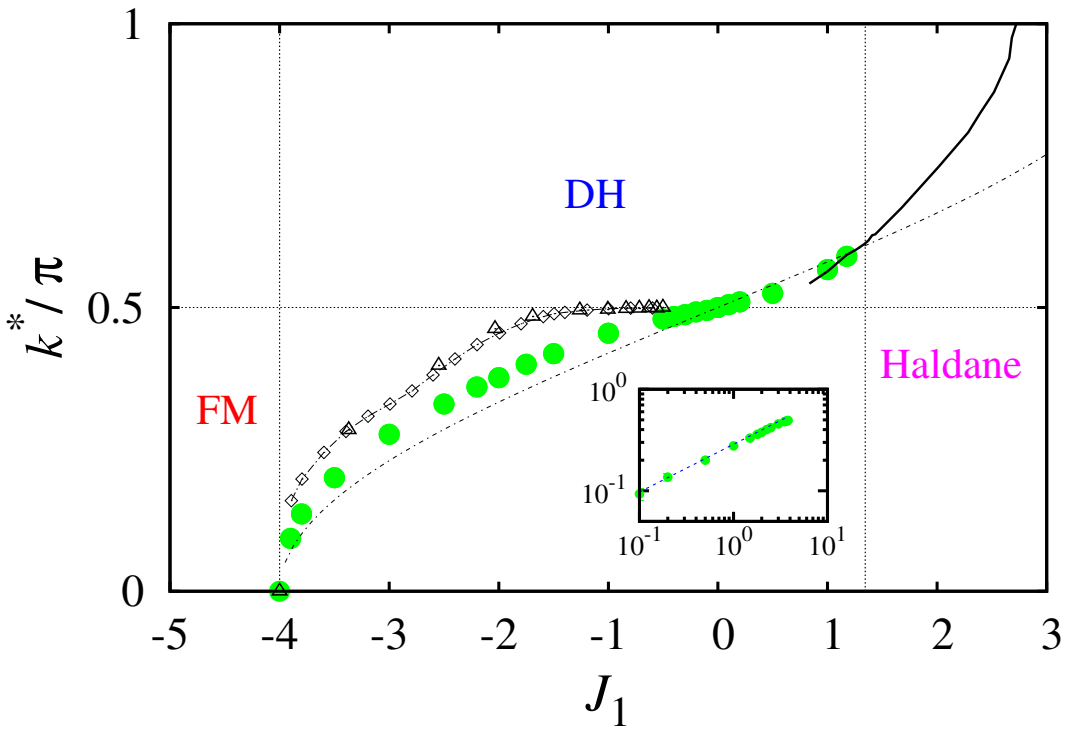

Figure 4.3: (Color online) The pitch angle k^* as a function of the NN couplings J_1. The pitch angles, which are determined by the maximum position in the structure factor, are marked by green solid circles. The pure NNN-AKLT state ($J_1 = 0$) has $k^* = \pi/2$ reflecting the short-ranged antiferromagnetic correlation in each subchain. The antiferromagnetic correlation becomes incommensurate at finite J_1 in the DH phase. We also plot the results of the classical spin system, $\arccos(-J_1/4)$ (dot-dashed line), and those of the spin-1/2 system from Ref. 120 (triangles) and Ref. 123 (diamonds) for comparison. The data marked by a solid line as well as the transition point to the Haldane phase are quoted from Ref. 62. The inset shows the pitch angle in a log-log plot for $J_1 - J_c > 0$ with $J_c = -4$ and the dashed line represents the best power-law fit to the data. The data points without error bars have errors not larger than the size of the symbols.

We can determine the pitch angle k^* of the spin correlations by the position of the maximum in $S(k)$ on the side of positive k. For $J_1 = 0$, the peak is located at $k^* = \pi/2$ which is consistent with the NNN AKLT state, the prototype state in the double Haldane phase. In Fig. 4.3 we plot k^* as a function of J_1. As $|J_1|$ increases, k^* decreases monotonously from $k^* = \pi/2$ for $J_1 = 0$ to $k^* = 0$ for $J_1 = J_c$, and the ground state connects smoothly with the FM state at $J_1 = J_c$. The decreasing curve corresponds to a convex-up function.

Such behavior is reminiscent of the spiral state which shows up in the classical spin system. In the presence of NN ferromagnetic couplings ($J_1 < 0$) and NNN antiferromagnetic couplings ($J_2 > 0$), the classical spins exhibit a spiral state for $-J_c < J_1 < J_c$, with the wave number given by $q = \arccos(-J_1/4)$ [55]. Similar behaviors of the pitch angle were also reported in previous numerical studies of the spin-1/2 chains via the transfer-matrix DMRG method [120] and the infinite time-evolving block-decimation algorithm method [123, 124]. For comparison, we have also plotted the data for classical and spin-1/2 chains with a dot-dashed line and open symbols, respectively, in Fig.4.3. In all three systems the pitch angle k^* reduces with the increase of $|J_1|$ starting from $k^* = \pi/2$ at $J_1 = 0$, and approaches $k^* = 0$ continuously at the transition into the FM phase. In the case of the spin-1/2 chains, the plateau-like region persists near $J_1 = 0$ up to $J_1 \approx -2$. On the other hand, the classical spin system displays a rather gradual decrease even near $J_1 = 0$. The curve of k^* for the spin-1 chain locates between the classical and spin-1/2 systems, which may be attributed to the reduction of quantum fluctuations in spin-1 systems in comparison with spin-1/2 systems. It would be interesting to study variations of the pitch angle for higher spins, which

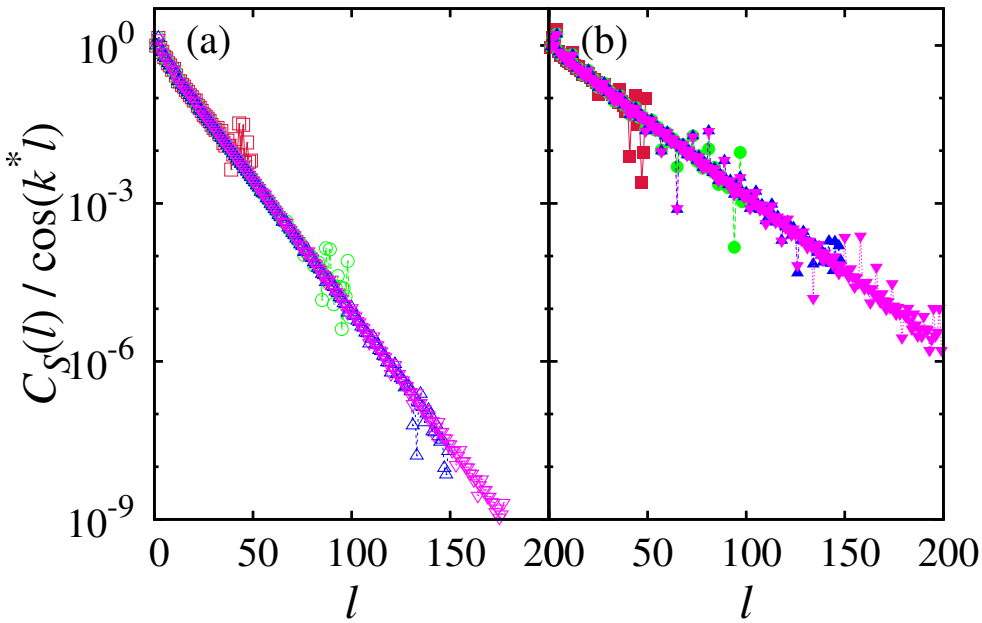

Figure 4.4: (Color online) Semi-log plot of the spin-spin correlation function $C_S(l)$ divided by $\cos(k^*l)$ for several values of L and (a) $J_1 = -1$ and (b) $J_1 = -2$. The pitch angle k^* is determined by the maximum position of the structure factor for each J_1. The data denoted by red squares, green circles, blue triangles, and pink inverted triangles correspond to $L = 50, 100, 150$, and 200, respectively.

should reflect the effects of both the changes in quantum fluctuations and the alternating behavior of integer and half-integer spins.

In the inset of Fig. 4.3, we plot k^* as a function of $J_1 - J_c$ in the log-log scale. Near the critical point the pitch angle displays the power-law behavior

$$k^* \sim (J_1 - J_c)^\alpha \tag{4.4}$$

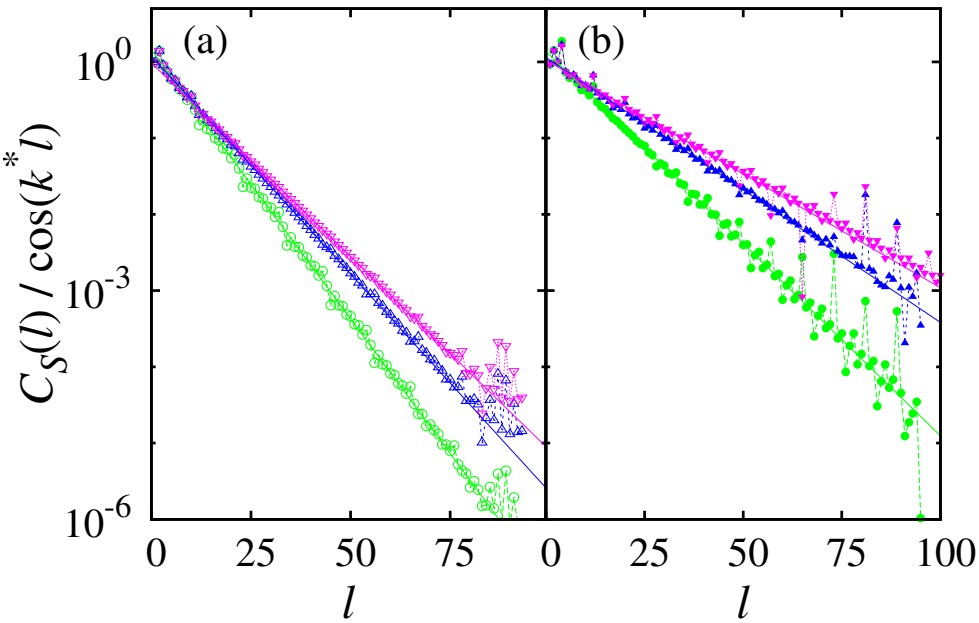

Figure 4.5: (Color online.) Semi-log plot of the spin-spin correlation function $C_S(l)$ divided by $\cos(k^*x)$ for several values of m and (a) $J_1 = -1$ and (b) $J_1 = -2$. The pitch angle k^* is determined in the same way as in Fig. 4.4. The data denoted by green circles, blue triangles, and pink inverted triangles correspond to $m = 50, 100$, and 150, respectively, and the solid lines are the best linear fits.

The best fit in the range $-3.9 \leq J_1 \leq -3.0$ gives the exponent $\alpha = 0.47(3)$. Although the best-fit value of α is a bit smaller than $\alpha_{\rm cl} = 0.5$ for the classical spiral state, the two values are consistent within numerical errors. Numerical errors in the exponent are mainly due to the large relative errors near J_c. It is also notable that the curve of k^* versus $J_1 - J_c$ is slightly convex up in the log-log plot, which tends to give an additional underestimate of α in the power-law fit over a finite window of J_1.

In Fig. 4.3 we also plot the pitch angle in the case of $J_1 > 0$: The solid line represents the data from an earlier study [62] for $S = 1$, and the data points denoted by solid circles are obtained from our calculation. The double Haldane phase in this region gives pitch angles in the range $\pi/2 < k^* < \pi$ [61, 62]. The pitch angle increases with J_1 and becomes commensurate with $k^* = \pi$ around $J_1 \approx 2.67$. Remarkably, the incommensurate spin correlations persist even in the region of the Haldane phase, which sets in at $J_1 \approx 1.34$. This is in contrast to the fact that the pitch angle reduces to $k^* = 0$ exactly at the transition to the FM phase for $J_1 < 0$.

In order to examine the correlation length, we divide the spin correlation function $C_S(l)$ by the oscillating factor $\cos(k^* l)$ and estimate the correlation length ξ by fitting it to the exponential decay $\sim \exp -l/\xi$. In Figs. 4.4 and 4.5 one can see that $C_S(l)/\cos(k^* l)$ for $J = -1$ and -2 decays exponentially in a wide range of l. Figure 4.4 also demonstrates that the quantities in different sizes exhibit almost the same exponentially-decaying behavior except for near the edges. The decay tends to become slower as the number m of the kept states is increased. In Fig. 4.6 we plot the correlation length ξ estimated from the best fit as a function of J_1 for various values of m as well as in the limit $m \to \infty$. We have also reproduced the data for $J_1 > 0$ from an earlier work [61]. For $J_1 > 0$ our numerical results are consistent with the peak associated with the transition between the Haldane and the DH phases. For $J_1 < 0$ the correlation length is enhanced as J_1 approaches J_c. We also note that there exists a small bump around $J_1 = 0$, which signifies stronger spin fluctuations near the decoupled subchains.

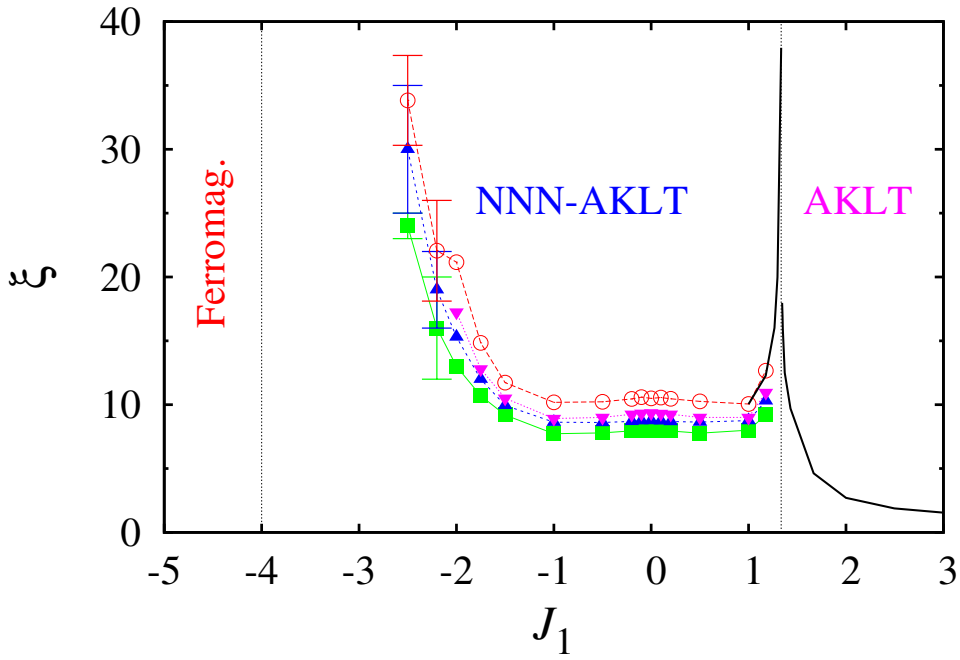

Figure 4.6: Correlation length as a function of the NN coupling J_1 for m =100 (green squares), 150 (blue triangles), 200 (pink inverted triangles), and its extrapolation to $m = \infty$ [(red) circles]. As we approach the phase boundary to the ferromagnetic phase the correlation length becomes very large and is expected to diverge at $J = -4$. Solid lines denote the data quoted from Ref. 61. The data points without error bars have errors not larger than the size of the symbols.

We also examine string order and double-string order for $J_1 < 0$, which can be probed by the use of the following nonlocal correlators [11–13, 60]

$$O_1(l, l') \equiv -\langle S_l^z \left[\exp\left(\sum_{j=l+1}^{l'-1} i\pi S_j^z \right)] \right] S_{l'}^z \rangle \tag{4.5}$$

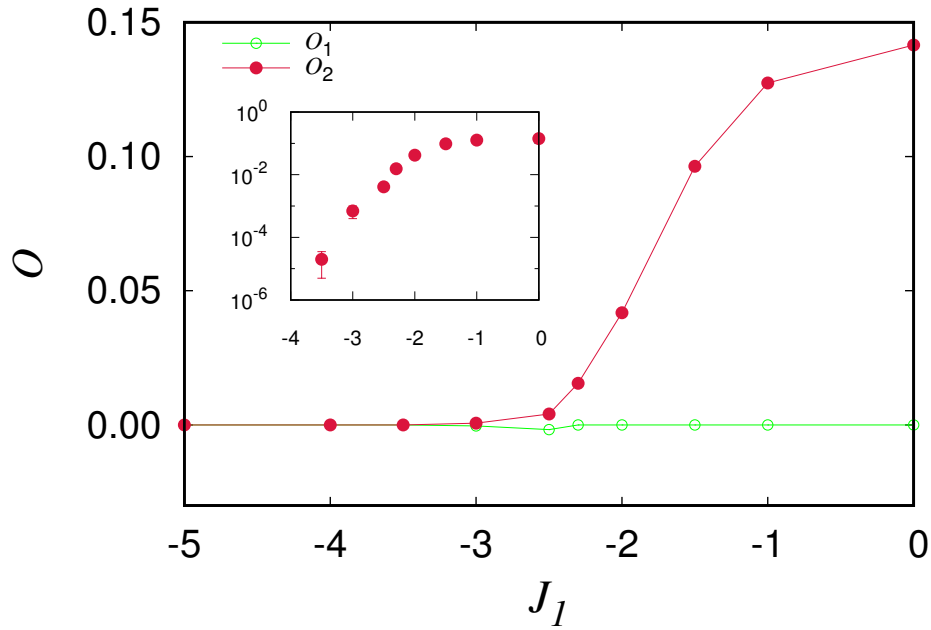

Figure 4.7: (Color online) String order parameters as a function of the NN coupling J_1. We represent O_1 and O_2 by red solid circles and green empty circles, respectively. The inset displays the semi-log plot of O_2. The data points without error bars have errors not larger than the size of the symbols.

and

$$O_2(l,l') \equiv \langle S_l^z S_{l+1}^z \left[\exp\left(\sum_{j=l+2}^{l'-2} i\pi S_j^z \right)] \right] S_{l'-1}^z S_{l'}^z \rangle \ . \tag{4.6}$$

The string order parameters O_1 and O_2 can then be defined by

$$O_1 \equiv \lim_{|l-l'|\to\infty} O_1(l,l') \tag{4.7}$$

$$O_2 \equiv \lim_{|l-l'|\to\infty} O_2(l,l') \tag{4.8}$$

in the limit of infinite separations. Figure 4.7 shows string order parameters O_1 and O_2 versus J_1. For $J_1 = 0$, we have nonzero O_2 with vanishing O_1, which is a typical characteristic of the DH phase. On the other hand, in the FM phase ($J_1 < J_c$) both O_1 and O_2 vanish. As J_1 decreases from zero, O_2 also reduces. It reflects that the singlet bonds on the double chain which we consider here is not captured by the single string order. The double string order becomes finite in the perturbed NNN-AKLT state, capturing the connectivity of two intertwined AKLT states [60]. We have to examine carefully the string order because it cannot distinguish the AKLT state from the magnetically ordered states [78].

It is remarkable that O_2 is significantly reduced for $J_1 \lesssim -2$, while the transition into the ferromagnetic phase occurs at $J_1 = -4$. Such an abrupt reduction may suggest the possible existence of an emergent phase between the double Haldane phase and the ferromagnetic phase. However, a detailed analysis has revealed that the string nonlocal correlator $O_2(l, l')$ shows quite distinct behavior for $-4 < J_1 \lesssim -2$ from that of the ferromagnetic phase where the string order is absent. In the ferromagnetic phase ($J_1 < J_c$) $O_2(l, l')$ shows a clear exponential decay with $|l - l'|$, implying that the corresponding string order parameter O_2 vanishes in the thermodynamic limit. For $-4 < J_1 \lesssim -2$, in contrast, $O_2(l, l')$ remains finite although its values are very small. The semi-log plot of O_2, which is presented in the inset of Fig. 4.7, also supports a direct transition from the double Haldane phase to a ferromagnetic one. It demonstrates that the decreasing behavior is rather consistent with the transition at $J_1 = -4$ although a rapid decrease of O_2 starts around $J_1 \approx -2$.

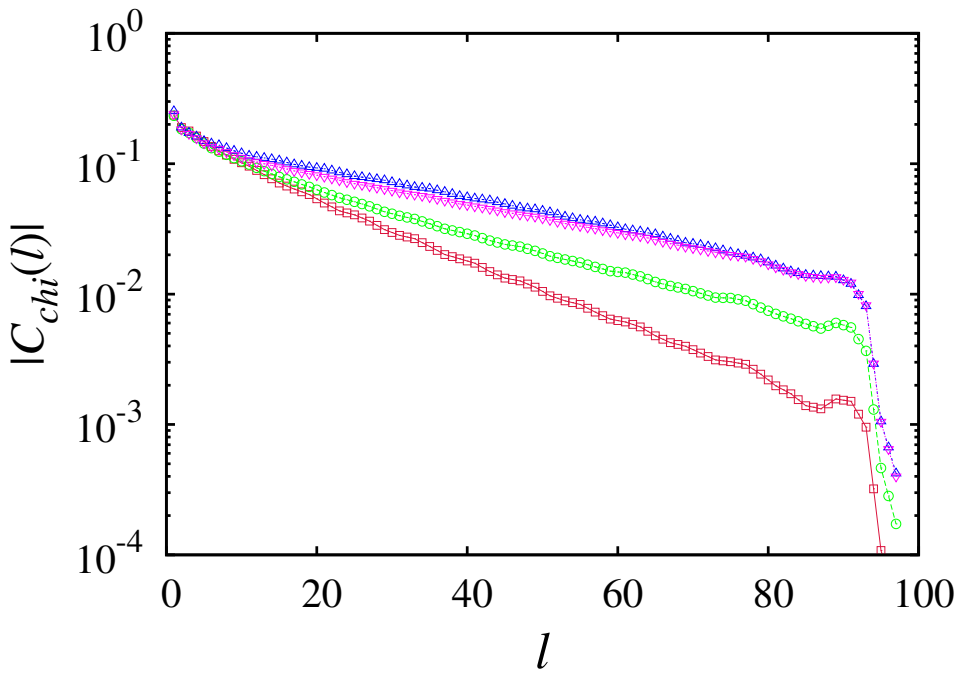

Figure 4.8: (Color online) Semi-log plot of the chirality correlation function $C_\kappa(l)$ for $J_1 = -3$. The data denoted by red squares, green circles, blue triangles, and pink inverted triangles correspond to $m = 50, 100, 150$, and 200, respectively.

It is also worth while to examine whether a chiral phase is present between the double Haldane phase and the ferromagnetic phase. In the spin-1/2 case the chiral phase has been reported in close vicinity to the region [123, 124], and accordingly, it is a strong candidate for a new phase if it emerges also in the spin-1 case. We have thus computed the chirality correlation function defined by

$$C_\kappa(l) \equiv \langle \hat{\kappa}_i^z \hat{\kappa}_{i+l}^z \rangle \tag{4.9}$$

with

$$\hat{\kappa}_i^z \equiv \hat{z} \cdot (\hat{\boldsymbol{S}}_i \times \hat{\boldsymbol{S}}_{i+1}) = \hat{S}_i^x \hat{S}_{i+1}^y - \hat{S}_i^y \hat{S}_{i+1}^x. \tag{4.10}$$

Figure 4.8 presents $C_\kappa(l)$ for $J_1 = -3$, where O_2 is significantly reduced. The chirality correlation function exhibits an apparent exponential decrease, which indicates the absence of a chiral phase. This also implies that the emergence of a new phase is less probable. We presume that the great reduction in O_2 for $-4 < J_1 < -2$ is caused by the large ferromagnetic fluctuations which are enhanced markedly in that region, as can be seen in Fig. 4.6.

4.3 Summary

We have investigated the one-dimensional spin-1 system frustrated by the combination of the spin exchange interactions: the ferromagnetic one between NN spins and the antiferromagnetic one between NNN spins. Via the DMRG calculations we have confirmed explicitly that the ferromagnetic phase transition for $S = 1$ occurs at $J_1 = -4(\equiv J_c)$ [122, 125], below which the spin-spin correlation function becomes constant. The robustness of J_c suggests that quantum fluctuations due to the quantum nature of the spin do not affect significantly the ferromagnetic phase transition; this is in sharp contrast to the fact that other phase boundaries of the frustrated spin chains exhibit strong dependence on S and a variety of distinct phases [126]. Such interesting results may be tested through experiments on ultracold atoms [127–129].

In the double Haldane phase, on the other hand, the system shows short-ranged antiferromagnetic spin-spin correlations. Such behavior remains robust in a wide range of the NN ferromagnetic interaction strength J_1 up to J_c. The pitch angle of the incommensurate spin-spin correlations decreases from $\pi/2$ as

J_1 approaches J_c, vanishing at $J_1 = J_c$. Similar behaviors were also reported in earlier works on the classical and spin-1/2 systems. It has been revealed that the results of the spin-1 system are closer to the classical results than those of the spin-1/2 one. We have also discussed the behavior of string order parameters in the double Haldane phase in the presence of ferromagnetic NN couplings. It has been found that the string order parameter O_2 undergoes a substantial reduction far above J_c. However, detailed analysis has suggested that a new phase is less likely to emerge in that region. It is presumed that the enhancement in the ferromagnetic fluctuations gives rise to such substantial reduction in O_2.

Chapter 5

Anisotropy in spin chains

It has been known that systems with anisotropic interactions can have a lot of phases such as the Ising FM, the Ising antiferromagnet or the XY (critical) phases as we reviewed in Sec. 2.1.6. In a combination of the frustration and the anisotropy, while it is shown that the spin-1/2 chains display chirality or other more phases, a complete understanding of the combination of ferromagnetic frustration and anisotropy is still lacking in the spin-1 chain In this chapter, we examine the effects of the anisotropic exchange interaction on the frustrated Heisenberg spin chain. Various correlation functions are calculated and we obtain a full phase diagram. In contrast to the isotropic frustrated model in Sec. 4 we found various phases, continuous/discontinuous phase transitions between them, and even a new intermediate phase with the nonzero string order parameter appearing in a wide region.

5.1 Model

The Hamiltonian of the spin-1 chain with anisotropic exchange interaction and frustration is

$$\begin{aligned}\mathcal{H} = \quad & J_1 \sum_i \left(S_i^x S_{i+1}^x + S_i^y S_{i+1}^y + J_z S_i^z S_{i+1}^z \right) \\ & + J_2 \sum_i \left(S_i^x S_{i+2}^x + S_i^y S_{i+2}^y + J_z S_i^z S_{i+2}^z \right) \ , \end{aligned} \tag{5.1}$$

where S_i^σ $(\alpha = x, y, z)$ denotes a spin-1 operator at site i. We take the ferromagnetic NN interaction $(J_1 < 0)$ and the antiferromagnetic NNN interaction $(J_2 > 0)$, which results in frustration of the system. The strength of the anisotropic exchange interaction is denoted by J_z and is taken for $0 \leq J_z < 1$. We will also denote the energy and the length in units of J_2 and of the lattice constant, respectively, throughout this work.

5.2 Results

We perform the DMRG calculation for various values of J_z and J_1 to investigate how ground state of the system changes as the anisotropic interaction varies. We also adopt and compare the two kinds of open boundary conditions - the standard and the modified ones as discussed in Sec. 3.1.5 (see Fig. 3.3). The comparative computation also shows no significant qualitative difference in the bulk state just as we introduced only the frustration, not anisotropy.

In this work, we keep m in the range between 50 and 100 in chains up to $L = 200$. The truncation errors are of the order of magnitude 10^{-5} to 10^{-8}.

For maximum values of m, the highest error corresponds to the DH phase while the XY phase and the other ordered phases have the order of 10^{-7} and 10^{-8}, respectively.

We use the following spin-spin correlation functions

$$C_\alpha(l) \equiv \langle S_i^\alpha S_{i+l}^\alpha \rangle \qquad (\alpha = x, z) \tag{5.2}$$

and the chirality correlation $C_\kappa(l)$ which was defined in Eq. (4.9) and Eq. (4.10). The spin-spin correlation functions along the x- and z-directions should be considered because the system is no longer isotropic. Similarly, we also introduce two kinds of string correlators along the x- and z-directions. as follows :

$$C_{\mathrm{str},1}^\alpha(i,j) = -\langle S_i^\alpha \left[\exp(\sum_{k=i+1}^{j-1} S_k^\alpha) \right] S_j^\alpha \rangle \tag{5.3}$$

and

$$C_{\mathrm{str},2}^\alpha(i,j) = \langle S_i^\alpha S_{i+1}^\alpha \left[\exp(\sum_{k=i+2}^{j-2} S_k^\alpha) \right] S_{j-1}^\alpha S_j^\alpha \rangle \tag{5.4}$$

where $\alpha = x$ and z. We take the site i such that both the sites i and $i+l$ are as far from the boundaries as possible in order to minimize the finite-size effects. The two string order parameters is defined as

$$O_1^\alpha \equiv \lim_{l\to\infty} C_{\mathrm{str},1}^\alpha(l) \tag{5.5}$$

$$O_2^\alpha \equiv \lim_{l\to\infty} C_{\mathrm{str},2}^\alpha(l) \tag{5.6}$$

where we divide it by $(-1)^l$ factor for the intermediate phase. They help us to

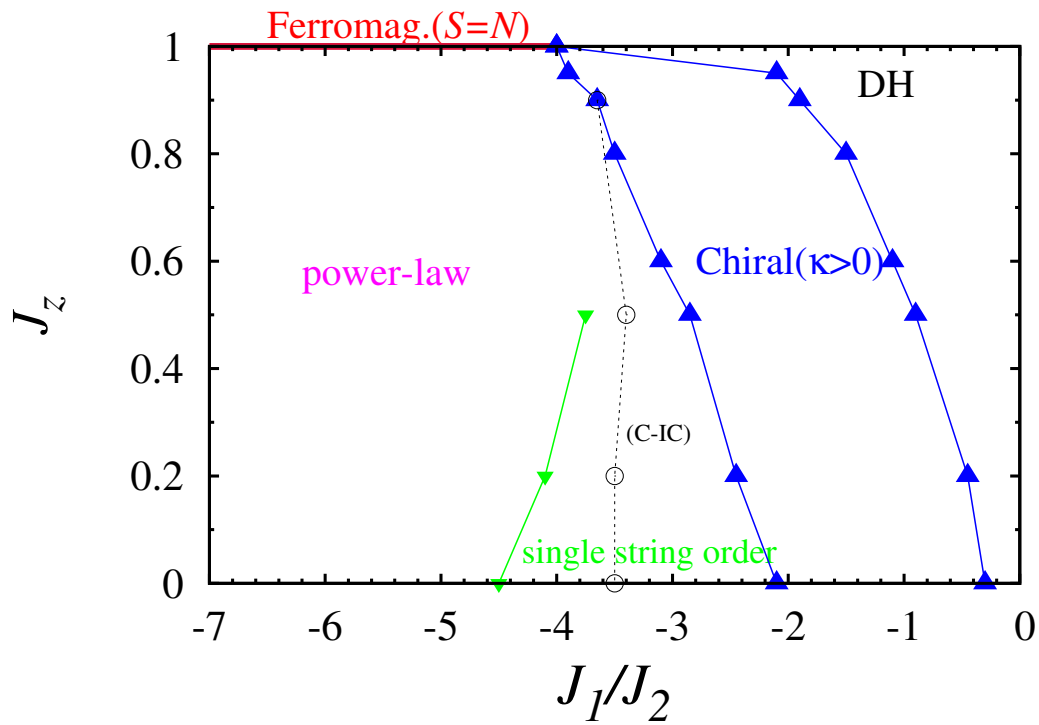

Figure 5.1: (Color online.) Phase diagram on the J_1-J_z plane. There are three additional phases in comparison with the case of $J_z = 1$ - chiral phase, ferromagnetic XY phase, and single string phase.

check whether the hidden $Z_2 \times Z_2$ symmetry is broken or not.

Figure 5.1 shows a phase diagram in the J_1-J_z plane. We obtain four distinct phases - the double Haldane (DH) phase, the chiral phase, the single string phase, and the ferromagnetic-XY phase - for $0 < J_z < 1$. The areas of these phases are determined by whether they show long-range orders, exponential decays, or power-law decays from the correlation functions.

The DH phase from the noninteracting limit still remains in wide range of J_1

even if the anisotropic interaction is introduced ($0 < J_z < 1$). There is still no qualitatively significant difference in the properties of the DH phase from those from in the previous chapter (Sec. 2.1.5). The anisotropic interaction affects the value of the Haldane gap and double string order parameters. The Haldane gap decreases monotonically as the value of J_z decreases. There exists a difference between the double string order parameters along the z- and the x- directions although they still have finite values. While the string order parameters along the z-direction decreases monotonically and rapidly as J_z decreases, the x-direction's shows a convex-up shape and larger values than that of the z-direction [68]. In addition, the ground state no longer shows nonzero values of S_tot in this region. Nevertheless, there is no magnetic order in the system, and the DH phase which is similar to the NNN-AKLT state still remains. If J_z is close enough to zero, the system undergoes a phase transition to the antiferromagnetic XY phase where the correlation functions change to the power-law distribution. Its correlation length increases greatly and continuously, and the gap is expected to vanish by the diverging correlation length in this phase though we did not show it by the calculation.

We analyzed how the system changes for fixed J_z values smaller than 1 as decreasing J_1 from 0. It is found that the double string order reduces as J_1 decreases in the DH phase. In addition, the chirality correlation starts to be enhanced gradually and become constant with diverging its correlation length at certain values. We plot the chirality correlation functions for fixed $J_z = 0.2$ in Fig. 5.3. The values of J_{c_1} are larger than the ferromagnetic phase transition

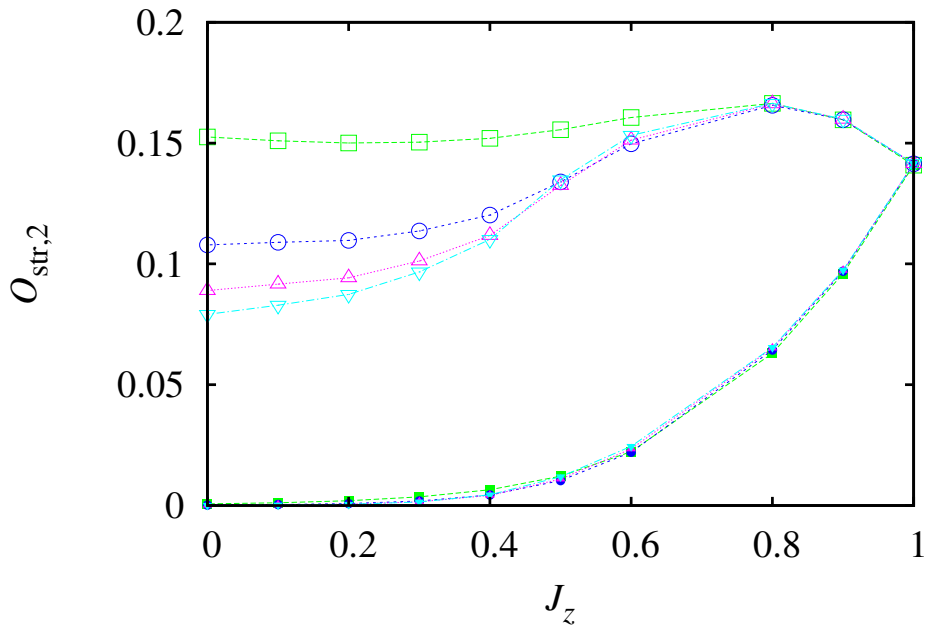

Figure 5.2: (Color online.) Double string order parameters as a function of J_z for $J_1 = 0$ and $m = 85$ from various system-size. The order parameter along the z- and x-directions are denoted by filled and open symbols, respectively, with $L = 40$ (squares), 80 (circles), 120 (triangles), 160 (inverse triangles). There exists a monotonic decrease in the z-direction's, but not in the x-direction's. The value for the x-direction around $J_z = 0$ is finite but shows the power-law behavior, vanishing in the thermodynamic limit.

point $J_c = -4$ for $J_z = 1$ which is obtained in the isotropic model in Sec. 4. It shows that for sufficiently large values of J_1 ($J_1 < J_{c_1}$) the system attains the chirality long-range order with the breaking of Z_2 symmetry. We also plot the chirality κ for various lengths defined as $\kappa \equiv \sqrt{C_\kappa(l)}$ for $l = N/2$ from Eq. (4.9) in Fig. 5.4. We find that the chirality shows up continuously and increases very rapidly after the double Haldane phase disappears. From this point, we determine

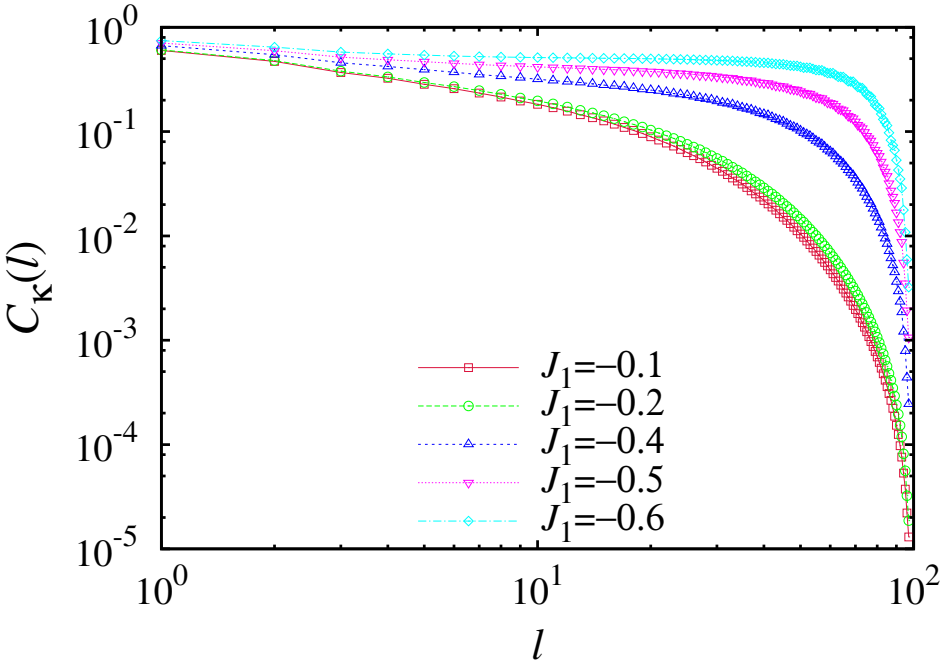

Figure 5.3: (Color online.) Log-Log plot of the chirality correlation function $C_\kappa(l)$ for $m = 100$ and various values of J_1 at $J_z = 0.2$. The data is plotted for $J_1 = -0.1$ (squares), -0.2 (circles), -0.4 (triangles), -0.5 (inverted triangles), and -0.6 (diamonds). The correlation is strongly enhanced as J_1 decreases until it becomes J_{c_1}. A rapid decrease of correlation at large distance is attributed to the finite size effect and is neglected as we increase the system-size.

the phase boundary between the chiral phase and the double Haldane phase as in Fig. 5.1. It is interesting to note that although the critical point at which the chiral order begins to occur becomes larger as J_z decreases, the width of the region of finite chirality seems to be unchanged for fixed J_z. This aspect differs markedly from the result of the spin-1/2 frustrated systems in the previous studies where the chirality phase mainly has a large chirality around $J_z \approx 0.7$ [123, 124]. The spin-1/2 results also shows a narrow region of the chiral phase for strong

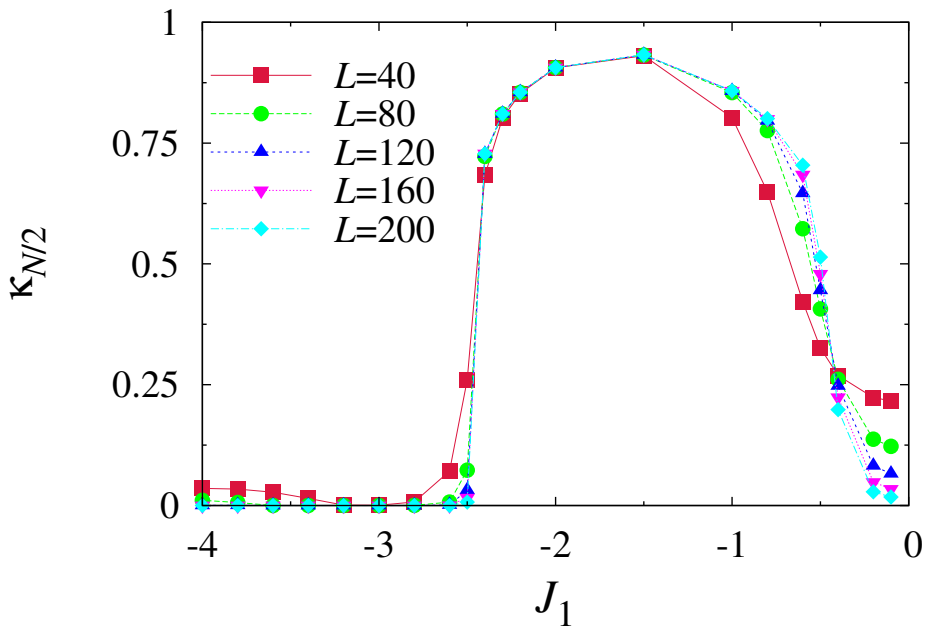

Figure 5.4: (Color online.) Chirality order parameter at $J_z = 0$ as a function of J_1 for various lengths The chirality appears for $-2.5 < J_1 < -0.5$. As we decrease J_1 the system undergoes the discontinuous phase transition to the single string phase. The chirality is reduced for $J < J_{c_2}$, resulting in the exponential decay.

anisotropy ($J_z \lesssim 0.5$). We also confirmed that the spin-spin correlation functions are decaying exponentially in the chiral phase. This fact implies that the system has a gap and is different from the gapless chiral phase [78] which shows a power-law decaying spin-spin correlation.

When the ferromagnetic NN coupling is further increased in the chiral phase, it induces two distinct phase transitions depending on the value of J_z. First, for weak anisotropy of $J_z > 0.8$ the system undergoes the phase transition to the

critical phase from the chiral phase. This critical phase is kind of the ferromagnetic XY phase where the correlation functions show the power-law distribution with divergent correlation length.

On the other hand, for sufficiently large anisotropy ($J_z \lesssim 0.5$), there is an intermediate phase between the chiral phase and the ferromagnetic XY phase. The chirality decreases and disappears when J_z becomes J_{c_2}, and then the long range order of the single string correlator appears in the system immediately. This new intermediate phase for $J_z < J_{c_2}$ shows that all the spin-spin correlation functions decay exponentially as well as the double string correlator does. We call this phase the "single string" phase which has a difference from the ordinary string (AKLT) state. The single string correlators at the intermediate phase for $J_1 = -3$ and $J_z = 0.2$ is plotted in Fig. 5.5. It is very interesting not only that the string correlations are enhanced by the ferromagnetic couplings, but also that the single string correlator along the x-direction clearly oscillates with period of 2. The oscillation of the string correlator defined in Eq. (5.4) can usually be shown in the ferromagnetic order phase. This indicates that the intermediate single string phase reflects the ferromagnetic nature of the spin state without any ferromagnetic order. We can also see that a difference between the amplitudes of the x- and z-directions is kept.

The single string order parameters for $J_z = 0.2$ are plotted together with the pitch angle from the spin-spin correlation function (Eq. 4.3) and the chirality as a function of J_1 in Fig. 5.6. The finite amplitudes of the string order parameters survives in a wide range of J_1. Meanwhile, the previous research proved that the

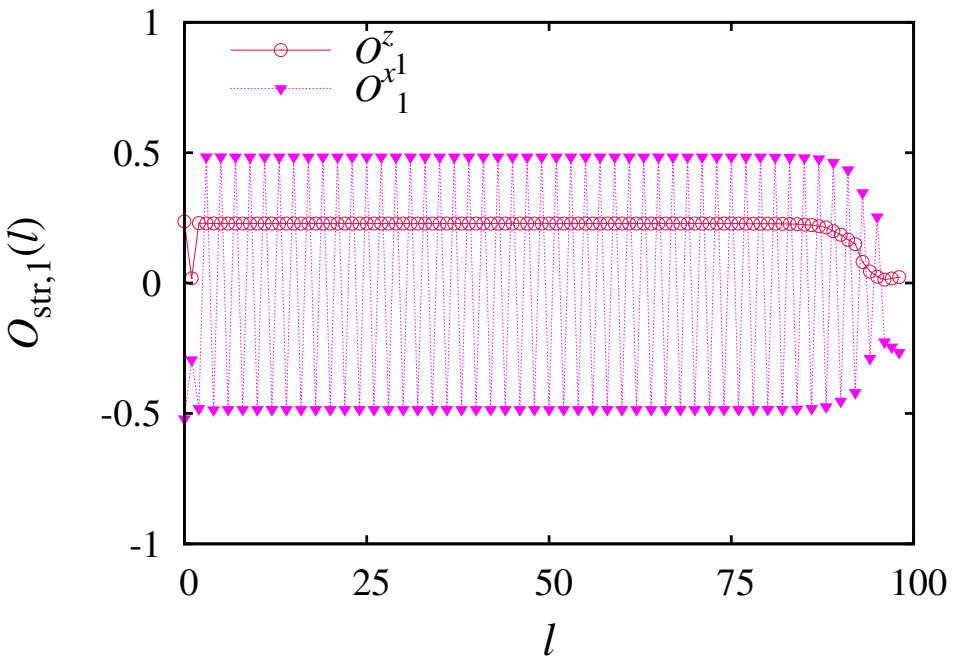

Figure 5.5: (Color online.) Single string correlators in the intermediate phase between the chiral and ferromagnetic-XY phases for $J_1 = -3$ and $J_z = 0.2$. The data for the z- and x-directions is marked by (red) circles and (purple) triangles, respectively. Both correlator remain finite as L increases, but the correlator for the x-direction oscillates with the period of 2.

Haldane phase can be understood in terms of soliton in the AKLT state [60]. They showed a solitonic excitation appears with frustration and change the sign of the string correlator when a soliton gets inside the string correlator. From this point of view, the single string phase can be described by a soliton-condensate state where the string correlation function oscillates with its separation. In a way of explaining the AKLT state by the matrix product state (MPS) [6, 7], we also try to explain this intermediate state by the MPS with different symmetry, which will be discussed in the next section. We find the qualitatively similar behavior

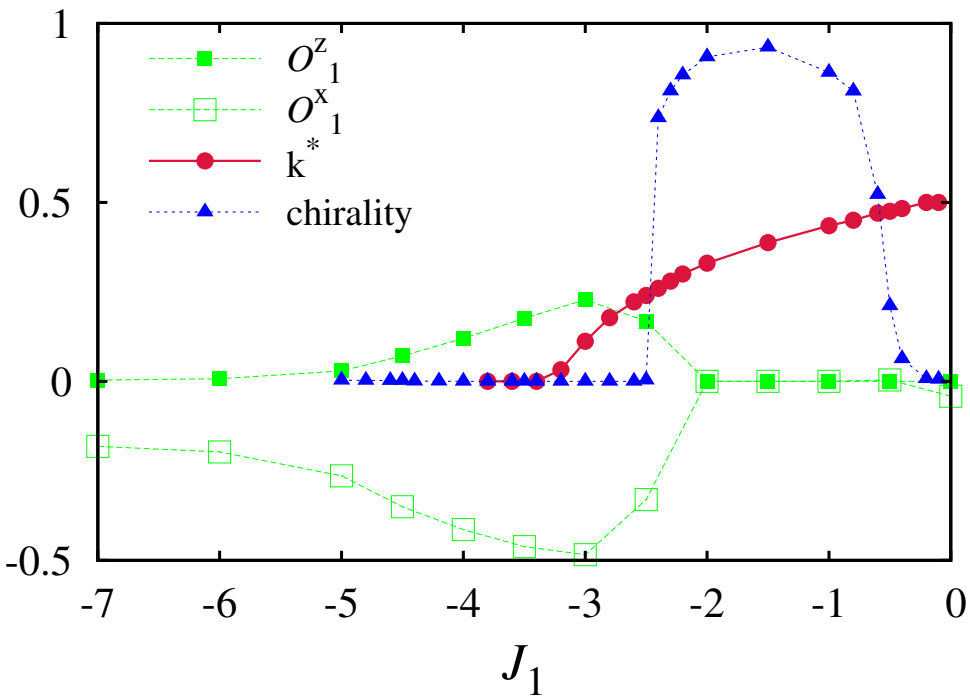

Figure 5.6: (Color online.) Single string orders, chirality, and pitch angle as a function of J_1 for $J_z = 0.2$. The string order parameters for the z- and x-directions, the chirality, and the pitch angle from the spin-spin correlation function are marked by (green) filled squares, (green) open squares, (red) filled circles, and (blue) triangles, respectively.

in our MPS state and call this resulting MPS state the "triplet-AKLT" state.

When we decreases J_1 smaller from the intermediate phase, there is another phase transition to the ferromagnetic-XY phase. All the correlation functions starts to increase their correlation length and shows a power-law decay consequently, signifying the BKT transition. This phase is adiabatically connected to that of the ferromagnetic XY model. It is also expected that its gap vanishes as

the correlation length increases

Matrix Product States

In this section, in order to explain the new single string phase which comes from the ferromagnetic interaction in our numerical result we introduce a new matrix product state (MPS). The previous research gives the AKLT state as a MPS state which describes the singlet bonds of spin-1/2 sites with the projection into the spin-1 state on a chain [6, 7] as we explained in Sec. 2.1.1. This gives a good explanation of the ground state in the spin-1 Heisenberg chain model and the gap which Haldane conjectured. The AKLT state can be captured by the string correlator describing the connectivities between the sites without magnetic order. We take a variation in the AKLT state and change the singlet bonds to the triplet bonds between the spin-1/2 sites which can be expected to have a ferromagnetic correlation. We first set and parametrize the triplet state between the $s = 1/2$ spins on different sites as follows

$$|\varphi_{i,i+1}\rangle = \quad \left(|\uparrow_i^R\rangle |\downarrow_i^R\rangle\right) \begin{pmatrix} \alpha & \frac{\beta}{\sqrt{2}} \\ \frac{\beta}{\sqrt{2}} & \gamma \end{pmatrix} \begin{pmatrix} |\uparrow_{i+1}^L\rangle \\ |\downarrow_{i+1}^L\rangle \end{pmatrix} \tag{5.7}$$

where $|\alpha|^2 + |\beta|^2 + |\gamma|^2 = 1$ and $\{|\uparrow_i^{R(L)}\rangle |\downarrow_i^{R(L)}\rangle\}$ are the spin-1/2 states on the right (left) side at ith site. Following the construction of the matrix product state in a chain, we obtain the wavefunction of the triplet-bonds of spins as

$$|\psi_{\mathrm{MPS}}\rangle = \sum_{\sigma} \mathrm{Tr}[C^{\sigma_1} C^{\sigma_2} \cdots C^{\sigma_L}]|\sigma\rangle \tag{5.8}$$

where $|\sigma\rangle = |\sigma_1\rangle|\sigma_2\rangle\cdots|\sigma_L\rangle$ and C^{σ_i} is given by

$$C^+ = \begin{pmatrix} \alpha & \frac{\beta}{\sqrt{2}} \\ 0 & 0 \end{pmatrix},\ C^0 = \begin{pmatrix} \frac{\beta}{2} & \frac{\gamma}{\sqrt{2}} \\ \frac{\alpha}{\sqrt{2}} & \frac{\beta}{2} \end{pmatrix},\ C^- = \begin{pmatrix} 0 & 0 \\ \frac{\beta}{\sqrt{2}} & \gamma \end{pmatrix}.$$

We simplify the MPS state of Eq. (5.8) into two cases satisfying the time-reversal symmetry : (a) $\beta \neq 0$, $\alpha = \gamma = 0$, (b) $\beta = 0$, $\alpha \neq 0$, $\gamma \neq 0$. In case (b), we additionally take (b1) $\alpha = \gamma$ and (b2) $\alpha = -\gamma$ separately. The most general case can presumably be obtained and explained by the superposition of the above states. To compare the physical properties of them with our numerical results, we calculate the spin-spin correlation functions and the string correlators of each MPS. The detailed calculation method is the same as explained in Sec. 2.1.4. The result is shown in Table. 5.1. While the singlet MPS (or the AKLT state) shows a positive constant of the string correlators at infinite distance l, the triplet MPS shows an alternating the sign of the string correlators with same constant. It gives a remarkably good agreement with the intermediate phase of our numerical result. The well-known antiferromagnetic spin-spin correlation is reproduced in the singlet MPS for all directions. The triplet MPS shows that one of the spin-spin correlations has an ferromagnetic correlation without oscillating correlation functions. In our numerical result, the spin-spin correlation functions show both the ferromagnetic and antiferromagnetic correlations in the intermediate phase, depending on the direction. This difference may be attributed to the composition of the triplet states, that is a linear combination of the triplet MPSs. For more quantitative comparison of their physical properties, we need to consider excitations such as the soliton excitations or magnon excitations and set an effective

Table 5.1: Single string correlator and the spin-spin correlation functions with the bond-types of the MPS as $l \to \infty$ in the thermodynamic limit

	$O^z_{str,1}$	$O^x_{str,1}$	C_z	C_x
singlet	$\frac{4}{9}$	$\frac{4}{9}$	$\sim (-\frac{1}{3})^l$	$\sim (-\frac{1}{3})^l$
triplet (a)	$\frac{4}{9}$	$\frac{4}{9}(-1)^{l-1}$	$\sim (-\frac{1}{3})^l$	$\sim (\frac{1}{3})^l$
triplet (b1)	$\frac{4}{9}(-1)^{l-1}$	$\frac{4}{9}(-1)^{l-1}$	$\sim (\frac{1}{3})^l$	$\sim (\frac{1}{3})^l$
triplet (b2)	$\frac{4}{9}(-1)^{l-1}$	$\frac{4}{9}$	$\sim (\frac{1}{3})^l$	$\sim (-\frac{1}{3})^l$

model of solitons [60]. It will helps us to understand about our numerical results, the triplet-AKLT state, and their connection.

5.3 Summary

We have investigated the spin-1 chain of anisotropic exchange interactions with frustration from the ferromagnetic and antiferromagnetic couplings by the DMRG method. We have obtained the phase diagram on the J_1-J_z plane through the analysis of the various correlation functions. There is the chiral phase in a wide region when anisotropy is introduced as well as the double Haldane phase remains. Besides, the new intermediate phase, so-called the triplet-AKLT state, emerges between the ferromagnetic XY and the chiral phase, showing the oscillating string order parameter. We have suggested that the triplet-AKLT state can be understood by the MPS where the triplet bonds are formed rather than the singlet bonds of the ordinary AKLT state. It gives a good agreement with

the oscillating string order in the x-direction. For a clearer comparison, we need to consider more quantitative analysis of energy, gaps, excitations, etc.

Chapter 6

Kane-Mele-Hubbard model

In this chapter, we study the interplay of the spin-orbit interactions and the electron-electron interactions on the honeycomb lattice. The edge state in the honeycomb lattice has the magnetization by the electron-electron interactions in the bulk while the spin-orbit interactions make the edge topologically nontrivial for finite size. We focus on large nanoribbon geometry in the Kane-Mele-Hubbard model. Magnetic properties of the system and its phase diagram are obtained in the thermodynamic limit by using a mean-field approach. The decay of the numerical magnetization from the edge to center is characterized in each phase and shows critical behavior in phase boundary.

6.1 Introduction

Topological distinction to classify materials has been hugely concerned in the sold state physics communities [130]. Unlike an ordinary insulator regarded as having a trivial topological invariant, there exists an insulating phase having

gapless current-flowing states on the boundary, so called a topological insulator. Recent studies of such topological insulators were initiated by the discovery of quantum spin Hall (QSH) insulators, which are induced by the intrinsic spin-orbit (SO) interactions and exhibits a quantized Hall conductance and gapless edge-localized states. [16, 17, 131]. This novel phase which had been predicted theoretically was generalized in three dimensions [18], and experimental results proved this theoretical results right after [19, 20].

On the other hand, the Hubbard model which considers the on-site Coulomb repulsive interaction between electrons with different spins has also been studied on the honeycomb lattice [21, 22]. This repulsive interaction tends to localize the electrons and yields a Mott gap above some critical value of the interaction strength. In addition to this, it also gives rise for the system to have the antiferromagnetic order with spontaneous symmetry breaking [21]. The local magnetizations of the honeycomb lattice have been shown to display peculiar properties at the open boundary [22]. Recently, it has been also reported that there exists a quantum spin liquid (QSL) phase before the system attains the finite charge gap [23].

Within the interplay of the SO interaction and the Hubbard interaction, many studies are achieved in various methods on the honeycomb lattice. [24–28, 132, 133]. The mean-field study revealed that the phase transition from the QSH insulating phase to an antiferromagnetic Mott insulating (AFMI) phase occurs [24, 132] and even the finite system has been shown to have distinguished phases

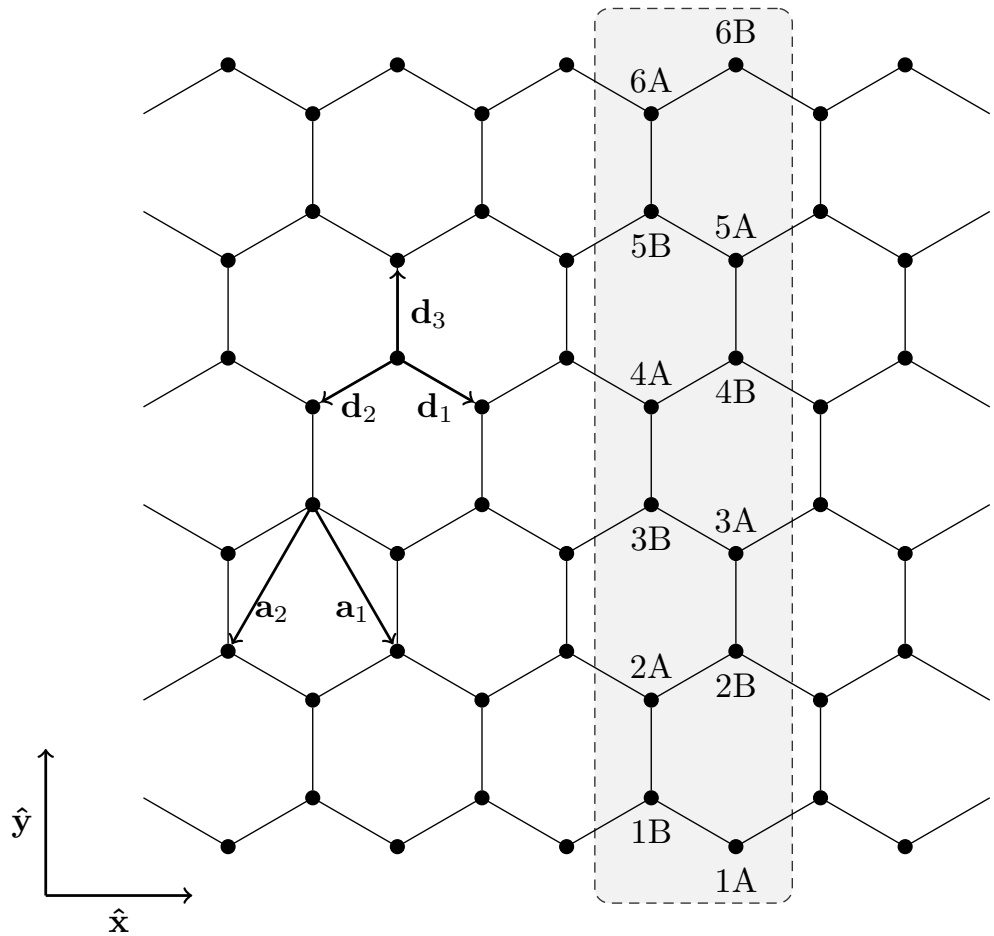

Figure 6.1: Nanoribbon in the 2D honeycomb lattice along the zigzag direction. The unit cell which contains $2L$ atoms is shown by the shaded rectangle where L denotes the number of zigzag lines. The open boundary condition is applied in the vertical axis and the periodic boundary in horizontal axis.

in between [28, 132, 134]. It is also shown in the quantum Monte Carlo (QMC) [25, 27, 133]. and the variational cluster approach (VCA) [26]. that the QSH insulating phase can also exist in the existence of the Hubbard interaction. When

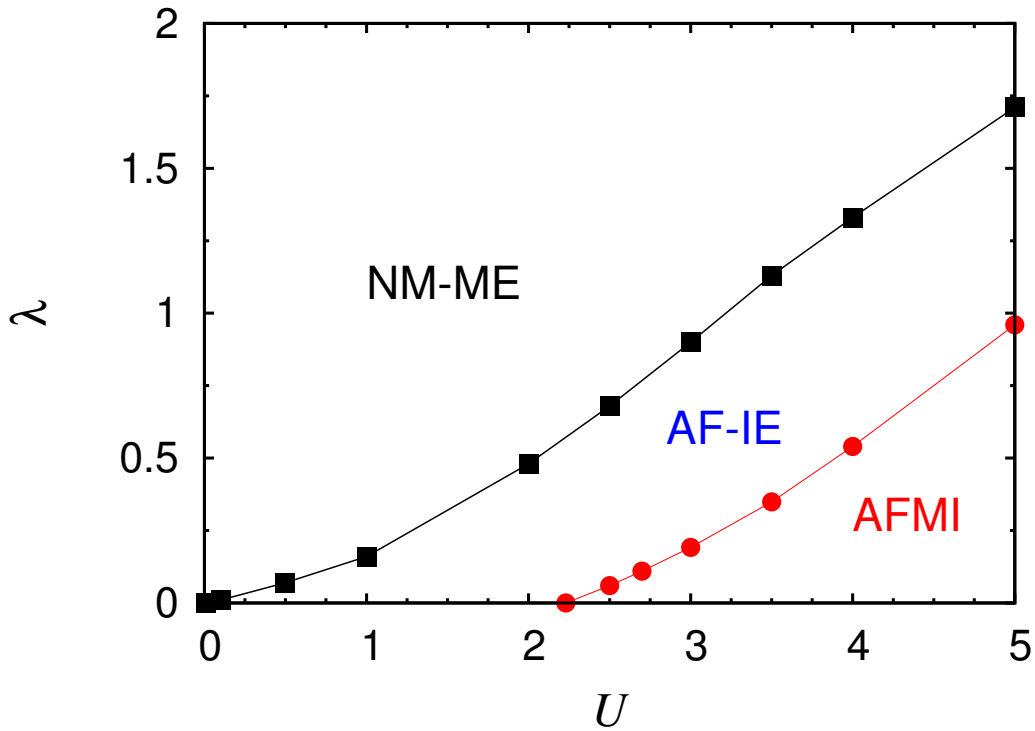

Figure 6.2: Phase diagram of the nanoribbon with $L = 24$ in the Kane-Mele-Hubbard model in the plain spanned by the Hubbard interaction strength U and the spin-orbit coupling strength λ. We use the strengths in a unit of the hopping integral t.

the SO interaction is considered with the correlation effects, the QSL phase can still survive [25, 26, 133], and a finite edge magnetism of a power-law correlation with a paramagnetic bulk state appears [27].

Beyond graphene, recent studies have shown that many materials are described by the 2D honeycomb lattice and that there exists a gap from the SO interaction. We list those materials with their hopping strengths and methods calculating them in Tab. 6.1. They show the materials to be in the QSH phase

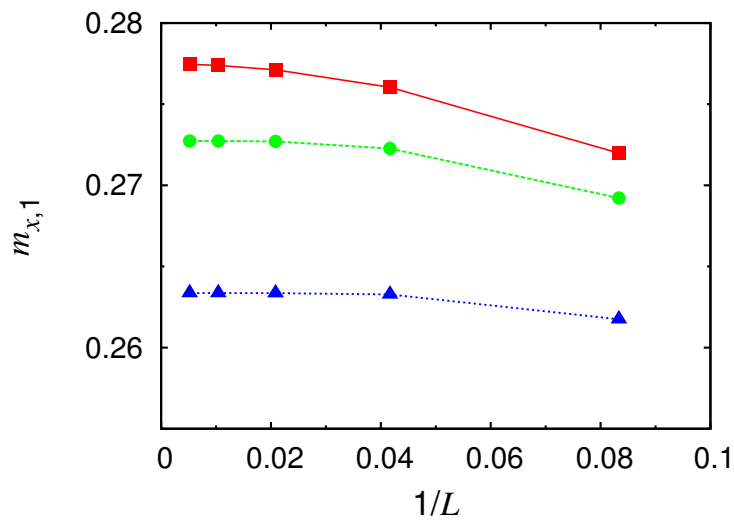

Figure 6.3: Edge magnetization of the nanoribbon ($|\boldsymbol{m}_i = 1|or|\boldsymbol{m}_i = L|$), over $\lambda = 0$ ($\square$), 0.005 ($\circ$), and 0.01 ($\triangle$). The data from $L = 12$ to $L = 192$ are plotted with the inverse of the width and shows that the magnetization remains finite as increasing L.

and their gaps are large enough for applications.

6.2 Model

Our model is described by the Hamiltonian of the KMH model,

$$H = -t \sum_{\langle i,j \rangle \sigma} c^{\dagger}_{i\sigma} c_{j\sigma} + H_{SO} + H_U, \tag{6.1}$$

where

$$H_{SO} = i\lambda \sum_{\langle\langle i,j \rangle\rangle \sigma} \nu_{ij} c^{\dagger}_{i\sigma} \sigma_z c_{j\sigma} \tag{6.2}$$

Table 6.1: Hopping strength and band gap of 2D honeycomb materials from previous studies. The gaps of silicene and germanene are also significantly affected by the Rashba SO interaction while stanene's is negligible. We specify methods of the data: DFT and TB denotes the density functional theory and the tight-binding method, respectively.

Material	t	Gap	Method, etc.
Graphene	2.7 eV	$\sim 10^{-3}$ meV	TB [135], DFT [136]
Silicene	1.5 eV	7.9 meV	TB [137]
		1.55 meV	DFT [138]
Germanene	1.4 eV	93 meV	TB [137]
		23.9meV	DFT [138]
Stanene	1.3 eV	129 meV	TB [137]
		73.5 meV	DFT [138]
		∼100 meV	DFT [139]
		∼300 meV	DFT [139]; fluorinated (*i.e.* SnF)

and

$$H_U = U \sum_i n_{i\uparrow} n_{i\downarrow} \ . \tag{6.3}$$

Here $c^\dagger_{i\sigma}(c_{i\sigma})$ is an electron creation (annihilation) operator of spin σ at site i, $n_{i\sigma} \equiv c^\dagger_{i\sigma} c_{i\sigma}$, $\langle i, j\rangle$ denotes nearest-neighbor (NN) pair, $\langle\langle i, j\rangle\rangle$ denotes next-nearest-neighbor (NNN) pair, σ_z is the Pauli matrix, and $\nu_{ij} = (\mathbf{d}_i \cdot \mathbf{d}_j)/|\mathbf{d}_i \times \mathbf{d}_j|$ in which $\mathbf{d}_i$ is the lattice vector between the NN pair. The parameters t, λ, and U represent the hopping parameter, the SO coupling strength, and the on-site Coulomb repulsion strength, respectively. We use t as a unit of energy in this

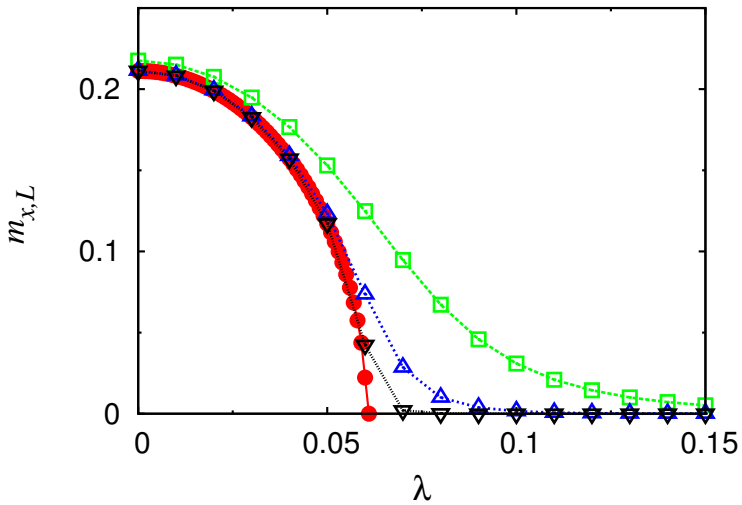

Figure 6.4: (Color online). Magnetization at the center ($i = L$) of the nanoribbon, with L=12 (□), 24 (△), and 48 (▽) as a function of λ for $U = 2.5$. We also plot the bulk magnetization from infinite lattice system with solid circles for comparison.

paper and consider the half-filling system at zero temperature. In our model we assume the 2D honeycomb lattice with a periodic boundary along x-axis and a open boundary along y-axis which is shown with the lattice vectors in Fig. 6.1. The unit cell depicted as a shaded box in Fig. 6.1 consists of $2L$ atoms and L zigzag chains. The length of the nanoribbon along the direction of the periodic boundary makes no difference in our method. so we consider the nanoribbon only with an unit length in this dissertation.

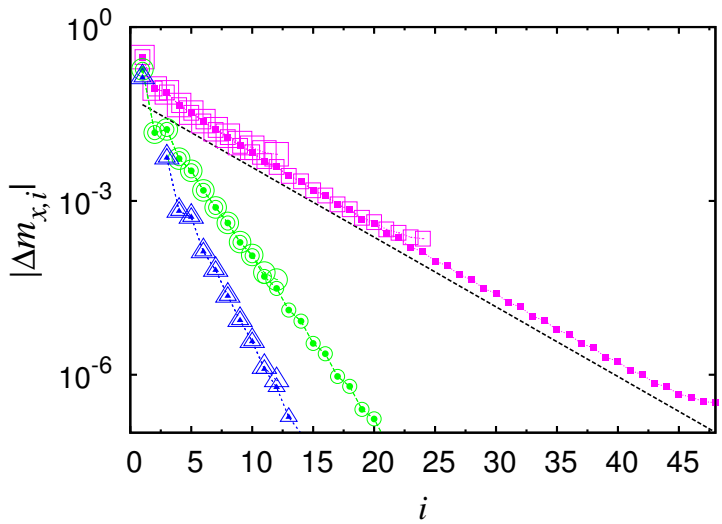

Figure 6.5: Absolute value of the enhanced magnetization, $|\Delta m_{x,i}|$, from the edge ($i = 1$) to center ($i = L$) with U=2.5 (□), 3 (○), and 3.5 (△) for $\lambda = 0$. By semi-log plotting of $|\Delta m_{x,i}|$, it shows exponential decay above the critical point $U_c \simeq 2.23$, in which some deviations occur around both ends of the data. The data are plotted for L =12, 24, and 48. For clarity, the larger symbol size of the data represents the narrower systems henceforth.

6.3 Results

We calculate the ground state of the Hamiltonian with the Hartree-Fock approximation (Sec. 3.2)

Three distinct phases exist in our result, and a phase diagram with those states is obtained as shown in Fig. 6.2. The resulting phases are nonmagnetic and metallic state (NM-ME), antiferromagnetic and insulating edge state (AF-IE), and the AFMI state. From the limit of very large λ, we have the NM-ME state which is adiabatically connected to the QSH phase. Even if U is finite, the gapless edge state of the Dirac fermions still exists with a wide range of U. The other

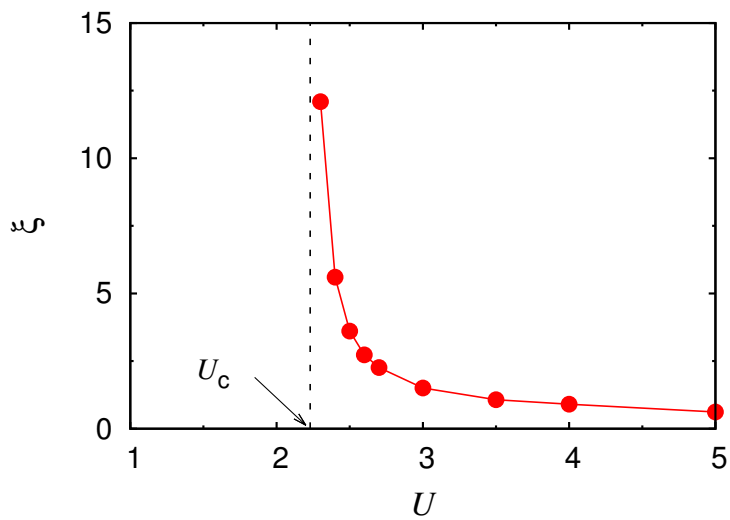

Figure 6.6: Characteristic length ξ of the exponentially decaying magnetization when the system has the bulk magnetization in AFMI for $\lambda = 0$. In the presence of bulk magnetic order, we plot the enhanced magnetization $|\Delta m_{x,i}|$ and fit the data to obtain ξ as U is close to the critical point U_c. We do not fit the data in the region of $U < U_c$ since ξ is divergent and not well-defined.

bands extended to the lattice shows the gap induced by and proportional to λ [16]. Further increasing of U from the NM-ME state turns out that the phase transition to the AF-IE state occurs with a ferrimagnetic structure. The edge-localized band which is gapless and nonmagnetic in the NM-ME state becomes gapped and spin-polarized continuously. The spins in the system have an order along the plane of the lattice and rotate because of the $U(1)$ symmetry as mentioned in the above, which agrees well with the other results [132, 133]. We thus consider only one component of magnetization in the plane, say $m_{i,x}$, without loss of generality. Its magnetizations on the edge site are computed for $U = 1$ as a function of the width L with an increase of λ from zero in Fig. 6.3. We can see that the increase

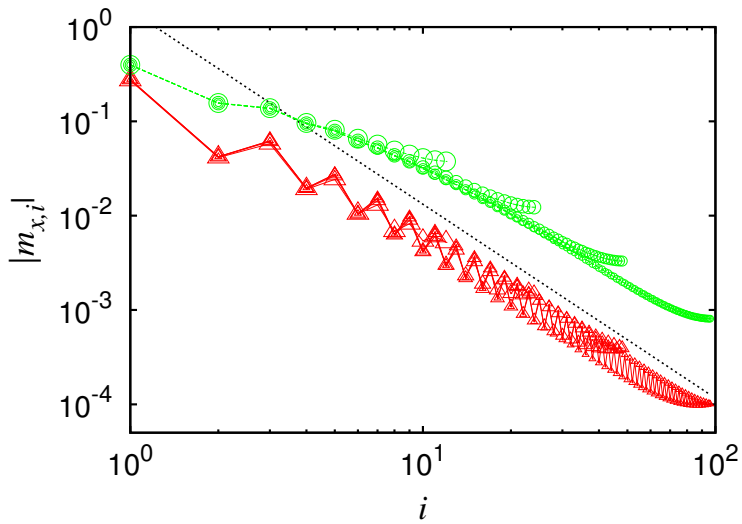

Figure 6.7: Log-log plot of absolute value of the magnetization, $|m_{x,i}|$, with $L = 12$,24 ,48 , and 96 from the edge ($i = 1$) to center ($i = L$). The data of U=1 (△) and 2 (□) for $\lambda = 0$ has the power law in the absence of bulk magnetic order beyond the critical point U_c Some deviations around both ends of the data are also shown as in the exponential decay.

of the SO interaction suppresses slightly the magnetization and that its behavior holds for the large width. Despite of that suppression, the edge magnetizations still saturate to finite values as an increase of L, and are even enhanced for some values of λ. The extrapolation in Fig. 6.3 demonstrates that the edge magnetism is maintained even in the thermodynamic limit.

The existence of the AFMI state represented by the bulk magnetic order and gap is verified in our model. Figure 6.4 shows the convergence of the magnetization of the central site to that of the bulk system. For $\lambda = 0$, the central magnetization of the nanoribbon follows that of the bulk for small width of nanoribbon

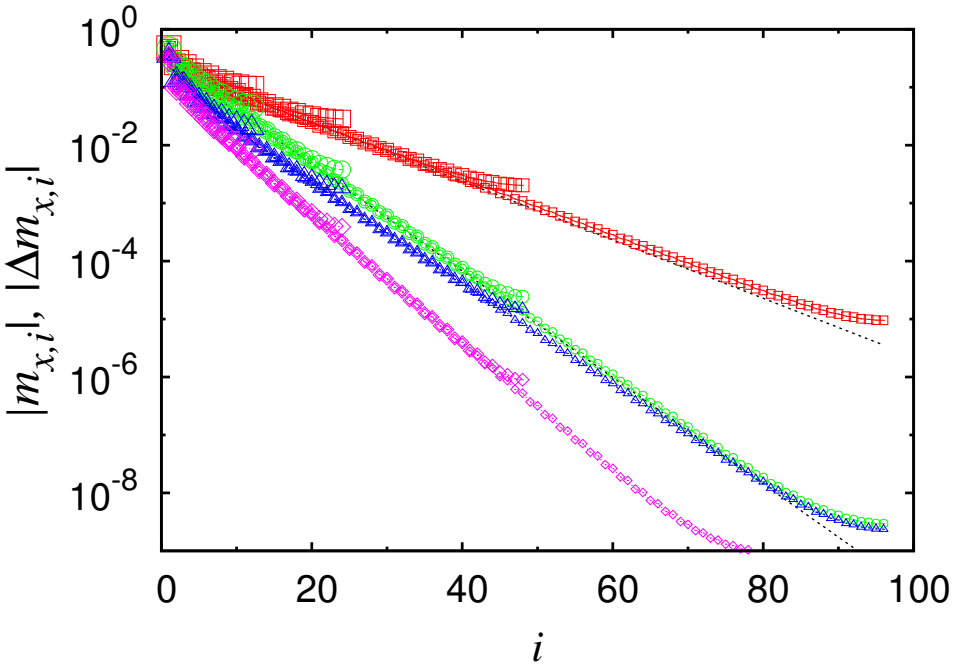

Figure 6.8: Semi-log plot of the magnetizations at finite λ for $U > U_c$. The AFMI phase where the bulk magnetic order exists is still exists for λ =0.02 (diamond) and 0.06 ($\triangle$) smaller than the critical value of λ_c and shows the exponential decay of the enhanced magnetization. As the AF-IE phase with λ =0.07 ($\circ$) and 0.09 ($\square$) above λ_c appears, the exponentially decreasing behavior is also shown.

[22]. It is also shown that the magnetization caused by the Hubbard interaction tends to diminish as λ increases. We can identify the critical point λ_c, where the bulk magnetization vanishes and the continuous phase transition occurs from the AFMI to AF-IE states. The central part of the nanoribbon for sufficiently large width is close to the bulk system very well, while in the region of the AF-IE state there is rather large deviations. These deviations from the bulk diminish at large λ and are also suppressed by the increase of L. Consequently, we show that the

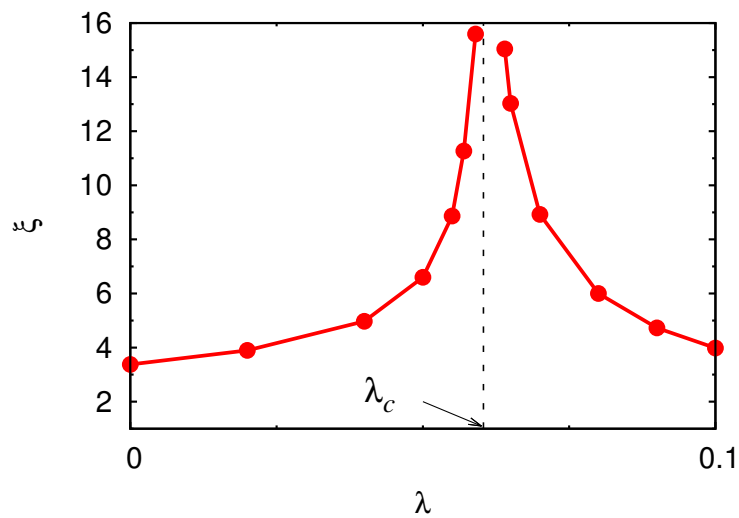

Figure 6.9: Fitting results of characteristic length ξ for finite λ. With an increase of λ, the bulk magnetization of the system becomes suppressed and zero at λ_c, above which the system goes to the AF-IE state. It is shown that ξ increases rapidly around the transition point.

large width nanoribbon can be treated as the infinite lattice system.

In order to examine how the magnetic edge state is connected to the bulk magnetization, we compute the decay of the local magnetization across the nanoribbon of the ferrimagnetic structure for the AF-IE and AFMI state. In the AFMI state where the bulk magnetization exists, we consider the enhanced magnetization, $\Delta m_i \equiv m_i - m_{\text{bulk}}$. The monotonically decreasing of $\Delta m_{x,i}$, from the edge ($i = 1$) toward the center ($i = L$) for $\lambda = 0$ with various widths is shown in Fig. 6.5. It turns out to be an exponential decay, which is expressed by $\Delta m_i \sim e^{-r_i/\xi}$. The enhanced magnetization decreases with an increase of U while the bulk magnetization becomes larger. Some apparent deviations from the exponential decay are due to finite-size effects in the nanoribbon geometry.

Table 6.2: Exponents of the power-law decay, η, by fitting the plot of $\{m_{x,i}\}$ with $r_i^{-\eta}$ for $U < U_c$ in the region of $\lambda = 0$.

U	1	1.5	2
η	2.008(2)	2.072(1)	2.067(1)

One of the deviations occurs around the edge site of which the magnetization is larger than that of the other sites. Another type of deviations is observed around the center where the decay of magnetization is rather suppressed. Both regions of the deviations become wider as the system is near the critical point U_c for a given width. We also find that the characteristic length ξ of the exponential decay decreases as U increases, which means less correlation between the edge and the center of nanoribbon. The best fit of ξ is estimated as function of U in Fig. 6.6. It is indicated that ξ grows very rapidly as U approaches U_c from above. The divergence of the characteristic length is expected to be related to a critical behavior around U_c in the bulk phase transition. In the region of $U < U_c$ with $\lambda = 0$, it is shown that ξ is not well-defined. We plot the magnetization for this region in logarithmic scales which is shown in Fig. 6.7. The profile exhibits a power-law decay, $m_i \sim r_i^{-\eta}$ instead of the exponential decay. This decay to the bulk occurs very slower than the exponential decay, and the bulk magnetization, however, is still expected to be completely zero in the thermodynamic limit. We fit the data up to $L = 384$ and obtain the exponent of the power-law decay, η, as shown in Tab. 6.2.

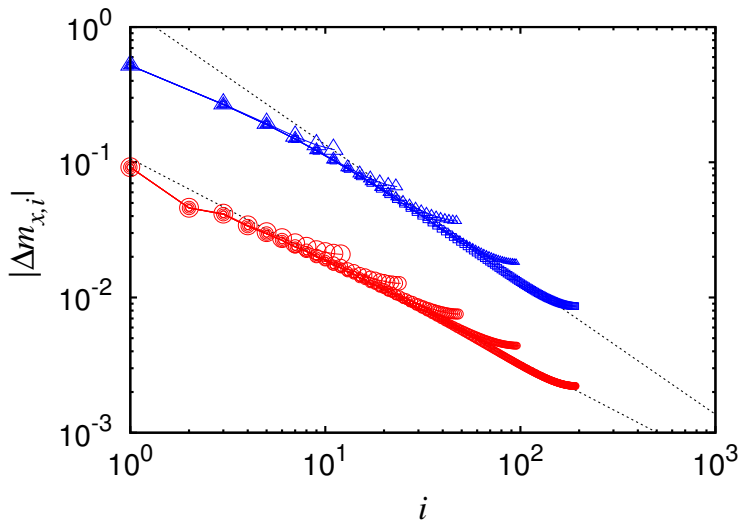

Figure 6.10: Absolute values of the magnetizations $|\Delta m_{x,i}|$ for fixed values of U =2.3 ($\triangle$) and 3 ($\circ$) with finite λs which are very close to each critical point $\lambda_c(U)$. The data are plotted on a log-log scale, giving the power law decay much slower than the exponential decay. On the boundary its critical exponent η depends on λ, and the large deviations occurs around the edge and the center. The data for $U = 2.3$ are shifted by the amount of -0.2 in the log scale.

The best fit gives the exponent η is very close to 2 and independent of U for $U < U_c$.

If we consider finite λ for $U < U_c$, the system lies in the AF-IE state. The introduction of the SO interaction not only suppresses the magnetic order, particularly around the center, also transforms the power-law decay into the exponential decay in which the central magnetization at a large-width nanoribbon has less correlation with the edge magnetizations. Above the critical point U_c the system lying in the AFMI state with $\lambda = 0$ has a phase transition into the AF-IE state at a critical point λ_c with an increase of λ as shown in Fig. 6.4. The response of $m_{x,i}$ to the increase of λ is found to be different from that for fixed values of

Table 6.3: Best fitting values of the exponent of the power-law decay, η, at $\lambda = \lambda_c$ for the fixed values $U > U_c$.

U	2.3	3
λ_c	0.014755	0.1924456
η	0.804(2)	0.953(4)

$U < U_c$. Although λ diminishes the bulk magnetization in the AFMI state, the decay of $\Delta m_{x,i}$ becomes slower for large λ as shown in Fig. 6.8. We can see that the exponential decay in the AFMI state still remains for all finite λ. Above the critical point λ_c, the system obtains the AF-IE state of which the magnetization follows the exponential decay.

In order to understand further the decaying behavior around the transition point, we fit the exponential decay to obtain ξ and plot it as a function of λ in Fig. 6.9 It is shown that ξ diverges in the critical point λ_c as similar to that of the region of $\lambda = 0$. This behavior of ξ ascertains that with the magnetic ordering the phase transition occurs in the nanoribbon system. In this critical point λ_c where ξ is not well-defined, we plot the magnetization in the log-log scale as shown in Fig. 6.10. It gives the power-law decay, however, with the different exponent from what we have in the region of $\lambda = 0$. In addition, the power-law exponent η computed by fitting the data depends on the value of U in this phase boundary as shown in Tab. 6.3. The slopes representing the value of η are quite different for U.

6.4 Summary

We have investigated the collective magnetic properties of the half-filled Kane-Mele-Hubbard model with nanoribbon geometry. By means of the Hartree-Fock approximation we have analyzed the ground state and shown that the magnetic order on the edge persists in the thermodynamic limit. This edge magnetization can survive in the absence of magnetic order in the bulk between the TBI and the AFI. The characteristic length of the magnetization signifies the phase transition between the TBI and the AFI. It has been found to be enhanced as we approach the phase boundary and become divergent at the phase transition point or the (semi-)metallic phase.

Bibliography

[1] *The Many-Body Problem An Encyclopedia of Exactly Solved Models in One Dimension*, edited by D. C. Mattis, (World Scientific, Singapore, 1993).

[2] *Quantum Magnetism*, edited by U. Schollwöck, J. Richter, D. J. J. Farnell, and R. F. Bishop, (Springer-Verlag, Berlin, 2004).

[3] *Frustrated Spin Systems*, 2nd ed., edited by H. T. Diep, (World Scientific, Singapore, 2013).

[4] F. D. M. Haldane, Phys. Rev. Lett. **50**, 1153 (1983).

[5] F. D. M. Haldane, Phys. Lett. A **93**, 464 (1983).

[6] I. Affleck, T. Kennedy, E. H. Lieb, and H. Tasaki, Phys. Rev. Lett. **59**, 799 (1987).

[7] I. Affleck, T. Kennedy, E. H. Lieb, and H. Tasaki, Commun. Math. Phys. **115**, 477 (1988).

[8] I. Affleck, J. Phys. Condens. Matter **1**, 3047 (1989).

[9] S. R. White, Phys. Rev. Lett. **69**, 2863 (1992).

[10] S. R. White, Phys. Rev. B **48**, 10345 (1993).

[11] M. den Nijs and K. Rommelse, Phys. Rev. B **40**, 4709 (1989).

[12] S. M. Girvin and D. P. Arovas, Phys. Scr. **T27**, 156 (1989).

[13] T. Kennedy and H. Tasaki, Phys. Rev. B **45**, 304 (1992).

[14] F. D. M. Haldane, Phys. Rev. Lett. **61**, 2015 (1988).

[15] S. Murakami, N. Nagaosa, and S.-C. Zhang, Phys. Rev. Lett. **93**, 156804 (2004).

[16] C. L. Kane and E. J. Mele, Phys. Rev. Lett. **95**, 146802 (2005).

[17] C. L. Kane and E. J. Mele, Phys. Rev. Lett. **95**, 226801 (2005).

[18] L. Fu, C. L. Kane, and E. J. Mele, Phys. Rev. Lett. **98**, 106803 (2007).

[19] M. König, S. Wiedmann, C. Brüne, A. Roth, and H. Buhmann, Science **318**, 766 (2007).

[20] D. Hsieh, D. Qian, L. Wray, Y. Xia, Y. S. Hor, R. J. Cava, and M. Z. Hasan, Nature **452**, 970 (2008).

[21] S. Sorella and E. Tosatti, Europhys. Lett. **19**, 699 (1992).

[22] M. Fujita, K. Wakabayashi, K. Nakada, and K. Kusakabe, J. Phys. Soc. Jpn. **65**, 1920 (1996).

[23] Z. Y. Meng, T. C. Lang, S. Wessel, F. F. Assaad, and A. Muramatsu, Nature **464**, 847 (2010).

[24] S. Rachel and K. Le Hur, Phys. Rev. B **82**, 075106 (2010).

[25] M. Hohenadler, T. C. Lang, and F. F. Assaad, Phys. Rev. Lett. **106**, 100403 (2011).

[26] S.-L. Yu, X. C. Xie, and J.-X. Li, Phys. Rev. Lett. **107**, 10401 (2011).

[27] D. Zheng, G.-M. Zhang, and C. Wu, Phys. Rev. B **84**, 205121 (2011).

[28] D. Soriano and J. Fernández-Rossier, Phys. Rev. B **82**, 161302 (2010).

[29] W. Heisenberg, Zeitschrift für Phys. **49**, 619 (1928).

[30] T. Kennedy, J. Phys. Condens. Matter **2**, 5737 (1990).

[31] U. Schollwöck, Ann. of Phys. **326**, 96 (2011).

[32] I. Affleck, Nucl. Phys. B **265**, 409 (1986).

[33] I. Affleck and F. D. M. Haldane, Phys. Rev. B **36**, 5291 (1987).

[34] J. Oitmaa, J. B. Parkinson, and J. C. Bonner, J. Phys. C **19**, L595 (1986).

[35] J. Sólyom, Phys. Rev. B **36**, 8642 (1987).

[36] R. R. P. Singh and M. P. Gelfand, Phys. Rev. Lett. **61**, 2133 (1988).

[37] K. Chang, I. Affleck, G. W. Hayden, and Z. G. Soos, J. Phys. Condens. Matter **1**, 153 (1989).

[38] M. P. Nightingale and H. W. J. Blöte, Phys. Rev. B **33**, 659 (1986).

[39] J. B. Parkinson and J. C. Bonner, Phys. Rev. B **32**, 4703 (1985).

[40] S. R. White and D. A. Huse, Phys. Rev. B **48**, 3844 (1993).

[41] R. Botet and R. Jullien, Phys. Rev. B **27**, 613 (1983).

[42] M. Kolb, R. Botet, and R. Jullien, J. Phys. A. Math. Gen. **16**, L673 (1983).

[43] R. Botet, R. Jullien, and M. Kolb, Phys. Rev. B **28**, 3914 (1983).

[44] J. C. Bonner and G. Müller, Phys. Rev. B **29**, 5216 (1984).

[45] U. Glaus and T. Schneider, Phys. Rev. B **30**, 215 (1984).

[46] H. J. Schulz and T. Ziman, Phys. Rev. B **33**, 6545 (1986).

[47] J. B. Parkinson, J. C. Bonner, G. Müller, M. P. Nightingale, and H. W. J. Blöte, J. Appl. Phys. **57**, 3319 (1985).

[48] A. Moreo, Phys. Rev. B **35**, 8562 (1987).

[49] M. Takahashi, Phys. Rev. Lett. **62**, 2313 (1989).

[50] S. Liang, Phys. Rev. Lett. **64**, 1597 (1990).

[51] S. Takada and K. Kubo, J. Phys. Soc. Jpn. **60**, 4026 (1991).

[52] F. Verstraete, V. Murg, and J. Cirac, Adv. Phys. **57**, 143 (2008), 0907.2796 .

[53] R. Orús, Ann. Phys. **349**, 117 (2014).

[54] U. Schollwöck, T. Jolicœur, and T. Garel, Phys. Rev. B **53**, 3304 (1996).

[55] S. R. White and I. Affleck, Phys. Rev. B **54**, 9862 (1996).

[56] G. H. Wannier, Phys. Rev. **79**, 357 (1950).

[57] J. V. Toulouse and G, J. Phys. C **10**, L537 (1977).

[58] J. Villain, J. Phys. C **10**, 1717 (1977).

[59] *Magnetism in condensed matter*, edited by S. Blundell, (Oxford University Press, New York, 2001).

[60] A. K. Kolezhuk and U. Schollwöck, Phys. Rev. B **65**, 100401 (2002).

[61] A. Kolezhuk, R. Roth, and U. Schollwöck, Phys. Rev. Lett. **77**, 5142 (1996).

[62] A. Kolezhuk, R. Roth, and U. Schollwöck, Phys. Rev. B **55**, 8928 (1997).

[63] W. Lenz, Z. Physik **21**, 613 (1920).

[64] E. Ising, Z. Physik **31**, 253 (1925).

[65] E. Lieb, T. Schultz, and D. Mattis, Ann. Phys. **16**, 407 (1961).

[66] T. Sakai and M. Takahashi, J. Phys. Soc. Jpn. **59**, 2688 (1990).

[67] K. Kubo, Phys. Rev. B **46**, 866 (1992).

[68] Y. H. Su, S. Y. Cho, B. Li, H.-L. Wang, and H.-Q. Zhou, J. Phys. Soc. Jpn. **81**, 74003 (2012).

[69] K. Nomura, Phys. Rev. B **40**, 9142 (1989).

[70] G. Gómez-Santos, Phys. Rev. Lett. **63**, 790 (1989).

[71] W. Chen, K. Hida, and B. Sanctuary, Phys. Rev. B **67**, 104401 (2003).

[72] *Leture notes on electron correlation and magnetism*, edited by P. Fazekas, (World Scientific, Singapore, 1999).

[73] T. Sakai and M. Takahashi, Phys. Rev. B **42**, 4537 (1990).

[74] Y. Hatsugai and M. Kohmoto, Phys. Rev. B **44**, 11789 (1991).

[75] S. Ejima and H. Fehske, Phys. Rev. B **91**, 45121 (2015).

[76] P. Calabrese and J. Cardy, J. Stat. Mech.: Theory Exp. , P06002 (2004).

[77] T. Hikihara, J. Phys. Soc. Jpn. **71**, 319 (2002).

[78] T. Hikihara and M. Kaburagi, J. Phys. Soc. Jpn. **69**, 259 (2000).

[79] M. Kaburagi, H. Kawamura, and T. Hikihara, J. Phys. Soc. Jpn. **68**, 3185 (1999).

[80] A. Meyer, A. Gleizes, J. J. Girerd, M. Verdaguer, and O. Kahn, Inorg. Chem. **21**, 1729 (1982).

[81] J. P. Renard, M. Verdaguer, L. P. Regnault, W. A. C. Erkelens, J. Rossat-Mignod, and W. G. Stirling, Europhys. Lett. **3**, 945 (1987).

[82] J. P. Renard, M. Verdaguer, L. P. Regnault, W. A. C. Erkelens, J. Rossat-Mignod, J. Ribas, W. G. Stirling, and C. Vettier, J. Appl. Phys. **63**, 3538 (1988).

[83] K. Katsumata, H. Hori, T. Takeuchi, M. Date, A. Yamagishi, and J. P. Renard, Phys. Rev. Lett. **63**, 86 (1989).

[84] M. Hagiwara, K. Katsumata, I. Affleck, B. I. Halperin, and J. P. Renard, Phys. Rev. Lett. **65**, 3181 (1990).

[85] S. H. Glarum, S. Geschwind, K. M. Lee, M. L. Kaplan, and J. Michel, Phys. Rev. Lett. **67**, 1614 (1991).

[86] S. Ma, C. Broholm, D. H. Reich, B. J. Sternlieb, and R. W. Erwin, Phys. Rev. Lett. **69**, 3571 (1992).

[87] L. P. Regnault, I. Zaliznyak, J. P. Renard, and C. Vettier, Phys. Rev. B **50**, 9174 (1994).

[88] I. A. Zaliznyak, D. C. Dender, C. Broholm, and D. H. Reich, Phys. Rev. B **57**, 5200 (1998).

[89] W. J. L. Buyers, R. M. Morra, R. L. Armstrong, M. J. Hogan, P. Gerlach, and K. Hirakawa, Phys. Rev. Lett. **56**, 371 (1986).

[90] I. A. Zaliznyak, L.-P. Regnault, and D. Petitgrand, Phys. Rev. B **50**, 15824 (1994).

[91] M. Kenzelmann, R. A. Cowley, W. J. L. Buyers, and D. F. McMorrow, Phys. Rev. B **63**, 134417 (2001).

[92] M. Kenzelmann, R. A. Cowley, W. J. L. Buyers, Z. Tun, R. Coldea, and M. Enderle, Phys. Rev. B **66**, 24407 (2002).

[93] T. Masuda, T. Sakaguchi, and K. Uchinokura, J. Phys. Soc. Jpn. **71**, 2637 (2002).

[94] A. P. Ramirez, S. W. Cheong, and M. L. Kaplan, Phys. Rev. Lett. **72**, 3108 (1994).

[95] J. Darriet and L. P. Regnault, Solid State Commun. **86**, 409 (1993).

[96] G. Xu, J. F. DiTusa, T. Ito, K. Oka, H. Takagi, C. Broholm, and G. Aeppli, Phys. Rev. B **54**, R6827 (1996).

[97] F. Tedoldi, R. Santachiara, and M. Horvatić, Phys. Rev. Lett. **83**, 412 (1999).

[98] M. Kenzelmann, G. Xu, I. A. Zaliznyak, C. Broholm, J. F. DiTusa, G. Aeppli, T. Ito, K. Oka, and H. Takagi, Phys. Rev. Lett. **90**, 087202 (2003).

[99] Y. Uchiyama, Y. Sasago, I. Tsukada, K. Uchinokura, A. Zheludev, T. Hayashi, N. Miura, and P. Böni, Phys. Rev. Lett. **83**, 632 (1999).

[100] A. Zheludev, T. Masuda, I. Tsukada, Y. Uchiyama, K. Uchinokura, P. Böni, and S.-H. Lee, Phys. Rev. B **62**, 8921 (2000).

[101] A. Lappas, V. Alexandrakis, J. Giapintzakis, V. Pomjakushin, K. Prassides, and A. Schenck, Phys. Rev. B **66**, 14428 (2002).

[102] B. Pahari, K. Ghoshray, R. Sarkar, B. Bandyopadhyay, and A. Ghoshray, Phys. Rev. B **73**, 12407 (2006).

[103] Z. He and Y. Ueda, J. Phys. Soc. Jpn. **77**, 13703 (2008).

[104] A. K. Bera, B. Lake, A. T. M. N. Islam, B. Klemke, E. Faulhaber, and J. M. Law, Phys. Rev. B **87**, 224423 (2013).

[105] C. P. Landee, K. A. Reza, M. R. Bond, and R. D. Willett, Phys. Rev. B **56**, 147 (1997).

[106] H. A. Katori, Y. Ajiro, T. Asano, and T. Goto, J. Phys. Soc. Jpn. **64**, 3038 (1995).

[107] B. Pahari, K. Ghoshray, A. Ghoshray, T. Samanta, and I. Das, Physica B Amsterdam **395**, 138 (2007).

[108] *Density-Matrix Renormalization : A New Numerical Method in Physics*, edited by I. Peschel, X. Wang, M. Kaulke, and K. Hallberg, (Springer-Verlag, Berlin, 1999).

[109] U. Schollwöck, Rev. Mod. Phys. **77**, 259 (2005).

[110] *Computational Many-Particle Physics*, 1st ed., edited by H. Fehske, R. Schneider, and A. Weiße, (Springer, Hidelberg, 2008).

[111] *Strongly Correlated Systems*, edited by A. Avella and F. Mancini, (Springer, Hidelberg, 2013).

[112] C. Lanczos, J. Res. Bur. Stand. **45**, 255 (1950).

[113] Q. Shao-Jin and L. Ji-Zhong, Commun. Theor. Phys. **36**, 635 (2001).

[114] *OpenMP Parallel Programming*, edited by Y. H. Jeong, (Purple, 2014).

[115] S. R. White, Phys. Rev. Lett. **77**, 3633 (1996).

[116] U. Schollwöck, Phys. Rev. B **58**, 8194 (1998).

[117] T. Hamada, J.-i. Kane, S.-i. Nakagawa, and Y. Natsume, J. Phys. Soc. Jpn. **57**, 1891 (1988).

[118] M. Härtel, J. Richter, D. Ihle, and S.-L. Drechsler, Phys. Rev. B **78**, 174412 (2008).

[119] J. Sudan, A. Lüscher, and A. M. Läuchli, Phys. Rev. B **80**, 140402 (2009).

[120] J. Sirker, Phys. Rev. B **81**, 014419 (2010).

[121] J. Sirker, V. Y. Krivnov, D. V. Dmitriev, A. Herzog, O. Janson, S. Nishimoto, S.-L. Drechsler, and J. Richter, Phys. Rev. B **84**, 144403 (2011).

[122] H. P. Bader and R. Schilling, Phys. Rev. B **19**, 3556 (1979).

[123] S. Furukawa, M. Sato, S. Onoda, and A. Furusaki, Phys. Rev. B **86**, 094417 (2012).

[124] S. Furukawa, M. Sato, and S. Onoda, Phys. Rev. Lett. **105**, 257205 (2010).

[125] L. Balents and O. A. Starykh, Phys. Rev. Lett. **116**, 177201 (2016).

[126] T. Hikihara, M. Kaburagi, and H. Kawamura, Phys. Rev. B **63**, 174430 (2001).

[127] C. Senko, P. Richerme, J. Smith, A. Lee, I. Cohen, A. Retzker, and C. Monroe, Phys. Rev. X **5**, 021026 (2015).

[128] I. Cohen, P. Richerme, Z.-X. Gong, C. Monroe, and A. Retzker, Phys. Rev. A **92**, 012334 (2015).

[129] J. J. García-Ripoll, M. A. Martin-Delgado, and J. I. Cirac, Phys. Rev. Lett. **93**, 250405 (2004).

[130] M. Hasan and C. Kane, Rev. Mod. Phys. **82**, 3045 (2010).

[131] B. A. Bernevig, T. L. Hughes, and S.-C. Zhang, Science **314**, 1757 (2006).

[132] Y. Yamaji and M. Imada, Phys. Rev. B **83**, 205122 (2011).

[133] M. Hohenadler, Z. Y. Meng, T. C. Lang, S. Wessel, A. Muramatsu, and F. F. Assaad, Phys. Rev. B **85**, 115132 (2012).

[134] D. Gosálbez-Martínez, D. Soriano, J. Palacios, and J. Fernández-Rossier, Solid State Commun. **152**, 1469 (2012).

[135] H. Min, J. E. Hill, N. A. Sinitsyn, B. R. Sahu, L. Kleinman, and A. H. MacDonald, Phys. Rev. B **74**, 165310 (2006).

[136] Y. Yao, F. Ye, X.-L. Qi, S.-C. Zhang, and Z. Fang, Phys. Rev. B **75**, 041401 (2007).

[137] C.-C. Liu, W. Feng, and Y. Yao, Phys. Rev. Lett. **107**, 076802 (2011).

[138] C.-C. Liu, H. Jiang, and Y. Yao, Phys. Rev. B **84**, 195430 (2011).

[139] Y. Xu, B. Yan, H.-J. Zhang, J. Wang, G. Xu, P. Tang, W. Duan, and S.-C. Zhang, Phys. Rev. Lett. **111**, 136804 (2013).

국문 초록

본 학위논문은 낮은 차원계의 스핀과 전자계에서 일어나는, 떠오름 현상, 그 중 스핀 자유도를 통해 나타나는 현상에 대하여 연구하였습니다. 가장 가까운 이웃한 스핀과 강자성 결합과 다음으로 가까운 이웃한 스핀과 반강자성 결합이 동시에 존재함으로써 강자성적 찔찔맴이 있는 스핀-1 사슬에서 바닥 상태와 그 상관함수를 밀도행렬-되맞춤군 방법을 이용하여 분석하였습니다. 이중 할데인 상태는 강자성 결합으로 인해 파동수가 0과 π 사이의 값을 갖는 엇맞는 상관도를 보이며 강자성 상으로 상전이를 합니다. 이러한 짧은 범위 상관도는 연속적으로 전이 지점에서 강자성적 불안정성으로서 나타나게 됩니다. 교환 상호작용 내에 비등방성을 추가적으로 고려하면 새로운 무질서한 상과 손지기 상이 넓은 영역에 나타남을 확인하였습니다. 또한 스핀-1/2과 고전적 스핀 계들의 결과와 비교하고 계에서 나타나는 끈질서에 대해 살펴보았습니다.

케인-멜레-허바드 모형의 띠에서 나타나는 자성에 대해서도 연구하였습니다. 하트리-폭 근사를 이용하여 케인-멜레 모형에서 허바드 상호작용이 주는 영향을 띠 상태의 특성을 살펴 조사하였습니다. 다양한 길이의 나노 끈에서 국소 자기화량을 계산 하였으며, 열역학적 극한에서의 상그림을 얻었습니다. 자기화량 결과는 넓은 범위의 스핀-궤도 결합에서 평면상의 자기 질서가 띠의 존재하는 것을 보였습니다. 자기화량의 특성 길이의 변화는 위상 절연체와 반자

성 절연체간의 상전이와 밀접한 연관을 확인할 수 있었습니다.

주요어: 양자 스핀 사슬, 1차원 계, 할데인 틈, AKLT 상태, 스핀 교환 상호작용, 하이젠베르크 모형, 쩔쩔맴, 비등방성, 밀도행렬-되맞춤군, 케인-멜레-허바드 모형, 벌집 격자, 갈지자형 끈, 스핀-궤도 결합, 허바드 상호작용, 하트리-폭 근사, 띠 상태, 위상적 상태

학번: 2012-30107